7-19-2018

A Quantum Simulation Study of III-V Esaki Diodes and 2D Tunneling Field-Effect Transistors

Patsy Cadareanu
pxc7985@rit.edu

A Quantum Simulation Study of III-V Esaki Diodes and 2D Tunneling Field-Effect Transistors

Patsy Cadareanu

A Quantum Simulation Study of III-V Esaki Diodes and 2D Tunneling Field-Effect Transistors

Patsy Cadareanu

July 19, 2018

A Thesis Submitted
in Partial Fulfillment
of the Requirements for the Degree of
Master of Science
in
Microelectronic Engineering

R·I·T | Kate Gleason
College of ENGINEERING

Department of Electrical and Microelectronic Engineering

A Quantum Simulation Study of III-V Esaki Diodes and 2D Tunneling Field-Effect Transistors

Patsy Cadareanu

Committee Approval:

Dr. Sean L. Rommel *Advisor* Date
Gleason Professor, Electrical and Microelectronic Engineering

---

Dr. James E. Moon Date
Professor, Electrical and Microelectronic Engineering

Dr. Santosh K. Kurinec Date
Professor, Electrical and Microelectronic Engineering

Dr. Robert Pearson Date
Associate Professor, Electrical and Microelectronic Engineering
Program Director, Microelectronic Engineering

Dr. Sohail A. Dianat Date
Department Head of Electrical and Microelectronic Engineering

Acknowledgments

This thesis is the culmination of my 7th and final year at the Rochester Institute of Technology spent in pursuit of my bachelor's and master's degrees in Microelectronic Engineering, none of which would have been possible without the unfaltering support of many. Here's a few of them:

Dr. Sean Rommel, my advisor, introduced me to the idea of 2D semiconductors and, with greater consequence, to the importance of doing research grounded in theoretical knowledge. I am extremely thankful for his guidance and especially his patience.

Dr. Robert Pearson has supported me in the Microelectronic Engineering program since I joined in 2011. Considering how "green"I was when I started out, without his constant pushes I would have never made it through.

Drs. Santosh Kurinec and James Moon are two of my inspirations for pursuing a doctorate. I hope to one day be as passionate for semiconductors as they are.

Udita Kapoor, my partner on this project, is a true joy to work and talk with and you should read her thesis if you're going to go through the trouble of reading this one.

The Materials Design team, specifically Ray Shan and Volker Eyert and Purdue University's Gerhard Klimeck, Yuanchen Chu, and Tillman Kubis provided invaluable assistance with producing and interpreting simulations.

My parents have given me continuous support even in preparing this document (dad walked my dog while I reread incomprehensible papers and mom made my most tedious LaTex tables), and I wouldn't have made it this far without them.

And last but never least, my speed-dial: CLF, MB, KTN, and CJR.

Abstract

Tunnel field-effect transistors (TFETs) have long been considered as a replacement technology for metal-oxide-semiconductor field-effect transistors (MOSFETs) in low-power digital applications due to their low OFF-current (I_{OFF}) and small subthreshold swing (SS). These benefits are somewhat neutralized by the low ON-current (I_{ON}) exhibited by TFETs fabricated with large bandgap (E_g) semiconductors such as silicon. To offset this drawback, different material systems can be used, with material optimization required for the channel material, the gate stack, and their corresponding geometries. This study considers the novel idea of using 2-dimensional (2D) semiconductors for the channel material in TFETs, and the potential effects of such a channel on the physics of the resulting device. After this theoretical discussion of TFETs, the simulation requirements of such a device are introduced as well as the two quantum simulation systems of choice, Vienna Ab initio Simulation Package (VASP 5.4) as offered by Materials Design and NanoHUB's NEMO5. Topics examined with simulation theory in mind include the density functional theorem (DFT) and convergence criteria. Previously fabricated Esaki diodes from Pawlik *et al.* are simulated using NEMO5 and the necessity of bowing application to the tight-binding parameters is shown. Tables clarifying the tight-binding parameters of InGaAs from the NEMO5 *all.mat* file and their associated bowing parameters are included. The simulations performed with the bowing parameters included are shown to match the experimental data almost exactly. Initial VASP 5.4 simulations for GaAs and InAs are shown and the practicality of DFT using the generalized gradient approximation (GGA), HSE06 with GGA, and Hartree-Fock methods is discussed; HSE06 with GGA is shown to produce simulations closest to reality, though there is a significant computation time trade-off. A designed experiment varying the lattice constants of MoS_2 and WTe_2 is performed and included as an example of the simulation system's capabilities. A plot of VASP 5.4 and NEMO5 MoS_2 bandstructure results is also included.

Contents

List of Figures

List of Tables

List of Symbols

Term	Description	Units/Value
C'_D	Depletion region capacitance per unit area	F/cm^2
C'_{ox}	Oxide capacitance per unit area	F/cm^2
$\mathcal{E}$	Electric field	V/cm
E_c	Energy at the conduction band edge	eV
E_F	Fermi level	eV
E_g	Band gap energy	eV
E_v	Energy at the valence band edge	eV
E_x, E_y	Electric field normal and parallel to the gate	V/cm
$\hbar$	Reduced Planck constant	6.582×10^{-16} eV·s
I_D	Drain current	A
J_t	Band to band tunneling current density	A/cm^2
k	Boltzmann's constant	8.617×10^{-5} eV/K
m^*	Carrier effective mass	kg
N_A	Acceptor concentration	cm^{-3}
N_c	Effective density of states in the conduction band	cm^{-3}
n_i	Intrinsic carrier concentration	cm^{-3}
q	Elementary charge	1.602×10^{-19} C
SS	Subthreshold swing	mV/dec
T	Temperature	K
V_{th}	Threshold voltage	V
V_{DS}	Drain–Source voltage	V
V_{eff}	Effective reverse bias voltage	V
V_{FB}	Flatband voltage	V
V_G	Gate voltage	V
ϵ_s	Permittivity of a semiconductor	F/cm
μ_n, μ_p	Mobility of electrons and holes respectively	cm/V·s
Ψ_{sa}	Surface potential	V

Chapter 1

Introduction and Motivations

The intention of research is to further the respective field's knowledge in a specific domain, but as it is easier to continue along the path of previous research than it is to take up something entirely new, sometimes these spheres of expertise become either irrelevant or so specific they lose meaning for anyone in the field. To avoid this, the research proposed in this study is new and unfamiliar at the Rochester Institute of Technology. To advance in a new field requires previous knowledge to build on. This means that while the primary interest of this research is in developing two-dimensional (2D) tunneling field-effect transistors (TFETs) through a quantum simulation study, simpler devices with real data available for comparison such as III-V Esaki diodes previously fabricated and tested by Dr. Sean Rommel's research group in the past must first be simulated. Once these simulations are performed and their results are determined to match reality, 2D TFETs can then be similarly simulated and these simulations can be considered valuable. This way, an understanding of future research is intricately tied to the research of the past.

Academia is a potent breeding ground for ideas to feed industrial progress, especially in the semiconductor industry. As such, looking at the ideas currently being funded by industry giants is one of the best ways to determine where to focus future research and this was done prior to this study. The Center for Low Energy Systems Technology (LEAST) established in 2013 and led by Notre Dame University is

composed of 12 university microelectronics research centers and funded by the Semiconductor Research Corporation (SRC) and the Defense Advanced Research Projects Agency (DARPA). Each of these 12 centers receives approximately $6 million annually for their research. The research of interest at these centers is the development of more energy-efficient integrated circuits with a focus on ultra-low voltage and steep transistors. There is no mention on the LEAST website of III-V material devices, so even though there's an industrial market for III-V' s, there is not a lot of research potential there because funding for such devices has been withdrawn. *From this observed shift in research areas in the industry towards non-III-V and non-CMOS devices, 2D tunnel FETs are considered.*

One of the main problems with transistor scaling and increased chip density is that it leads to increased power density on the chip. This requires that the supply voltage (V_{DD}) be decreased to reduce power consumption which in turn results in an exponential increase in the leakage current. In metal-oxide-semiconductor field-effect transistors (MOSFETs) only the carriers with enough energy to exceed the source-channel potential barrier, and thus enter the channel from the source, will contribute to the ON-current (I_{ON}) of the device. [2] The subthreshold swing (SS) parameter refers to the gate-to-source voltage needed to change the drain current by one order of magnitude [4]. Eq. 1.1 can be used to calculate the ideal SS. [17, 18]

$$SS(T) = \frac{kT}{q} ln(10) \tag{1.1}$$

For the non-ideal SS, there is a dimensionless prefactor n which accounts for non-idealities, so that the equation is:

$$SS(T) = \frac{kTn}{q} ln(10) \tag{1.2}$$

where the non-ideality factor is defined as:

$$n = 1 + \frac{\gamma}{2\sqrt{\Psi_{sa}}} \tag{1.3}$$

Ψ_{sa} refers to the surface potential and γ is the body-effect coefficient.

A small SS value corresponds to a faster switching speed and allows operation at lower supply voltages, and is thus desired [8]. The minimum subthreshold swing (SS_{min}) in a MOSFET is limited to approximately 60 mV/decade at room temperature (300 K) because the carriers follow the Fermi-Dirac (FD) distribution and their energy is bounded by the fixed slope kT where k is the Boltzmann constant and T is the temperature [2].

Tunnel field-effect transistors (TFETs) differ from MOSFETs in that their I_{ON} is facilitated through a process called band-to-band tunneling (BTBT) at the source-channel potential barrier. In BTBT a considerable number of carriers with energy lower than the potential barrier will make it into the channel region because BTBT enables carriers to go through the potential barrier instead of limiting transport into the channel to only those that are energetic enough to get over the barrier. This results in the possibility of lowered SS values in TFETs; demonstrations have been shown with SS_{min} values as low as 21 mV/decade for a vertical III-V silicon (Si) nanowire with bias voltage (V_{DS}) of 0.1 V and 1 V. [2] A derivation of the SS_{min} as shown by Wei *et al.* as relevant for TFETs is provided in this study. Note that because the BTBT probability is often much smaller than 1, I_{ON} for TFETs is usually smaller than for MOSFETs, and special considerations must be taken to change this [8].

Owing to its tunneling-based current generation scheme, the structure of a TFET is different than that of a MOSFET. Fig. 1.1 (a) and (b), taken from Datta *et al.*, show a typical double-gated (DG) n-type TFET structure with asymmetrical

source and drain doping and an intrinsic region. [2] Note that TFET structures do not require two gates, and this device in particular is designed with two gates for increased gate control.

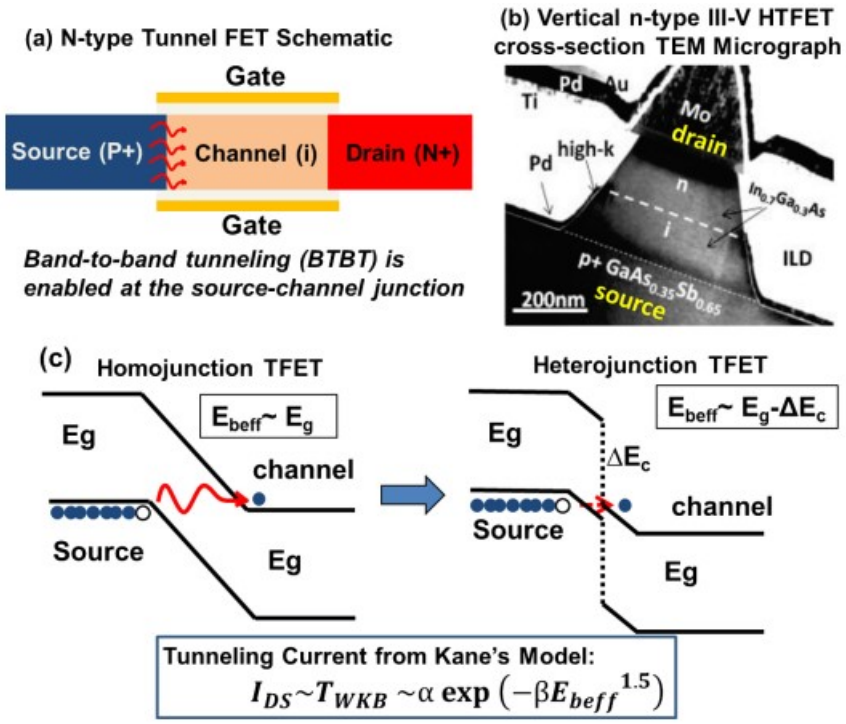

Figure 1.1: (a) The DG n-type TFET structure shown with carriers as arrows. (b) Transmission electron microscopy (TEM) micrograph of a fabricated TFET device. (c) Homojunction vs. heterojunction TFET carrier tunneling.[1][2]

For the transport cases shown in Fig. 1.1(c) to occur, a gate bias (V_G) is applied to either the top or bottom gate of the TFET which will cause the conduction band (E_C) of the intrinsic layer to lower. With enough voltage on the gate the E_C of the intrinsic layer can lower below the valence band (E_V) of the source, thus creating a window for the electrons to go from the source into the intrinsic region and then into the drain. As V_G is decreased, the bands will go back to their regular configurations and the tunneling window will close. Fig. 1.1(c) also shows that heterojunction TFETs can allow for increased I_{ON} when compared to homojunction TFETs by decreasing the

[1]Reprinted from Tunnel FET technology: A reliability perspective, vol. 54, no. 5, S Datta and H Lie and V Narayanan, pages 861-874, Copyright (2014), with permission from Elsevier.

tunnel barrier (E_{beff}) [2].

The operation of TFETs is limited by two parameters: the *SS* and the ON-OFF current ratio, sometimes referred to as the onset strength, both of which will be discussed in detail [8, 9]. Optimal *SS* and onset strength can be achieved through the selection of channel material, TFET gate stack, and the corresponding geometries [7]. The channel material and geometry in particular will be explored in depth.

Interfacial defects can increase *SS* considerably, thus negatively impacting device performance and overcoming the primary benefit of TFET devices. This *SS* degradation can be alleviated through the exploitation of dangling bond-free surfaces provided by two-dimensional (2D) materials. Transition metal dichalcogenides (TMDs) are particularly promising 2D materials due to their tunable bandgap (E_g) size, ability to adjust the Fermi level through doping, and receptivity to layer stacking. [9] The latter of these benefits will be considered.

Though the interest is clearly in fabricating TMD TFET devices, it would be irresponsible to start by jumping headfirst into making such devices due to the prohibitive cost of fabrication and materials. Instead, the research in this study is focused on determining the best quantum simulation packages and obtaining an understanding of how to use these systems most effectively.

First, the necessity of quantum simulations is deliberated. Quantum simulations software packages such as the Vienna Ab initio Simulation package are generally significantly more expensive than their TCAD counterparts. The Rochester Institute of Technology owns a license to the TCAD system Silvaco Athena and Atlas at the time of this research and corresponding publication, so this software package would have been the optimal choice to use. However, it is determined that TCAD simulations are not thorough enough to adequately capture tunneling effects and the negative differential resistance which is the defining characteristic of the Esaki diode and TFET, and this is discussed in detail.

The goal of quantum simulations are $E - k$ plots and $I - V$ characteristics that are similar to real data. Thus, the code must converge onto a single value. Each iteration in a quantum simulation is composed of a guess, followed by a calculation of the error (that is, the difference between two iterations), followed by an iteration corrected using the error, etc., until the error is small enough, as set by the user. At this point convergence is said to occur.

Once the two quantum simulation systems of choice are identified, previous Esaki diode data is simulated in Purdue's NEMO5 package to determine how well the simulations corresponds to reality. The simulation model used originally is the virtual crystal approximation (VCA); this corresponds to the tight-binding parameters used. VCA assumes that the tight-binding parameters will vary linearly with the composition so that the two molecules of interest (in the case of this study, InAs and GaAs) both contribute equally in the final composition, but this is not the case. Instead, a correction factor called a **bowing parameter** must be applied. This bowing parameter is the empirical offset between the two molecules. Bowing parameters as described in Luisier *et al*. are considered [15]. An overview of the NEMO5 tight-binding parameters and what they correspond to in reality is included in this thesis. The Esaki diode simulations are run using the regular VCA model and the model adjusted with the bowing parameters, and comparisons of the results are made. VASP 5.4 and NEMO5 results for MoS_2 bandstructure simulations are plotted together in this thesis, and this is the first step to calculating a set of bowing parameters for this material system.

The density functional theory (DFT) is one solution to solving many-body Schrödinger equations, and this is the fastest VASP 5.4 simulation method to run for bandstructure simulations. A comparison of this and two other available simulation methods (DFT with GGA-PBE, HSE06 with GGA-PBE, and Hartree-Fock) is included in this study. The simulation speed and accuracy are both considered. Lattice constant

variation effects in VASP 5.4 are also considered for both standard III-V and MoS_2 and WTe_2 systems, as this sort of change corresponds to added strain or monolayer directions, such as armchair or zigzag directions.

Chapter 2

Diode and Tunnel FET Theory

2.1 Esaki Diode Introduction

Tunnel diodes were first discovered in 1957 by Leo Esaki when he noticed the distinctive N-shaped transfer characteristic now called negative differential resistance (NDR) that has come to define them. They are also called Esaki diodes for this historical reason. [19, 20]

Tunneling occurs when a particle such as an electron actually penetrates the potential barrier if it is thin enough compared to the electron's Bloch wavelength. Seabaugh and Lake refer to tunneling as a ghostlike passage which is a good way to think of it. [20]

Tunnel diodes in particular are heavily doped on both $p-$ and $n-$sides. They exhibit both normal minority-carrier-based diffusion current and majority-carrier-based tunneling current (the latter for low voltage conditions). Fig. 2.1 from Pawlik's doctoral thesis shows the transfer characteristics and band diagrams for the different types of bias in a typical tunnel diode. [3]

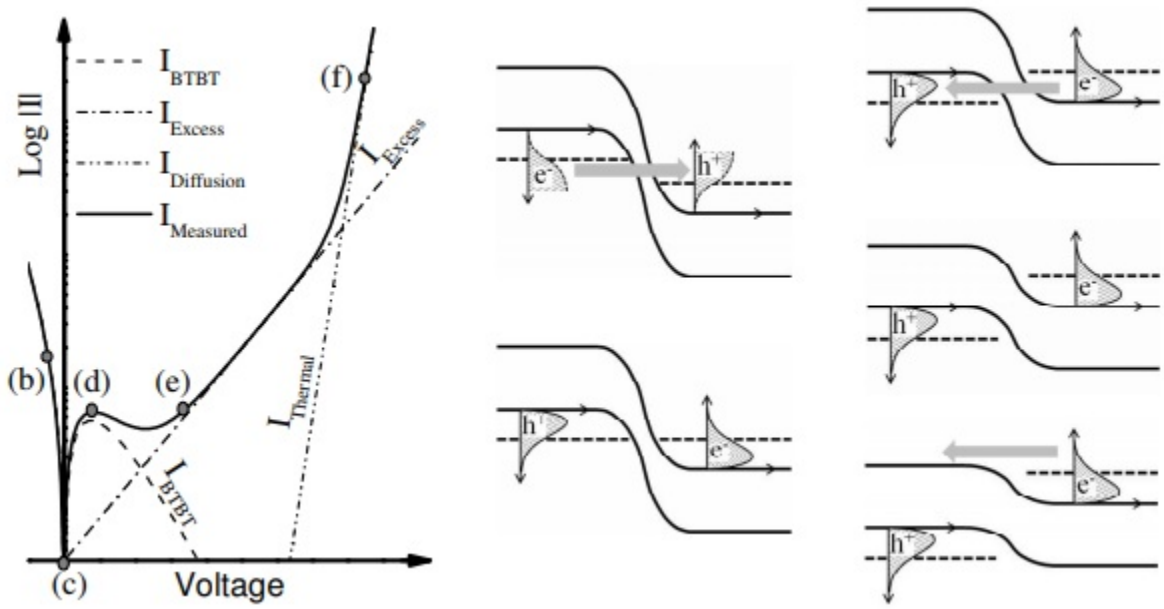

Figure 2.1: (a) I-V characteristic, and schematic band diagram for (b) reverse bias, (c) equilibrium, (d) peak tunneling current, (e) minimum direct tunneling current, and (f) diffusion current for a generic ETD. [3]

2.2 Subthreshold Swing Analysis for TFETs

Wei's group investigated the *SS* of TFETs by deriving a comprehensive analytical model based on electrostatic and material effects. An analysis of their findings is used to provide more understanding of TFET requirements from an operation stand-point. The device and corresponding energy band diagram assumed in their derivation is seen in Fig. 2.2. Relevant parameters in this figure as well as in the derivations to come include: $f_s(E)$, the FD distribution of electrons in the source region; $f_d(E)$, the FD distribution of electrons in the drain region; W_T, the minimum tunnel width; E_{cc}, the minima of the conduction band in the channel region; E_{vs}, the maxima of the valence band in the channel region; E_{vj}, the maxima of the valence band at the source-to-channel junction; E_g, the band gap; E_{fs}, the source Fermi level; E_{fd}, the drain Fermi level; and ΔE, the allowed tunnel window contributing to tunneling transport. [4]

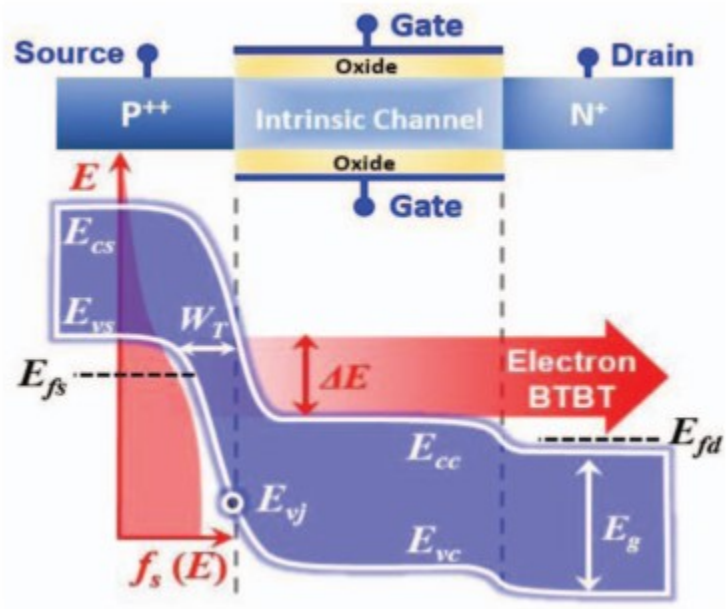

Figure 2.2: (Top) The structure of a DG n-TFET device. (b) The band diagram of this device.[1] [4]

The source-to-channel tunneling current (I_{ds}) Wei *et al.* employed is derived from making assumptions based on this device with respect to Eq. 2.1, the current for one conduction mode in TFETs within the Landauer's formalism. [4]

$$I_{ds} = \frac{2q}{h} \int_{E_{cc}}^{E_{vs}} T(E)[f_s(E) - f_d(E)]dE \tag{2.1}$$

where q is the electron charge, h is Planck's constant, $T(E)$ is the BTBT probability, and $f_{s/d}(E)$ is the source-to-drain FD distribution. These assumptions include: (1) the BTBT probability remains constant across the relevant tunnel window, which is valid for a small (within a few kT) tunnel window, and (2) the FD distribution of electrons in the drain region is small enough to ignore when compared to the FD distribution of electrons in the source region, and (3) the Fermi function integral is

[1] Reprinted from (C. Wei, D. Sarkar, Y. Khatami, K. Jiahao, and K. Banerjee, Subthresholdswing physics of tunnel field-effect transistors, AIP Advances, vol. 4, no. 6, June 2014) with the permission of AIP Publishing.

collected into a term $F_{Integral}$. The simplified tunneling current equation is then:

$$I_{ds} = \frac{2q}{h} T(\Delta E) F_{Integral} \tag{2.2}$$

where

$$F_{Integral} = kT \ln \frac{1 + \exp\left(\frac{E_{fs} - E_{vs} + \Delta E}{kT}\right)}{1 + \exp\left(\frac{E_{fs} - E_{vs}}{kT}\right)}. \tag{2.3}$$

The BTBT probability is found by solving the 2D Poisson equation for channel potential. This is done by simplifying the Poisson equation into a 1D form through a parabolic approximation, then using an analytic model cited by Zhang *et al.* that defines the electrostatic potential profile around the tunnel junction in double-gated (DG) TFETs. This is used to find the valence band maxima at the source-to-channel junction, E_{vj}:

$$E_{vj} = \sqrt{(E_{vs} - E_{fs} + \delta E)^2 + \gamma^2 + 2\gamma(\Delta E_{sc} + E_{vs} - E_{fs})} - (\Delta E_{sc} + E_{vs} - E_{fs} + \gamma) \tag{2.4}$$

where

$$\Delta E_{sc} = E_g + \delta E + \Delta E \tag{2.5}$$

$$\delta E = (E_{cc} - E_{vs})\Big|_{V_{gs}=0} \tag{2.6}$$

$$\gamma = \frac{q^2 N_{A,eff} \lambda^2}{\epsilon_{ch}} \tag{2.7}$$

$$N_{A,eff} = N_A - \frac{\epsilon_{ox}(\Delta E_{sc} + E_{vs} - E_{fs})}{\pi q^2 T_{ox} T_{ch}} \tag{2.8}$$

$$\lambda = \sqrt{\frac{\epsilon_{ch} T_{ox} T_{ch}}{2\epsilon_{ox}}} \tag{2.9}$$

where N_A is the source doping, ϵ_{ox} is the permittivity of the gate dielectric material, T_{ch} is the corresponding thickness of the gate dielectric material, ϵ_{ch} is the permittivity of the channel material, and T_{ch} is the corresponding thickness of the channel

material.

Using Eqs. (2.4 - 2.9), the minimum tunnel width is defined as follows:

$$W_T = L_1 + L_2 - \lambda cosh^{-1}(\frac{\Delta E + \delta E - E_{fs} + E_{v,WT}}{E_{vs} - E_{fs} + \delta E}) - \sqrt{\frac{2\epsilon_{ch}(E_{vs} - E_{v,WT} - E_g)}{q^2 N_{A,eff}}} \tag{2.10}$$

where L_1 and L_2 are the depletion widths:

$$L_1 = \sqrt{\frac{2\epsilon_{ch}(E_{vs} - E_{vj})}{q^2 N_{A,eff}}} \tag{2.11}$$

$$L_2 = \lambda cosh^{-1}(\frac{\Delta E_{sc} + E_{vs} - E_{fs} - (E_{vs} - E_{vj})}{E_{vs} - E_{fs} + \delta E}) \tag{2.12}$$

and

$$E_{v,WT} = \sqrt{(E_{vs} - E_{fs} + \delta E)^2 + \gamma^2 + 2\gamma(\Delta E + \delta E + E_{vs} - E_{fs})} - (\Delta E + \delta E + E_{vs} - E_{fs} + \gamma) \tag{2.13}$$

Finally, the BTBT probability is found using the Wentzel-Kramers-Brillouin (WKB) approximation and the two-band dispersion relation as established by Kane in his famous 1961 paper. [21, 4]

$$T(\Delta E) = \exp(\frac{-\pi\sqrt{2m_T}E_g^{3/2}}{4q(\frac{h}{2\pi})\bar{F}}) \tag{2.14}$$

where m_T is the tunnel effective mass, and the junction electric field is given by $\bar{F} = \frac{E_g}{W_T}$. As will be noted later in this thesis, full band structure consists of many bands. In certain circumstances, Kane's 2-band model is adequate. Also, Kane assumes a parabolic dispersion which is not always correct.

Equations (2.2 and 2.14) can be combined to define an equation for SS, which in turn can be broken down into its contributions from the tunneling probability, SS_T,

and from the FD distribution, SS_{FD}:

$$SS = (\frac{dlog_{10}(I_{ds})}{d(\Delta E/q)})^{-1} = \frac{SS_T SS_{FD}}{SS_T + SS_{FD}} \tag{2.15}$$

where

$$SS_T = (\frac{dlog_{10}(T(\Delta E))}{d(\Delta E/q)})^{-1} = \frac{2\sqrt{2}ln(10)h/(2\pi)}{-q\pi\sqrt{m_T E_g}\frac{dW_T}{d\Delta E}} \tag{2.16}$$

$$SS_{FD} = (\frac{dlog_{10}(F_{Integral})}{d(\Delta E/q)})^{-1} = \frac{ln(10)kT}{q}(1+exp(\frac{E_{vs} - E_{fs} - \Delta E}{kT})ln(\frac{(1 + exp(\frac{E_{fs}-E_{vs}+\Delta E}{kT})}{(1 + exp(\frac{E_{fs}-E_{vs}}{kT})}) \tag{2.17}$$

Simulations using the preceding equations performed at room temperature for a DG Si TFET with $m_T = 0.65m_0$, $N_A = 3E20$ cm^{-3}, $T_{ox} = 1$ nm, $T_{ch} = 10$ nm, and $E_g = 1.12$ eV resulted in Fig. 2.3. [4]

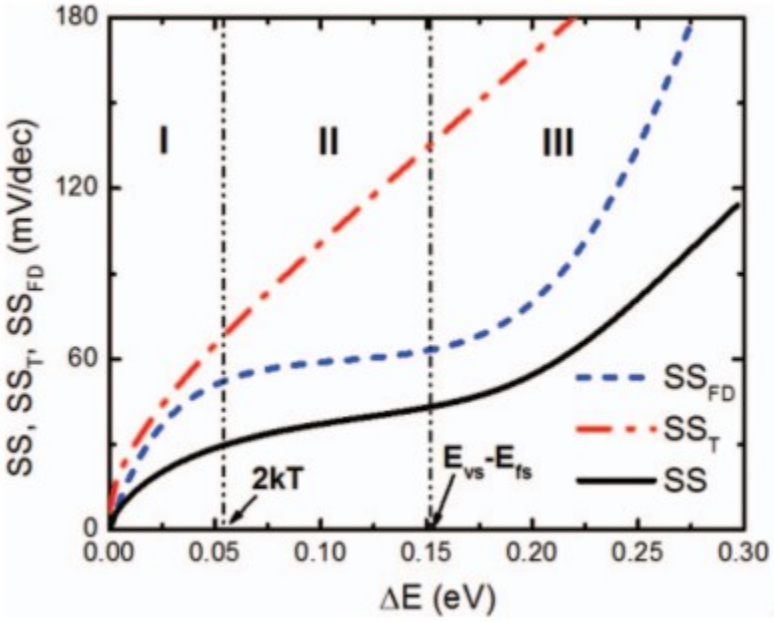

Figure 2.3: Simulated results of SS, SS_T, and SS_{FD} as affected by change in the width of the tunnel window Δ E.[2][4]

The ΔE axis of Fig. 2.3 is broken up into three regions corresponding to the

[2]Reprinted from (C. Wei, D. Sarkar, Y. Khatami, K. Jiahao, and K. Banerjee, Subthresholdswing physics of tunnel field-effect transistors, AIP Advances, vol. 4, no. 6, June 2014), with the permission of AIP Publishing.

significant changes in SS_{FD}. In region I, SS_{FD} simplifies to [4]

$$SS_{FD,RegionI} = \frac{ln(10)kT}{q}(1 - exp(\frac{-\Delta E}{kT})) \tag{2.18}$$

From this equation, as well as Fig. 2.3, it is observed that SS_{FD} exponentially approaches zero as the tunneling window decreases in size. According to Wei *et al*. this phenomenon is due to the FD distribution being truncated by the bandgap of the source region. It is this region of operation, referred to as the onset stage, that Wei *et al*. are most interested in because, as a result of the FD truncation phenomenon, the onset stage will result in the SS_{min} for the system. To further highlight this focus, recall that the first assumption made when deriving Eq. (2.2) is true for small ΔE only; thus, the resultant equations, including those for the various SS values, are only accurate for region I. Note that these equations, while not numerically accurate for $\Delta E > 2kT$, still provide approximate qualitative models for SS in regions II and III. [4]

It would follow from Eq. (2.15) and Eq. (2.18), as well as Fig. 2.3 that the SS at the onset stage would result in a near-zero SS, but this is not the case. The reason for this is that the OFF-current, (I_{OFF}) will dominate the low BTBT current, I_{BTBT}. An equation for OFF-current is as follows: [4]

$$I_{OFF} = \frac{2q}{\hbar}\int_{E_{cs}}^{+\infty} f_s(E)dE = \frac{2qkT}{\hbar}exp(\frac{E_g + E_{vs} - E_{fs}}{-kT}) \tag{2.19}$$

This equation for I_{OFF} does not include tunnel and gate leakage effects which would result from factors such as interface states near the tunneling junction. The effects of such interface states are a huge issue in TFETs, and this is discussed in depth in later sections, but it is beyond the scope of Wei's group's research on SS physics in Si and III-V TFETs. [4]

The hurdle posed by the OFF-current can be overcome and SS can be brought

down if the BTBT current in the onset stage, I_{ON}, is larger than I_{OFF}. The ratio between I_{ON} and I_{OFF} is called the onset strength of the device. Note that the minimum SS, SS_{min}, occurs when the BTBT current is equal to the OFF-current; that is,

$$SS_{min} = SS\Big|_{I_{OFF}=I_{BTBT}} \tag{2.20}$$

To determine the optimal material and electrostatic parameter values for establishing a large onset strength, four main TFET parameters: source doping level (N_A), natural length (λ), bandgap (E_g), and tunnel effective mass (m_T) are changed and their effects on I_{ON} and I_{OFF} are simulated. Fig. 2.4 illustrates these findings. [4]

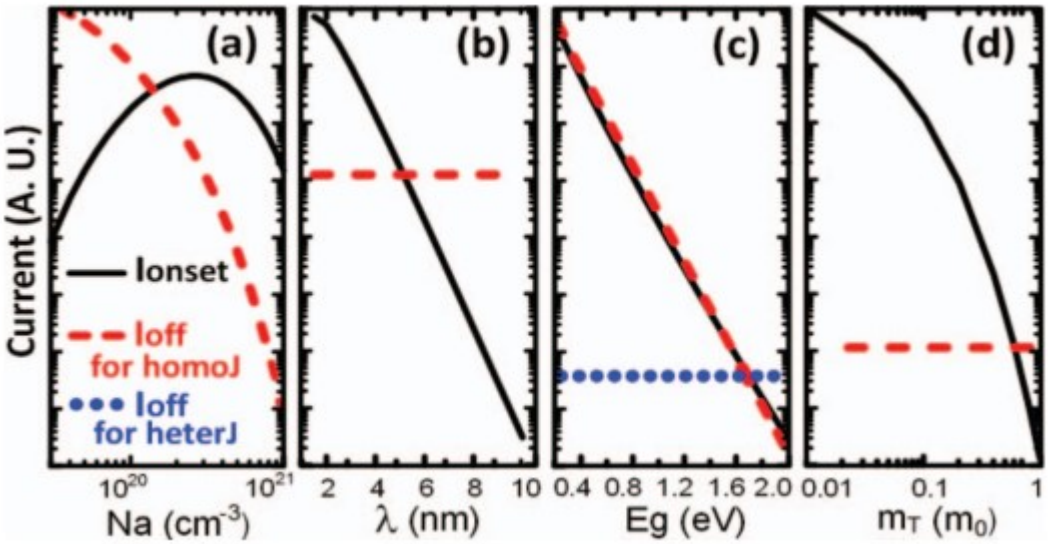

Figure 2.4: I_{BTBT} in terms of I_{ON} (referred to as I_{onset} in the graphs) and I_{OFF} for homojunction and heterojunction TFETs as functions of N_A, λ, E_g, and m_T.[3][4]

From Fig. 2.4 it can be seen that small λ and m_T are always desired and there is a simulated optimal N_A value of approximately 3E20 cm^{-3} that corresponds to maximized I_{ON}; for the latter, it is interesting to note that both lowering and increasing the doping past this optimal value will correspond to lowered onset strength. Also, for

[3]Reprinted from (C. Wei, D. Sarkar, Y. Khatami, K. Jiahao, and K. Banerjee, Subthresholdswing physics of tunnel field-effect transistors, AIP Advances, vol. 4, no. 6, June 2014), with the permission of AIP Publishing.

the case of heterojunction TFETs, small E_g is desired, while the relationship between bandgap and onset strength in homojunctions is not clear-cut. [4]

The final element of the total SS left to consider in pursuit of SS_{min} are the effects on SS of the tunneling probability, SS_T. Fig. 2.5 presents the effects of the four critical TFET parameters previously examined in terms of onset strength (that is: of N_A, λ, E_g, and m_T) on SS_{min} and SS_T evaluated at $\Delta E = 2kT$. [4]

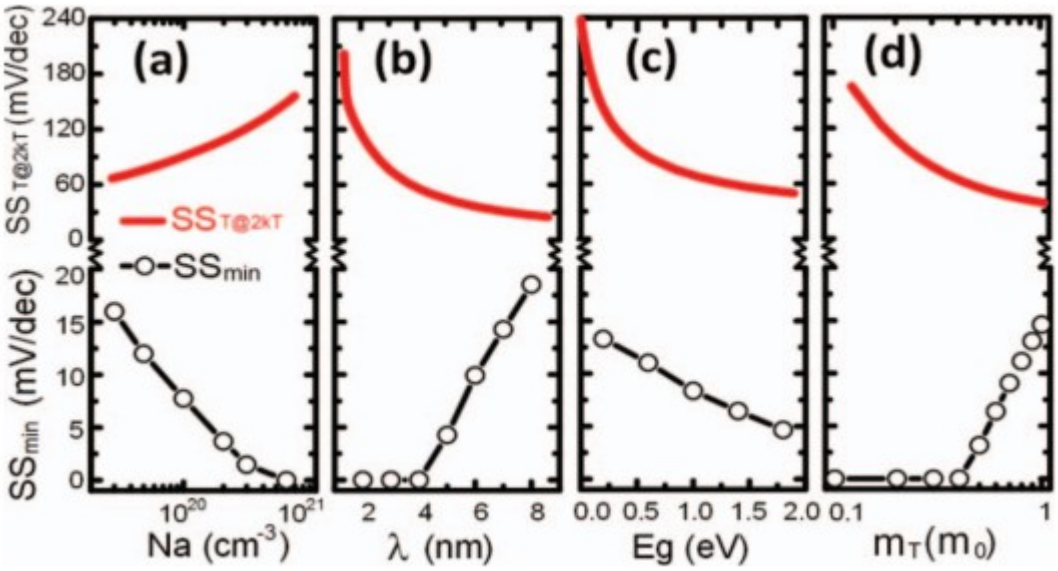

Figure 2.5: SS and $SS_{T@2kT}$ as functions of N_A, λ, E_g, and m_T.[4][4]

The results of Fig. 2.5 at first seem contrary to logic: $SS_{T@2kT}$ increases with increased N_A, and decreased λ, E_g, and m_T, even though tunneling efficiency is known to increase with these same changes in critical parameters. The reason for this is that the increased N_A, and/ or decreased λ correspond to a decrease in the depletion widths L_1 and/ or L_2, as seen in equations (2.11) and (2.12), respectively. These changes in turn correspond to a decrease in the minimum tunnel width W_T. TFETs with small tunnel widths are affected more strongly by junction electrostatic effects, and so the rate of change of W_T with respect to ΔE, $\frac{dW_T}{d\Delta E}.\frac{dW_T}{d\Delta E}$ will decrease accordingly

[4]Reprinted from (C. Wei, D. Sarkar, Y. Khatami, K. Jiahao, and K. Banerjee, Subthresholdswing physics of tunnel field-effect transistors, AIP Advances, vol. 4, no. 6, June 2014), with the permission of AIP Publishing.

for devices with increased N_A and/ or decreased λ. The effect this decrease in $\frac{dW_T}{d\Delta E}$, as well as the decrease in either or both other two parameters E_g and m_T, have on SS_T is clear from Eq. (2.16) where these terms are in the denominator and thus correspond to an increase in SS_T per their decrease. Wei *et al*. notes that this degradation in total SS through the effects of intrinsic properties on SS_T is often wrongly overlooked in the TFET community. [4]

Solutions to the problem of having both high I_{ON} and small SS suggested by Wei *et al*. include the use of heterojunction materials to boost tunneling, as well as using 2D semiconductors for the channel materials [4]. 2D semiconductors will be considered next.

2.3 2D Semiconductors and their applications in conventional FETs and TFETs

Atomic scale thickness is a huge benefit of using 2D semiconductors as channel materials in ever-shrinking FETs. Conventional bulk semiconductors such as Si can also be deposited at atomic thicknesses, but 2D semiconductors have multiple advantages over these bulk materials including dangling bond-free surfaces and fixed thicknesses which can be reproduced consistently for the chosen number of layers, resulting in minimal bandgap variation and carrier scattering. This is seen in Fig. 2.6 (a) and (b). [5]

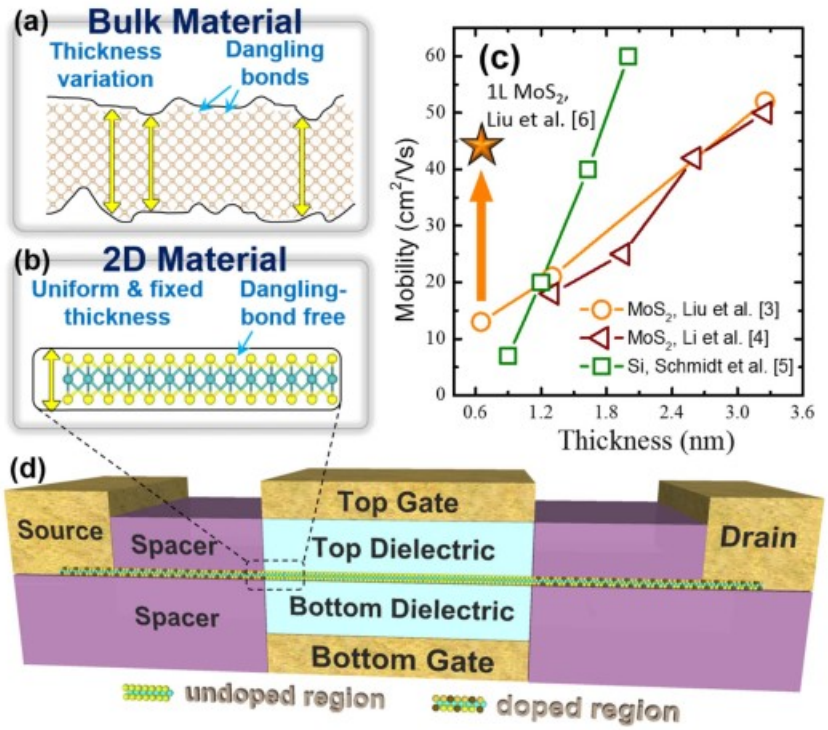

Figure 2.6: (a) and (b) demonstrate the advantages of using 2D materials over bulk materials, (c) the degradation of carrier mobility with smaller layer thicknesses, and (d) schematic of a DG 2D FET. IEEE ©2015.[5][5]

The atomic thicknesses capability of the 2D channel devices results in devices with superior electrostatics when compared to bulk channel devices; the fewer the number of layers, the better the electrostatics [5]. This is in part because the 2D materials provide increased gate control over the channel, resulting in higher electric fields at the junction [6]. Eq. (2.21) from Ilatikhameneh *et al.* can be used to explain this concept; note that the parameters for this equation are defined as part of the Wei *et al.* *SS* derivation [6].

$$\lambda = \sqrt{\frac{\epsilon_{ch}}{2\epsilon_{ox}}(1 + \frac{\epsilon_{ox}T_{ch}}{4\epsilon_{ch}T_{ox}})T_{ch}T_{ox})} \tag{2.21}$$

Scrutiny of Eq. (2.21) shows that the reduction of the channel thickness will also result in a reduction of the device λ, and this is known to result in higher electric

[5]Reprinted from (C. Wei, K. Jiahao, D. Sarkar, L. Wei, and K. Banerjee, 2d semiconductor fets-projections and design for sub-10 nm vlsi, IEEE Transactions on Electron Devices) with the permission of IEEE ©2015.

fields. The BTBT probability is exponentially dependent on the electric field, so atomically thin devices also result in better tunneling, which means higher I_{ON}. [6]

Another benefit to 2D materials is that thinning 2D materials will increase the bandgap significantly less than thinning a 3D material due to the weaker bonds between the layers of 2D materials. This is useful because increasing the bandgap corresponds to a shortening of the tunneling window which means that the I_{ON} will also be diminished. Besides this, monolayer 2D materials are known to have small dielectric constants which also corresponds to increased I_{ON}. [6]

While carrier mobility decreases with decreasing layer thickness for all materials, it is a slower decrease for molybdenum disulfide (MoS_2) than for Si, which results in MoS_2 having a higher mobility than Si at the monolayer (1L) level. One demonstrated hero device, as shown by Liu *et al.*, achieved a MoS_2 1L mobility of 44 $cm^2/V \cdot s$, significantly higher than the usual 13 $cm^2/V \cdot s$ for the same material. This can be seen in Fig. 2.6 (c). For comparison, consider that a 5 nm x 5 nm Si nanowire, given that a Si unit cell is known to be 0.545 nm, is about 9-10 monolayers in height. [5]

According to Wei *et al.* most theoretical simulations of 2D semiconductor-on-insulator (SOI) or DG FETs use inappropriate ballistic transport or poor back scattering simulations instead of dissipative transport theory, as is required for accurate predictions at and below the sub-10 nm node. Ballistic transport has been shown to overestimate drain current for 8 nm channel lengths. [5]

A balance must be struck between the scattering events considered during simulation and those ignored so that the simulations will be accurate but also computationally feasible. The approach taken by Wei *et al.* is summarized succinctly in Fig. 2.7. [5]

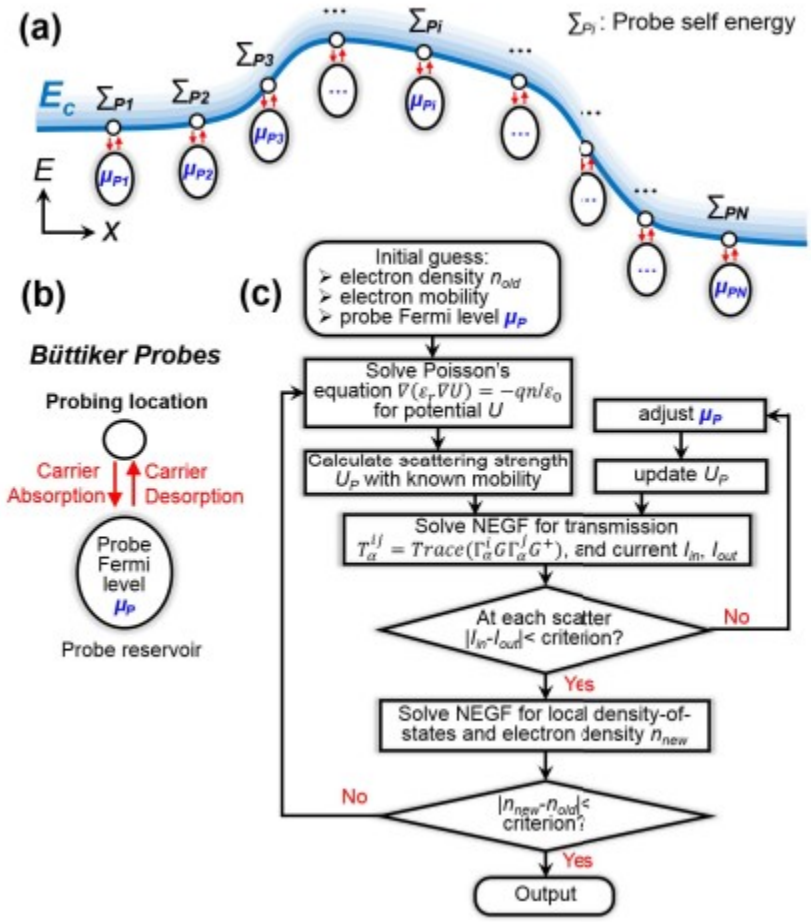

Figure 2.7: (a) E_C of a n-MOSFET in the channel region (that is, from source to drain) with *Büttiker* probes inserted at every mesh point along the channel. (b) A single *Büttiker* probe. (c) The simulation design. IEEE ©2015.[6][5]

For their simulations, Wei *et al.* use an approach adapted from Venugopal *et al.* [22] and Anantram *et al.* [23] use of *Büttiker* probes [24]; these are shown in Fig. 2.7 (a) and (b). The probes are inserted at each mesh point along the channel; each probe will take as its inputs the momentum and energy of the carriers at its location in the mesh, and its outputs will be the momentum and energy as changed by the predicted scattering events of the carriers at the probe's location. It is important to note that the probe will only affect the momentum and energy of the carriers at the

[6]Reprinted from (C. Wei, K. Jiahao, D. Sarkar, L. Wei, and K. Banerjee, 2d semiconductor fets-projections and design for sub-10 nm vlsi, IEEE Transactions on Electron Devices) with the permission of IEEE ©2015.

given point in the channel, and not the quantity of carriers passing through. The function of the probe is as follows: [5, 22, 23, 24]

1. Take as inputs the momentum and energy of the carriers;
2. Solve Poisson equation for the relevant electrostatics;
3. Solve the effective mass transport equation with a nonequilibrium Green's function (NEGF) for charge distribution and transmission;
4. Adjust the Fermi levels so that the net current at each probe is maintained to be zero;
5. Solve NEGF again, this time for carrier density and density of states (DOS);
6. Determine the appropriate scattering strength (U_P) from the carrier density and DOS;
7. Finally, output the momentum and energy of the carriers as affected by the calculated scattering strength.

In comparison, Ilatikhameneh *et al.*'s simulations are based on tight-binding (TB) with a Poisson-quantum transmitting boundary method (QTBM) methodology. This is equivalent to a more efficient form of solving the NEGF without scattering and is performed by the NEMO5 simulation tool available through the NanoHub at Purdue University. Because such simulations do not consider the scattering they can be done computationally faster than those performed by Wei *et al.* but are also less accurate. The monolayer TMD TFET simulated by Ilatikhameneh *et al.* is seen in Fig. 2.8 and has the following parameters: channel length= 15 nm, source/drain length = 10 nm, T_{ox}= 0.43 nm, and N_A/N_D= 1x10^{20} cm^{-3}. [6]

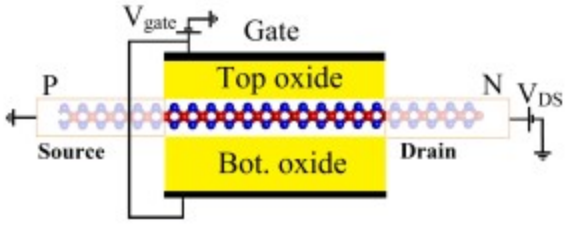

Figure 2.8: Monolayer TMD TFET structure. IEEE ©2015.[7][6]

Short-channel effects caused by lateral electric fields (that is, strong electric fields caused by the source/ drain depletion regions being too close together) diminish control of the gate and are a widespread problem in short-channel bulk semiconductor FETs. These short-channel effects do not occur to the same degree in FETs with 1L to three-layer (3L) 2D semiconductor channels because such channels are too thin to maintain the significant lateral electric field strength. Instead, most of the lateral electric fields in FETs with 1L to 3L 2D semiconductor channels occur in the gate dielectric and through the spacers. Low-k dielectric materials are effective in muzzling the lateral electric fields, but high-k materials provide better gate control; thus, a compromise is reached in device design by selecting gate materials with high-k and spacer materials with low-k. [5]

1L to 3L SOI and DG FETs with MoS_2 channel simulations consistently surpassed the SS and I_{ON} values simulated for Si ultrathin-body DG FETs. The DG 2D-channel devices outperformed the SOI 2D-channel devices for 2L and 3L due to the effects of the added lateral electric field through the 50 nm bottom gate dielectric of the latter device; for this reason, the DG 2D-channel device is considered superior to the SOI 2D-channel device. [5]

Low-standby-power (LSTP) applications require high threshold voltage (V_{th}), which corresponds to lowered I_{ON}. In contrast, high performance (HP) applications

[7]Reprinted from H. Ilatikhameneh, T. Yaohua, B. Novakovic, G. Klimeck, R. Rahman, and J. Appenzeller, Tunnel-field effect transistors in 2-d transition metal dichalcogenide materials, IEEE Journal on Exploratory Solid-State Computational Devices and Circuits) with the permission of IEEE © 2015.

require high I_{ON}, which corresponds to lowered V_{th}, and high-standby-power consumption. LSTP is a direct function of SS, and HP is instead a function of device parameters such as carrier mobility and DOS. Simulations by Wei *et al.* show better performance for MoS_2 FETs than for Si FETs for both HP and LSTP; the best device for HP is 2L, and the best device for LSTP is 1L. Devices with channels thicker than 3L will have significantly degraded electrostatics, outweighing the benefits of the higher DOS and increased carrier mobility provided by the increased layer thicknesses; thus, such channels should not be used for sub-10 nm nodes. According to the simulations, the LSTP requirement cannot be met with a MoS_2 channel device beyond the 7 nm node. [5]

High carrier mobility and relatively low effective mass m_0 are desired for all applications; while high mobility is always desired, care must be taken to ensure that the latter is not excessively small as this can result in increased source-to-drain tunneling leakage. Fig. 2.9 includes available data on material mobility and corresponding effective mass of 2D TMD semiconductors based on experiments and calculations performed by various groups as presented by Wei *et al.* [5]

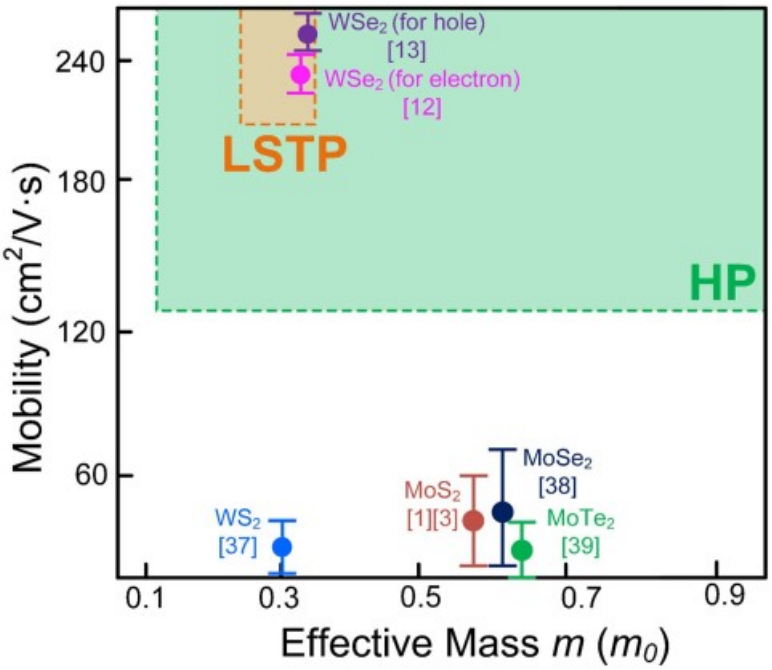

Figure 2.9: Mobility and effective mass data for various 2D semiconductors. The green block corresponds to the ranges required for HP operation; the orange block corresponds to the ranges required for LSTP operation. IEEE ©2015.[8][5]

From Fig. 2.9, WSe_2 is clearly the better material in terms of both effective mass and mobility. In fact, WSe_2 is capable of meeting all requirements down to the 5.9 nm node without any advanced techniques such as strain engineering, which is required of materials such as MoS_2 beyond the 7 nm node. [5]

Workable solutions for the sub-5 nm nodes include the use of anisotropic 2D materials and TFETs. An anisotropic material has different effective masses along the x- and z- planes; it has been found that a large effective mass in the transport or z-plane m_z can increase the density of states and boost I_{ON}. As seen in Fig. 2.10, this results in useable materials for HP applications beyond the 5 nm node, but is not useful for LSTP applications. [5]

[8]Reprinted from (C. Wei, K. Jiahao, D. Sarkar, L. Wei, and K. Banerjee, 2d semiconductor fets-projections and design for sub-10 nm vlsi, IEEE Transactions on Electron Devices) with the permission of IEEE ©2015.

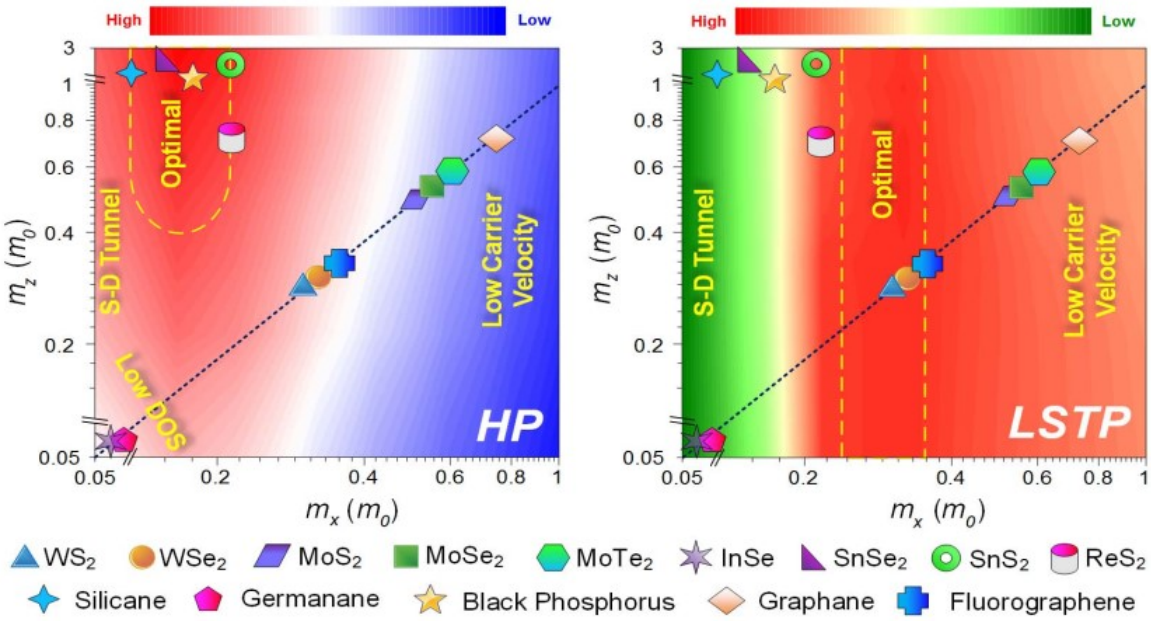

Figure 2.10: I_{ON}, seen as a color contour, is plotted as a function of effective mass along the x- and z- planes for HP (right) and LSTP (left) applications at the 5.9 nm node. The dashed blue lines correspond to isotropic materials. IEEE ©2015.[9][5]

Ilatikhameneh *et al.* simulated multiple TMD TFETs with fixed I_{OFF}= 1 nA/μm at V_G= 0 V. The results are seen in Fig. 2.11.

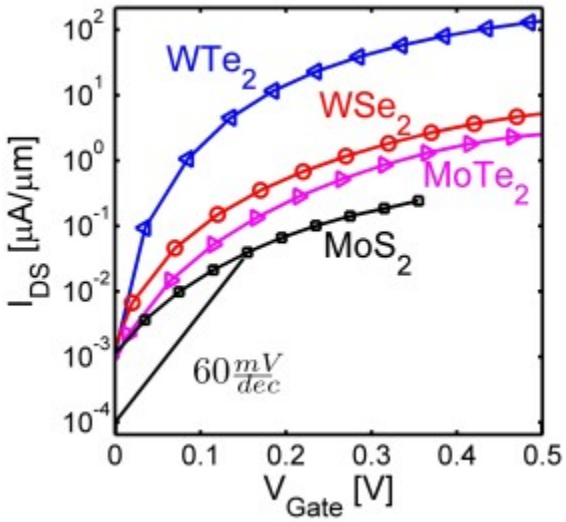

Figure 2.11: The transfer characteristics of various simulated TMD TFETs by Ilatikhameneh *et al.* IEEE ©2015.[10][6]

[9]Reprinted from (C. Wei, K. Jiahao, D. Sarkar, L. Wei, and K. Banerjee, 2d semiconductor fets-projections and design for sub-10 nm vlsi, IEEE Transactions on Electron Devices) with the permission of IEEE ©2015.

Fig. 2.11 shows that optimal TMD gate material is WTe_2, both in terms of *SS* and I_{ON}. This is due to factors such as its small bandgap and effective mass. These and other material parameters as well as the simulated results are seen in Table 2.1. [6]

Table 2.1: Data corresponding to the TMD TFET simulations seen in Fig.2.11. Note that effective mass/m_0 is referred to as the reduced effective mass, m_r^*. IEEE © 2015. [11][6]

Material	I_{ON} (μA/μm)	E_g (eV)	m_r^*	λ (nm)
WTe_2	127	0.75	0.17	0.45
WSe_2	4.6	1.56	0.21	0.41
$MoTe_2$	2.3	1.08	0.32	0.5
MoS_2	0.3	1.68	0.29	0.38

From these results WTe_2 would seem the clear winner for use as a channel material with a simulated I_{ON} almost 28 times as large as that of WSe_2 [6]. This conclusion sadly cannot be compared to Wei *et al.*'s findings because that group did not simulate WTe_2. They can, however, be compared to Fei *et al.*'s simulated results for 6 different TMD TFETs with channel lengths of 12 nm and V_D= 0.5 V [8]. These results are listed in Table 2.2.

Table 2.2: TMD TFET simulations by Fei *et al.* m_e/m_0 is the reduced electron effective mass, and m_h/m_0 is the reduced hole effective mass. IEEE © 2016.[12][8]

Material	E_g (eV)	$m_e(m_0)$	$m_h(m_0)$	SS_{min}
MoS_2	1.66	0.42	0.54	48.3
WS_2	1.81	0.30	0.39	56.1
$MoSe_2$	1.43	0.48	0.59	49.4
WSe_2	1.54	0.32	0.41	58.6
$MoTe_2$	1.07	0.39	0.54	58.6
WTe_2	1.07	0.25	0.34	71.2

[10]Reprinted from (H. Ilatikhameneh, T. Yaohua, B. Novakovic, G. Klimeck, R. Rahman, and J. Appenzeller, Tunnel-field effect transistors in 2-d transition metal dichalcogenide materials, IEEE Journal on Exploratory Solid-State Computational Devices and Circuits) with the permission of IEEE © 2015.

[11]Reprinted from (H. Ilatikhameneh, T. Yaohua, B. Novakovic, G. Klimeck, R. Rahman, and J. Appenzeller, Tunnel-field effect transistors in 2-d transition metal dichalcogenide materials, IEEE Journal on Exploratory Solid-State Computational Devices and Circuits) with the permission of IEEE © 2015.

Table 2.2 tells a different story in terms of the best TMD channel material because it lists the SS_{min} values for each of the materials, and WTe_2 is the highest and worst of these. This is because smaller bandgap and effective mass, as is the case for the monolayer WTe_2, results in lower I_{ON} but smaller onset strength and thus higher SS_{min}. According to this data, MoS_2 would be the best TMD material to use, though it has been shown that this is untrue from the Wei *et al*. paper. [8] The trade-off of *SS* and onset strength must be considered when choosing the TMD channel material and makes the choice more difficult than at first expected. It should be noted that Seabaugh *et al*. mention that as of 2015 no fabricated TMD TFETs have shown sub-60 mV/decade *SS*.

For LSTP applications, TFETs with TMD channels are a viable solution due to the numerous established advantages of 2D semiconductors. These include restraint on tunneling leakage and therefore improvement of *SS* due to the dangling bond-free surface of a 2D semiconductor, as well as increased gate control and increased I_{ON} caused by having an ultrathin body. [5] Next, focus will shift on the effects of having an ultrathin body in TFETs, as seen through an analysis of channel geometry, namely in terms of fin thickness and channel length.

2.4 The Effects of Channel Geometry on TMD TFETs

Electric fields responsible for tunneling of up to approximately 20 MV/cm have been observed in DG *p*-gallium nitride/*intrinsic*-indium nitride/*n*-gallium nitride (*p*-GaN/InN/*n*-GaN) fin TFET tunnel junctions; this is five times higher than the maximum electric fields observed in IV and III-V tunnel junctions. The reason for this is that this stack uses the physics of the heterojunction to positively influence tunneling capabilities: specifically, InN has a bandgap of 0.7 eV which is narrow compared to

[12]Reprinted from (L. Fei, W. Jian, and G. Hong, Atomistic simulations of device physics in monolayer transition metal dichalcogenide tunneling transistors, IEEE Transactions on Electron Devices) with the permission of IEEE © 2016.

the GaN bandgap of 3.2 eV. The narrow InN bandgap is responsible for increased inter-band tunneling and the wide GaN bandgap suppresses the OFF-current of the TFET device. Fig. 2.12 is the device and its corresponding band diagram. [7]

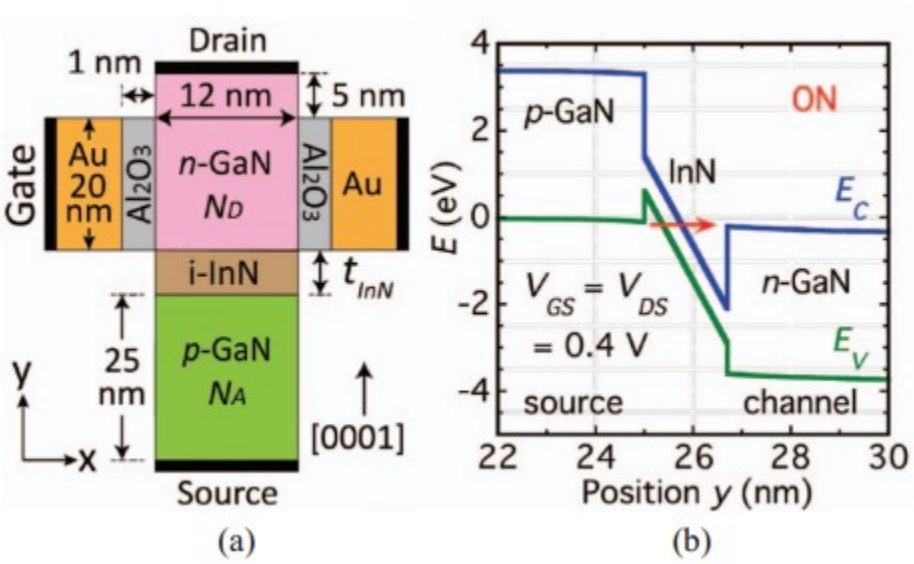

Figure 2.12: (a) The TFET structure used for simulations, and (b) the simulated energy band diagram of this device. IEEE © 2015.[13][7]

Dependences on the fin thickness L_D and the drain (that is, the n-GaN layer) doping N_D are observed from simulated transfer characteristics for a DG p-GaN/InN/n-GaN TFET device. The transfer characteristics, which can be seen in Fig. 2.13, correspond to the drain current per unit width I_D/W, a variable synonymous to the tunnel current, as a function of changing V_{GS}. [7]

[13]Reprinted from (A. Seabaugh, S. Fathipour, W. Li, H. Lu, J. H. Park, A. C. Kummel, D. Jena, S. K. Fullerton-Shirey, and P. Fay, Steep subthreshold swing tunnel fets: Gan-inn-gan and transition metal dichalcogenide channels, 61st IEEE International Electron Devices Meeting) with the permission of IEEE © 2015.

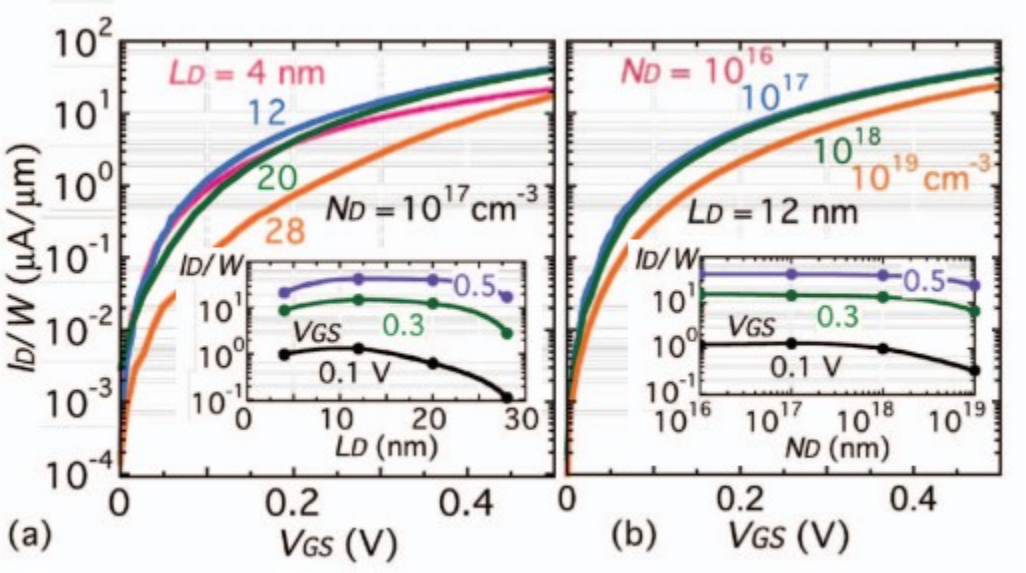

Figure 2.13: Synopsis TCAD transfer characteristics of (a) drain doping, and (b) fin thickness dependence, with the device parameters as follows: gate length L_G = 20 nm, thickness of the InN layer t_{InN} = 1.7 nm, thickness of the GaN layers $t_{p-GaN} = t_{n-GaN}$ = 25 nm, equivalent oxide thickness EOT = 0.43 nm, and V_{DS} = 0.5V. IEEE © 2015.[14][7]

Assuming a fixed drain doping N_D of 1x10^{17} cm^{-3}, an optimum fin thickness L_D is found to be between 10 to 20 nm; for $L_D < 10$ nm, the I_D/W will start to decrease as the current cross section diminishes; similarly, for $L_D > 20$ nm, the I_D/W will also decrease, though in this case as a result of lowered gate electrostatic control with increased L_D. Assuming a fixed fin thickness L_D of 12 nm, increasing the drain doping $N_D >$ 1x10^{18} cm^{-3} increases the density of carriers in the channel, thus reducing the number of free states available for tunneling to occur; this directly correlates to a decrease in tunnel current; contrarily, for changing $N_D <$ 1x10^{18} cm^{-3}, the tunnel current will remain unchanged. [7]

To supplement these findings, the behavior of a different device with changing channel length is explored in the Fei *et al.* paper. The device is a DG TFET with the monolayer $MoTe_2$ used as the gate material. Unlike the device explored in the

[14]Reprinted from (A. Seabaugh, S. Fathipour, W. Li, H. Lu, J. H. Park, A. C. Kummel, D. Jena, S. K. Fullerton-Shirey, and P. Fay, Steep subthreshold swing tunnel fets: Gan-inn-gan and transition metal dichalcogenide channels, 61st IEEE International Electron Devices Meeting) with the permission of IEEE © 2015.

Seabaugh *et al.* paper, this DG device, seen in Fig. 2.14 along with the atomistic structures of the monolayer along the armchair (AD) and zigzag (ZD) directions, is not a fin TFET, and so instead of the fin-thickness L_D, the channel length L_G is varied and observed. [8]

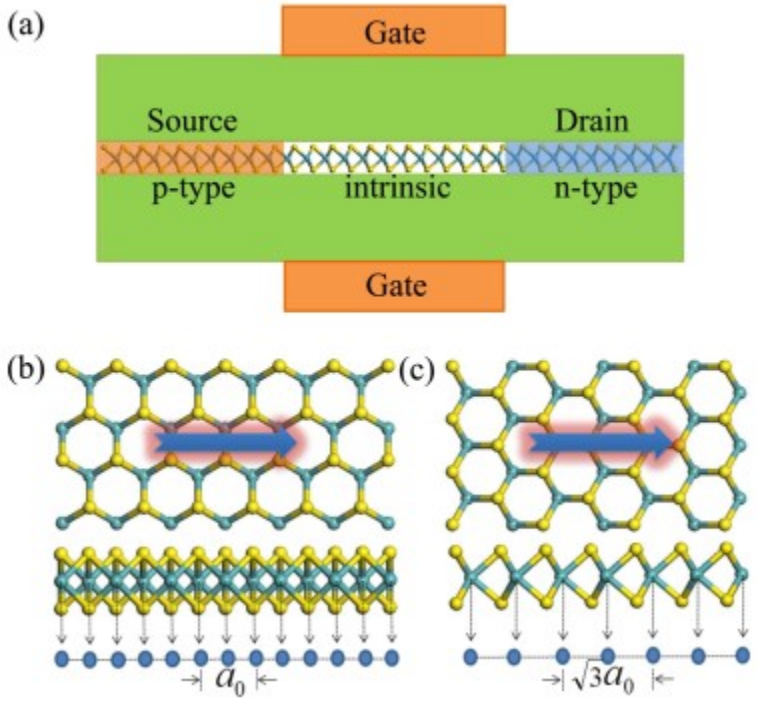

Figure 2.14: (a) The DG monolayer TMD TFET device structure, (b) the atomistic structure of the TMD monolayer along the ZD direction, and (c) the atomistic structure of the TMD monolayer along the AD direction. IEEE © 2016.[15][8]

Fei *et al.* notes that the performance of the TMD TFET is orientation dependent; for example, ZD can lead to higher I_{ON}, but no NDR, whereas AD has a very large NDR. These differences are, however, beyond the scope of this study. [8]

In the corresponding simulation which uses the TMD material $MoTe_2$, the channel length L_G is varied from 5 nm to 20 nm in increments of 5 nm with the drain voltage $V_D = 0.5$ V. The general transfer characteristics of the device with different gate lengths are shown in Fig. 2.15. [8]

[15]Reprinted from (L. Fei, W. Jian, and G. Hong, Atomistic simulations of device physics in monolayer transition metal dichalcogenide tunneling transistors, IEEE Transactions on Electron Devices) with the permission of IEEE © 2016.

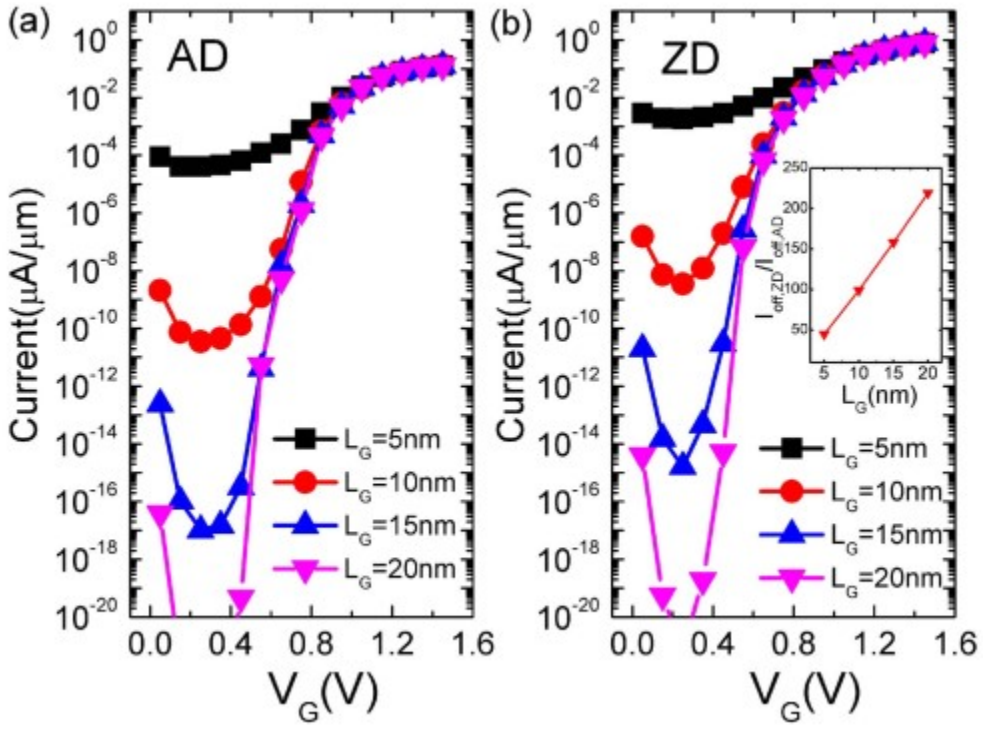

Figure 2.15: The simulated MoTe2 TFET transfer characteristics for different channel lengths in the (a) AD, and (b) ZD directions. IEEE © 2016.[16][8]

Two conclusions can be drawn from Fig. 2.15: larger L_G corresponds to smaller OFF-current, and the I_{ON} is not a function of channel length. [8] From these two papers, the impact of the channel geometry of different devices has been studied and determined to be a significant source of variation in terms of device behavior.

2.5 TMD Coupling in TFETs

Heterogeneous TFETs can be made by stacking p-n junctions of different TMD materials into what is known as *couple* configurations. To determine the most optimal such couples, Gong *et al*. characterizes the individual TMD materials based on band alignment. The results are seen in Fig. 2.16. [9]

[16]Reprinted from (L. Fei, W. Jian, and G. Hong, Atomistic simulations of device physics in monolayer transition metal dichalcogenide tunneling transistors, IEEE Transactions on Electron Devices) with the permission of IEEE © 2016.

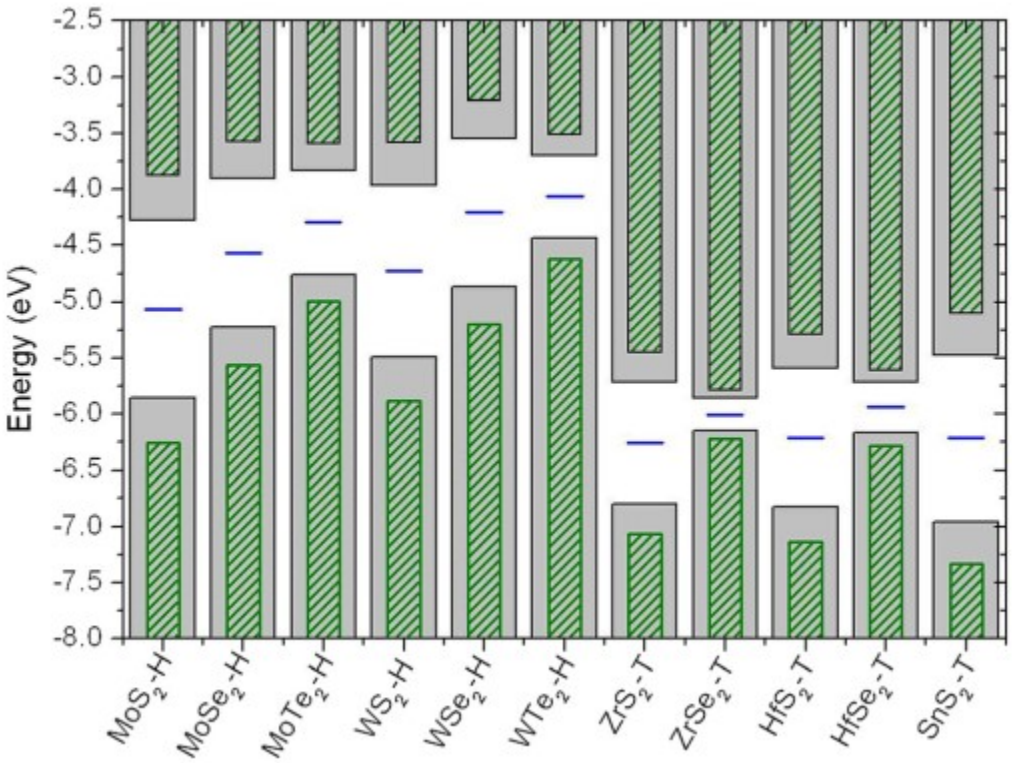

Figure 2.16: Band alignment of various monolayer TMD materials. The grey columns correspond to the conduction band minimum and valence band maximum and the green columns are the corrected band edges. The Fermi level of each material is the blue line, and the vacuum level is set at 0 eV.[17][9]

According to Fig. 2.16, electrons at the E_V of WTe_2 and $MoTe_2$ could easily tunnel into the E_C of ZrS_2, $ZrSe_2$, HfS_2, and $HfSe_2$. Gong *et al.* suggests the following couplings: n-type source as WTe_2, WSe_2, $MoTe_2$, or $MoSe_2$ with p-type drain as ZrS_2, $ZrSe_2$, HfS_2, or $HfSe_2$. [9] This is an interesting and note-worthy application of TMDs in TFETs because it uses the TMD materials for what would typically be the source/drain regions. When the two energy bands meet and open a tunneling window, the channel is created out of these regions without the use of an intrinsic layer.

[17]Reprinted from (C. Gong, H. Zhang, W. Wang, L. Colombo, R. M. Wallace, and K. Cho, Band alignment of two-dimensional transition metal dichalcogenides: Application in tunnel field effect transistors, Applied Physics Letters, vol. 103, no. 5, 2013) with the permission of AIP Publishing.

Chapter 3

Quantum Simulation Theory

3.1 The Necessity of Quantum Simulations

Computer-aided design is the first step to reducing fabrication cost of new devices, but determining the required software to use can be a challenge. This is considered.

Tunneling is calculated based on the assumption of straight-line tunneling paths in the popular dynamic nonlocal band-to-band (DNL) simulation method, whereas in the non-equilibrium Green's function (NEGF) method, the electrostatic potentials are obtained from self-consistent semiclassical Poisson calculations. Software packages such as Silvaco primarily use DNL-type simulations, whereas VASP and nanoHub's NEMO are both quantum-based. Determining which type of simulation software to use when simulating the desired devices is the necessary first step to conducting novel research. The Rochester Institute of Technology's Microelectronic Engineering department has a license for Silvaco's Athena software at the time of this writing, so this was the evident choice before massive drawbacks were recognized. The largest of these is illustrated in the example by Jiang *et al.*; Fig. 3.2 compares simulation results from DNL and NEGF results in a AlGaSb/InAs TFET (see Fig. 3.1 for the simulated device geometry). The simulation results in this paper follow from experimental results by Zhou et al. The parameters being varied in the simulations are gate length (L_g) and undercut length (L_{uc}). [25]

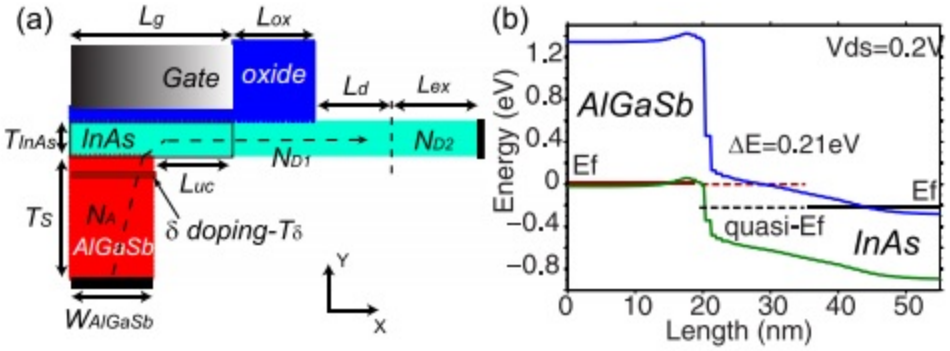

Figure 3.1: (a) Device geometry of the simulated TFET design. (b) Band profile plotted along dashed line in (a). IEEE ©2015.[1][10]

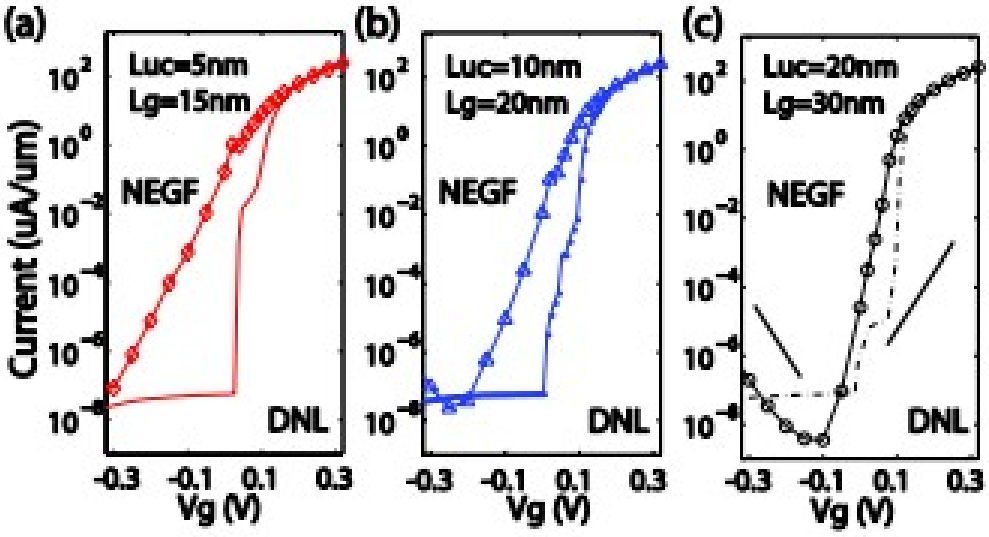

Figure 3.2: Comparisons of dynamic nonlocal band-to-band (DNL) and non-equilibrium Green's function (NEGF) simulation results. Note that the straight-lines correspond to the DNL simulations and the lines with the bullets correspond to the NEGF simulations. IEEE ©2015.[2][10]

It is seen that the NEGF simulation results in a higher *SS* than the DNL method. This observed difference is because the DNL model underestimates the contributions from the direct source–drain tunneling in the simulated geometries. NEGF simulations also take quantum-level scattering into consideration. Fig. 3.2 is an extreme

[2]Reprinted from (Z. Jiang, Y. Lu, Y. Tan, Y. He, M. Povolotskyi, T. Kubis, A. C. Seabaugh, P. Fay, and G. Klimeck, Quantum transport in algasb-inas tfets with gate field in-line with tunneling direction, IEEE Transactions on Electron Devices) with the permission of IEEE © 2015.

exaggeration of the required results because the experiment will look worse than the TCAD simulation. Thus, the atomistic model produced via NEGF simulations is required to show negative differential resistance (NDR) in the simulations. Determining NDR is pivotal to simulating both Esaki diodes and especially TFETs, so an appropriate quantum simulator must be selected to continue with this research.

3.2 Choosing a Quantum Simulation Package

3.2.1 The Vienna Ab initio Software Package

The Vienna Ab initio Software Package (VASP) 5.4 is a simulation package capable of computing an approximate solution to the many-body Schrödinger equation either by solving the Kohn-Sham equations which will be discussed later in this chapter or by other methods such as the Hartree-Fock solution. It has built-in Born-Oppenheimer molecular dynamics, spin-orbit coupling, and strain application capabilities, among many others. VASP is frequently used in the semiconductor industry for interface studies and is one of few software packages capable of simulating non-standard interfaces such as the 2D TMDs of interest in this study. The VASP 5.4 package was commercially complied for RIT by Materials Design, Inc. as a part of their MedeA software. Appendix B in this document offers a simple tutorial for using MedeA 2.22.2 for a general VASP 5.4 simulation.

3.2.2 NanoHUB's NEMO

NEMO5 is offered and supported by the NanoHUB at Purdue University. There are approximately 500 NEMO5 users, some industrial and most academic. NEMO5 can solve band structure or energy-momentum ($E - k$) problems directly through user-selected solvers, the most common being the non-equilibrium Green's function (NEGF). It is also capable of plotting I-V characteristics of devices built in the in-

put deck of the file. In contrast with VASP, which is an Ab initio package, NEMO uses empirical tight-binding which has been fit to VASP band structures. For further reading, consider Yaohua Tan's thesis from Purdue University. In this thesis, a comparison is made as a sanity check. [26]

Fig. 3.3 shows the basic NEMO5 simulation flow.

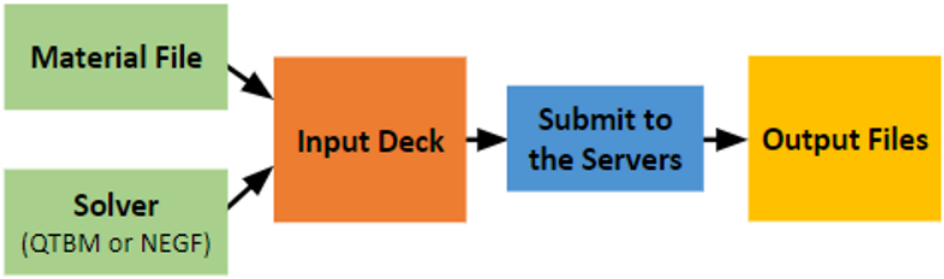

Figure 3.3: NEMO5 Simulation flow.

As mentioned previously, simulations should have a fundamental basis on experimental results. The simulation results must be compared to real data to determine if they correspond to anything true. The best way to do this is to start with existing experimental data and try to recreate them using simulations. Such simulations follow in the next chapter.

3.3 Quantum Simulation Theory

3.3.1 The Single-Body Problem

The energy-momentum $(E - k)$ relationship of a crystalline solid is most often obtained by solving the Schrödinger equation for a one-electron problem. The Schrödinger equation defines the total energy of a system and is as follows:

$$\hat{H}(x)\phi(x) = \frac{-\hbar^2}{2m}\frac{d^2\psi(x)}{dx^2} + V(x)\psi(x) = E\psi(x). \tag{3.1}$$

A hydrogen atom is composed of a single electron and a proton. In spherical

coordinates, the Schrödinger equation for such a problem is shown in Eq. 3.2, with Fig. 3.4 explaining the spherical coordinates.

$$\hat{H}(r,\theta,\phi)\psi(r,\theta,\phi) = E\psi(r,\theta,\phi). \tag{3.2}$$

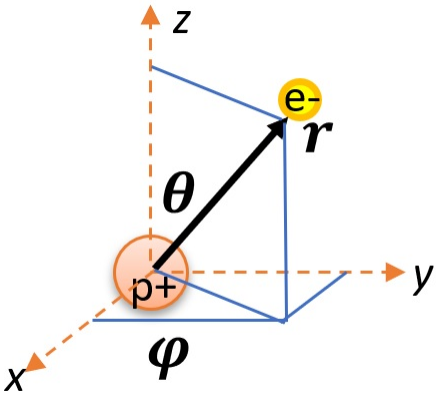

Figure 3.4: The spherical coordinates of a hydrogen atom.

This single-electron problem can be solved explicitly. [27, 28, 29, 30]

3.3.2 Orbitals

The hydrogen atom wavefunctions, $\psi(r,\theta,\phi)$, are the atomic orbitals. An atomic orbital is a function that describes one electron in an atom. It is important to understand the orientation and restrictions of each orbital when doing quantum simulations. Fig. 3.5 shows the s, p and d orbitals and their various allowed states.

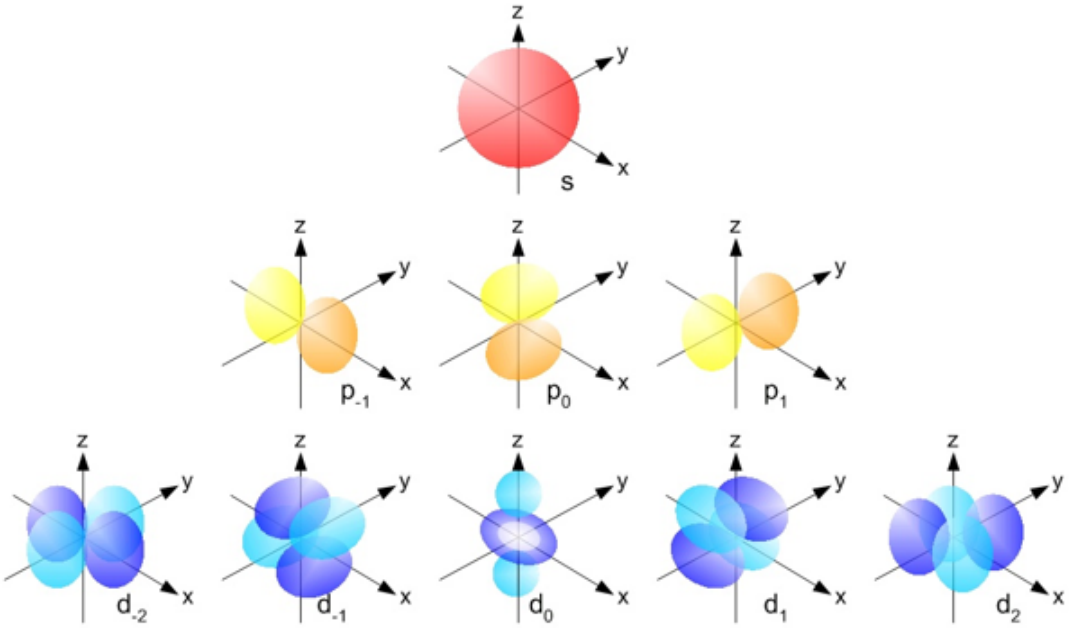

Figure 3.5: Electron configuration in each orbital. [11, 12]

As shown by Vogl *et al.* and Jancu *et al.*, quantum models including an excited s-like orbital, s^*, and excited d orbitals improve the simulation model fits of $E - k$ and effective mass plots. [31, 32, 33] This makes the relevant states for the type of quantum simulations of interest s, p, and d. The s-sublevels have one orbital and can hold two electrons. The s-orbital only forms sigma bonds. The p-sublevels have three orbitals and can hold six electrons. The p-orbital forms both sigma and pi bonds. The d-sublevels have five orbitals and can hold ten electrons. The d-orbital forms sigma, pi, and delta bonds. [11, 12, 34]

3.3.3 Density Functional Theorem

In real world applications the systems of interest are extremely complicated; there is no such thing as a "single-body" problem such as the solution for the hydrogen atom expressed earlier outside an introductory course in quantum mechanics. The systems of interest, at least in the semiconductor industry, are "many-body" solids. The relevant interactions to consider when solving a many-body quantum system are

the following:

- The nuclei kinetic energy,
- The electron kinetic energy,
- The nuclei Coulombic interactions,
- The electron Coulombic interactions,
- And the nuclei-electron Coulombic interactions.

The solid's behavior can be described by the wavefunction $\psi(r, \theta, \phi)$, which can in turn be found by solving the Schrödinger equation. But of course, a Schrödinger equation relating potentially millions of interactions as can be present at a transistor's interface is not the sort of problem that can be solved explicitly. Instead, the problem must be significantly simplified by eliminating some of the interactions listed above. [35, 36]

One specific solution to dealing with many-body Schrödinger equations is using the density functional theory (DFT). This is based on multiple simplifications which will be covered in the following cursory overview. [35, 36]

The first of these simplifications is the Born-Oppenheimer approximation. This approximation states that the wavefunction depends primarily upon the nuclear part of the atomic system. The nuclear motion is significantly slower than the electron motion due to the former's weight, and so it can be considered fixed. Therefore, only the position of the nuclei and not their velocity needs to be considered when performing calculations, reducing the required degrees of freedom drastically. [35, 36]

After the Born-Oppenheimer approximation is applied, the nuclei are now considered fixed in space, so they have no kinetic energy, and their Coulombic interaction with each other is a fixed value so it doesn't affect the solution. The only term where the nuclei still have an effect is in the nuclei-electron Coulombic interactions, and

this term comes to define which type of problem is being solved because it determines what molecule is being considered. In DFT context, this is often called the external potential because the nuclei determine the Coulombic potential in which the electrons move, and this defines the problem being solved. In summary, the relevant interactions are now:

- The electron kinetic energy,
- The electron Coulombic interactions,
- And the nuclei-electron Coulombic interactions (also known as the external potential).

The second simplification required for DFT is the Hohenburg-Kohn theorem. Note that a proof of this theorem is included in Appendix A. This theorem states that the electron density, ρ, of any system determines every ground-state property of the system. That is, the total ground state energy of a many-electron system is a function of the density, so therefore, if the electron density function is known, so too is the total energy of the system. This means that using this electron density function, all other ground state properties can be calculated. A simpler way to think of this is the following: every external potential corresponds to one specific wavefunction which corresponds to one specific density function. Thus, the wavefunction can be taken out and the external potential can be connected directly to a specific density function, with no information loss. [35, 36, 37]

In DFT the many-body Schrödinger equation is transformed into single-particle Kohn-Sham equations, which are the types of equations that are solved through a software like VASP. [35, 36] The Kohn-Sham equations are seen in equations 3.3 and 3.4:

$$\widehat{H_{ks}(\hat{r})} = \frac{-1}{2}\Delta^2 + v_{ks}(\hat{r}) \tag{3.3}$$

$$v_{ks}(\hat{r}) = v_{ext}(\hat{r}) + v_H(\hat{r}) + v_{xc}(\hat{r}) \tag{3.4}$$

where $\widehat{H_{ks}(\hat{r})}$ is the effective Hamiltonian, $v_{ks}(\hat{r})$ is the effective Kohn-Sham potential, $v_{ext}(\hat{r})$ is the external potential, $v_H(\hat{r})$ is the Hartree potential, and $v_{xc}(\hat{r})$ is the exchange-correlational potential. [35, 36, 37]

These equations operate by replacing the electrons in the crystal with non-interacting quasi-electrons. These new electrons are now only interacting with nuclei and not themselves. Next, an external field called the exchange-correlational field is applied to correct for the omitted interaction. The field is derived from the exchange-correlation potential, and if this functional is known the prediction that is made is without any accuracy loss. [35, 36, 37]

The most important part of performing a DFT-type calculation is the choice of the exchange-correlation functional. There is no rule for finding the best functional and often the way to do this is to make an educated guess and go from there until the functional begins predicting experimental values as closely as possible. [35, 36]

3.3.4 Jacob's Ladder

Jacob's ladder is an idea developed by Perdew and Schmidt which considers the efficiency and accuracy of using various methods for finding the external correlational functional. Fig. 3.6 shows a graphical representation of this idea. It shows the sacrifice in simulation simplicity that is often required to obtain accurate results.

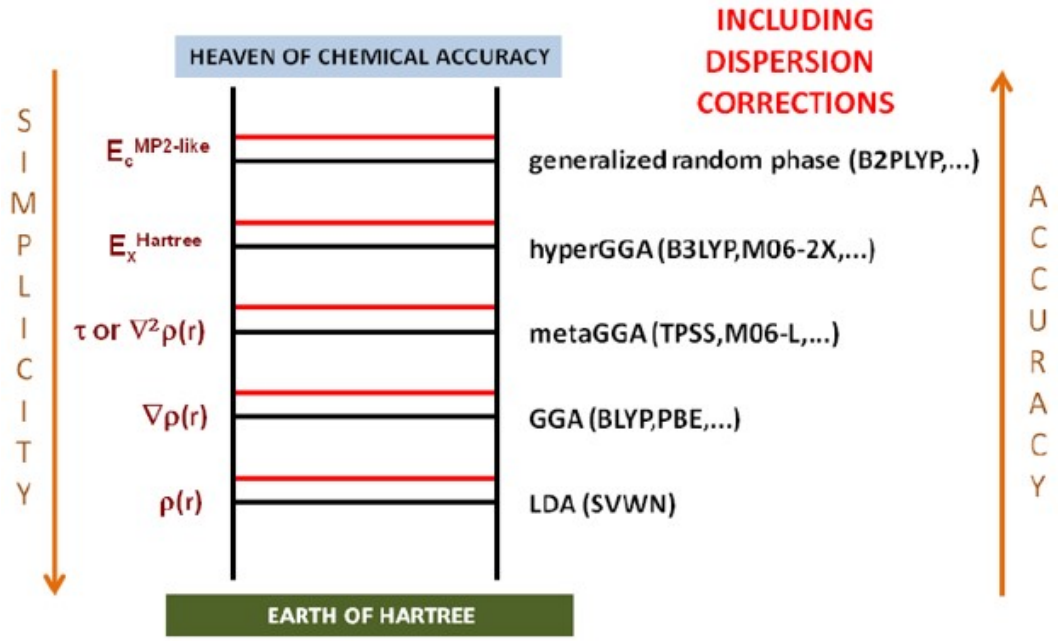

Figure 3.6: Jacob's Ladder via Perdew and Schmidt's metaphor.[3][13]

The general idea of Jacob's ladder is that things higher up the ladder are more effective so will converge faster, but each run will take longer. The discussion of convergence which follows in the next section should serve to clarify this idea.

The simulations performed in VASP that correspond to the rungs of this ladder include the DFT simulation using the generalized gradient approximation (GGA), the HSE06 simulation which is a hybrid-GGA, and the Hartree-Fock simulation which is not a DFT simulation at all.

3.4 Convergence

The goal of quantum simulations are $E - k$ plots and $I - V$ characteristics that match reality. To achieve this, the code must converge or focus onto a single value. The error is the difference between two iterations. Each iteration is composed of a guess, followed by a calculation of the error, followed by an iteration corrected using

[3]Reprinted from (John P. Perdew, Karla Schmidt, Jacob's ladder of density functional approximations for the exchange-correlation energy, AIP Conference Proceedings, 2001) with the permission of AIP Publishing.

the error, etc., until the error falls within the convergence criteria (in other words, until the error is small enough). At this point convergence is said to occur. The convergence limit is set either by the user or the simulation software; the smaller the error is required to be, the longer the simulation will take. It is possible that if the convergence criterion is too small, the simulation may time out and never finish running, so it is important to consider the limits of the simulation software and servers when setting this criterion. In both VASP 5.4 and NEMO the starting convergence criterion is a standard $1x10^{-5}$ (the units are determined by what the simulation is aimed at doing, but one example is eV).

In both VASP 5.4 and NEMO, the simulated devices are composed of matrix grids of points in the x, y, and z directions. These matrices of differential equations are simplified into difference equations and can then be broken down into for loops integrated over x, y, and z. The results of these simulations are likewise put into matrices of energy vs. momentum and current density vs. location to be read out by the user. Note that all simulation methods use matrices, and the more elements in a matrix, the longer it will take to solve. The grid breakdown must be done as simply as possible while also minimizing the error. An example of such a process is seen in NEMO's MetaPoissonQTBM5.py solver which has both fast and safe algorithms built into it for breaking down the device grids and performing the required calculations. The fast algorithm only checks against the most recent previously calculated term to determine the error, while the safe algorithm uses the Newton approach, which means it compares with both the most recent previously calculated term and the one before that and computes the average error. The determined error is then used to correct its next value and so on until convergence occurs. Thus, the safe algorithm, though requiring more computation per term in reality might converge faster because its error values are more significant.

NEMO uses the Jacobian iterative method as one of its solvers. A brief expla-

nation of this method is shown below to further understanding of convergence. This explanation and method are taken from *An Introduction to Numerical Linear Algebra* by Cullen [38].

3.4.1 Jacobian Iterative Method

Start with the linear system $A\ X = B$ where the diagonal entries of $A \neq 0$. The coefficient matrix A can then be broken up into three parts:

- A lower triangular matrix, L,
- An upper triangular matrix, R,
- And a nonsingular diagonal matrix, D.

Then,

$$A = D - L - R \tag{3.5}$$

and

$$(D - L - R)X = B, \tag{3.6}$$

$$DX = (L + R)X + B, \tag{3.7}$$

so that

$$X = D^{-1}(L + R)X + D^{-1}B. \tag{3.8}$$

To find X at convergence, the iteration is

$$X_k = D^{-1}(L + R)X_{k+1} + D^{-1}B. \tag{3.9}$$

An example of this method in use follows:

$$\begin{bmatrix} 4 & -1 & -1 & 0 \\ -1 & 4 & 0 & -1 \\ -1 & 0 & 4 & -1 \\ 0 & -1 & -1 & 4 \end{bmatrix} X = \begin{bmatrix} 9 \\ 12 \\ 0 \\ -3 \end{bmatrix}$$

where the true solution is known to be

$$X = \begin{bmatrix} 3.5 \\ 4 \\ 1 \\ 0.5 \end{bmatrix}.$$

Using the iterative method expressed above, the problem is solved for X.

$$A = \begin{bmatrix} 4 & -1 & -1 & 0 \\ -1 & 4 & 0 & -1 \\ -1 & 0 & 4 & -1 \\ 0 & -1 & -1 & 4 \end{bmatrix} = D - L - R$$

Therefore,

$$A = \begin{bmatrix} 4 & 0 & 0 & 0 \\ 0 & 4 & 0 & 0 \\ 0 & 0 & 4 & 0 \\ 0 & 0 & 0 & 4 \end{bmatrix} - \begin{bmatrix} 0 & 0 & 0 & 0 \\ 1 & 0 & 0 & 0 \\ 1 & 0 & 0 & 0 \\ 0 & 1 & 1 & 0 \end{bmatrix} - \begin{bmatrix} 0 & 1 & 1 & 0 \\ 0 & 0 & 0 & 1 \\ 0 & 0 & 0 & 1 \\ 0 & 0 & 0 & 0 \end{bmatrix}.$$

The Jacobian iteration matrix, J, is then defined as:

$$J = D^{-1}(L + R) = (1/4) \begin{bmatrix} 0 & 1 & 1 & 0 \\ 1 & 0 & 0 & 1 \\ 1 & 0 & 0 & 1 \\ 0 & 1 & 1 & 0 \end{bmatrix}.$$

and

$$X = JX + D^{-1}B = JX + (1/4)B. \tag{3.10}$$

Then,

$$X_{k+1} = JX_k + (1/4)B \tag{3.11}$$

where k is the iteration value, with $k = 0$ being the arbitrary first guess, say:

$$X_0 = \begin{bmatrix} 1 \\ 1 \\ 1 \\ 1 \end{bmatrix}.$$

Then

$$X_1 = JX_0 + (1/4)B = \begin{bmatrix} 2.75 \\ 3.50 \\ 0.50 \\ -0.25 \end{bmatrix},$$

$$X_2 = JX_1 + (1/4)B = \begin{bmatrix} 3.25 \\ 3.625 \\ 0.625 \\ 0.250 \end{bmatrix},$$

$$X_3 = \begin{bmatrix} 3.3125 \\ 3.8750 \\ 0.8750 \\ 0.3125 \end{bmatrix}, X_4 = \begin{bmatrix} 3.4375 \\ 3.9063 \\ 0.9063 \\ 0.4375 \end{bmatrix}, X_5 = \begin{bmatrix} 3.4531 \\ 3.9688 \\ 0.9688 \\ 0.4531 \end{bmatrix}, X_6 = \begin{bmatrix} 3.4844 \\ 3.9766 \\ 0.9766 \\ 0.4844 \end{bmatrix} ... \Rightarrow X = \begin{bmatrix} 3.5 \\ 4 \\ 1 \\ 0.5 \end{bmatrix}.$$

Clearly, as seen above, this method will yield a convergent series after enough iterations. If A was a full matrix each iteration would require approximately n^2 multiplications, so this method is more time-consuming than Gaussian elimination if more than $n/3$ iterations are required. Iterative methods are useful in solving systems where A is large, sparse, and regularly structured. [38]

Chapter 4

NEMO5 Simulation Results: An InGaAs Bowing parameter study

4.1 Introduction to Esaki diode data to be simulated

With the goal of benchmarking NEMO5 against previously fabricated homojunctions, multiple systems were considered from Pawlik's research [3]. These included InAs, GaAs, and $In_{0.53}Ga_{0.47}As$ Esaki diodes. Note that due to their small electron and hole effective masses, $p-i-n$ transistors made from InAs and GaAs materials are viable devices for generating large BTBT [15]. The initial designs introduced three regions: an intrinsic region sandwiched between a heavily-doped p-region and a heavily-doped n-region, with doping levels chosen to match the IEDM paper published by Pawlik and Rommel that were largely based on SIMS data [14].

The experimental data are seen in Fig. 4.1 - 4.6. The InGaAs devices are shown schematically in Fig. 4.1. Note that the 3 nm intrinsic region was included to ensure the $n+$ and $p+$ regions had minimal overlap due to diffusion or segregation during growth.

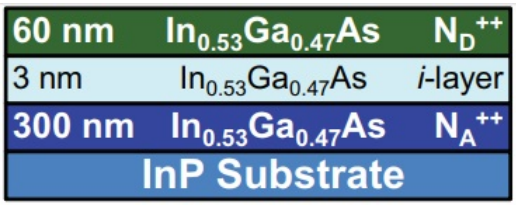

Figure 4.1: InGaAs device structure with doping. [14]

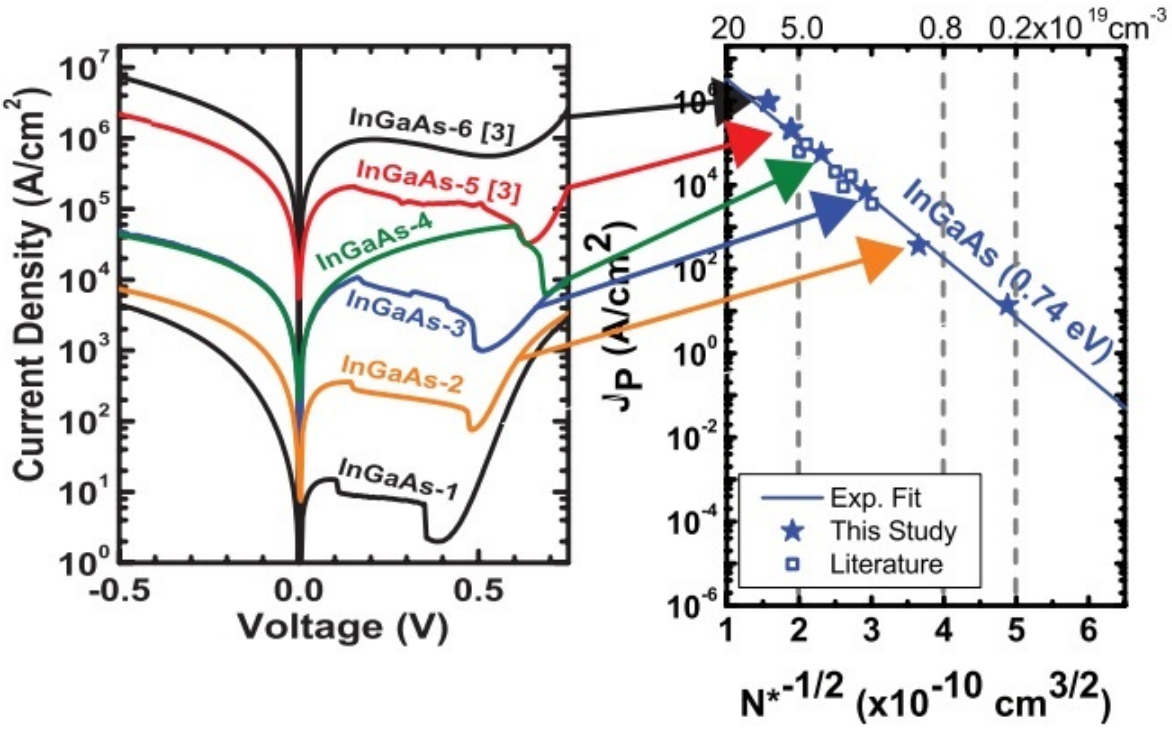

Figure 4.2: InGaAs devices experimental data. [14]

Fig. 4.3 illustrates the schematic diagram of the GaAs Esaki diodes. The accompanying experimental characteristics are shown in Fig. 4.4.

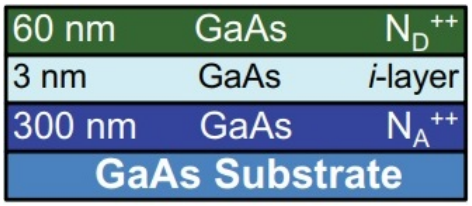

Figure 4.3: GaAs device structure with doping. [14]

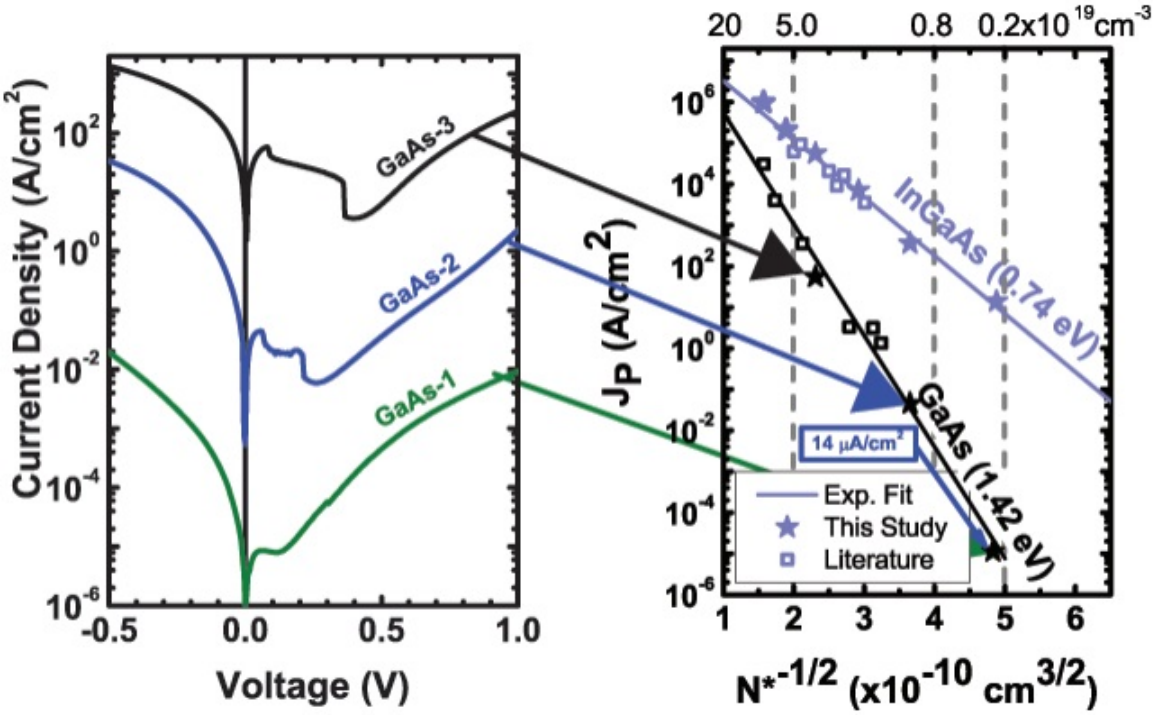

Figure 4.4: GaAs device structure with doping. [14]

Fig. 4.5 illustrates the schematic diagram of the InAs Esaki diodes. The accompanying experimental characteristics are shown in Fig. 4.6.

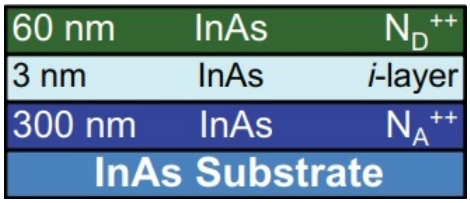

Figure 4.5: InAs device structure with doping. [14]

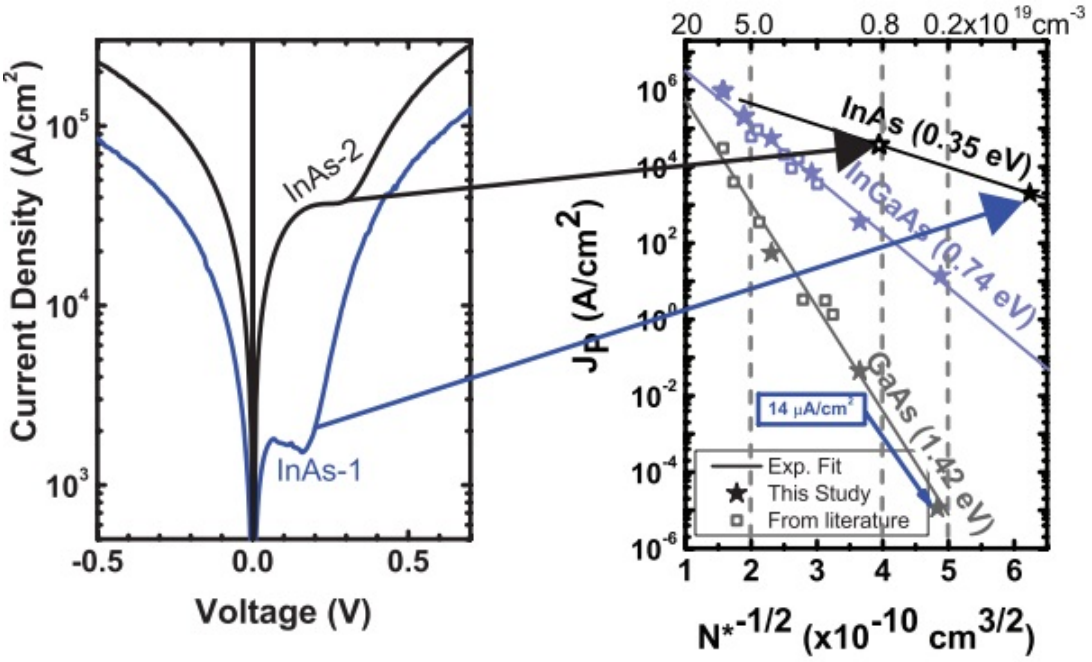

Figure 4.6: InAs device structure with doping. [14]

4.2 First NEMO5 Attempts at Benchmarking Homojunctions

The devices are designed as a "quasi-1D" structure in NEMO5 so as to cut down on simulation time. It is assumes that the structures are crystalline and repeat in the x- and y directions. These initial designs introduced three regions ($p+/intrinsic/n+$), though the the intrinsic region was treated as $p+$ in the case of the simulations. The doping levels were chosen to match the IEDM paper (see Fig. 4.1, 4.3, and 4.5) and were based on SIMS data. The homojunction device peak current densities were accurately predicted by David Pawlik via E.O. Kane's tunneling model. [3, 21]

Appendix C contains the NEMO5 structure files used to simulate the InGaAs-6 device. The NEMO5 simulation results are seen in Fig. 4.7 - 4.9 as well as the accompanying tables.

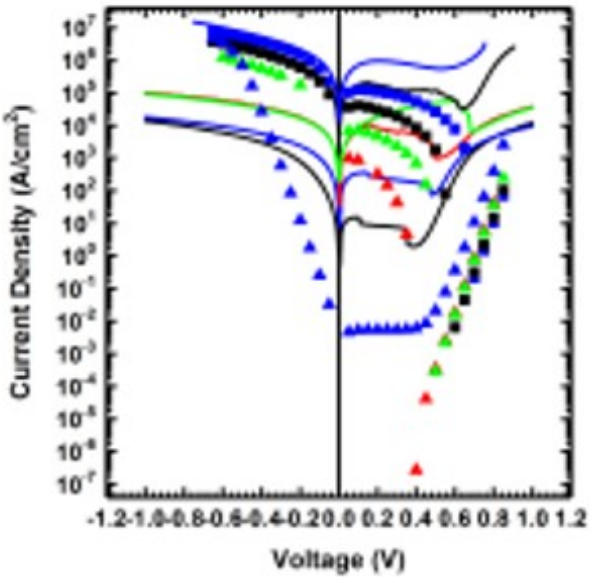

(a) Simulated vs. experimental transfer characteristics. Simulated data is the bulleted lines.

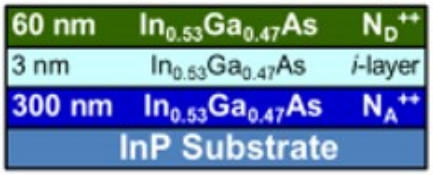

(b) Device structure.

Figure 4.7: NEMO5 simulations for the InGaAs-on-InP structure.[14]

An initial NEMO simulation was performed using NEMO's cirtual crystal approximation (VCA) method. VCA uses a straight Vegard's Law interpolation for all tight-binding parameters. Table 4.1 shows how severely the simulated current density is underestimated for the InGaAs devices. In the first two devices NDR is not even seen.

Table 4.1: Device doping and output current density peak summary for InP/InGaAs structure. [14]

Device	N_D x1E19 cm^{-3}	N_A x1E19 cm^{-3}	Exp. J_P $/cm^2$	NEMO J_P $/cm^2$
$InGaAs-1$	1.6	0.57	14 A	No NDR in NEMO
$InGaAs-2$	3	1	360 A	No NDR in NEMO
$InGaAs-3$	1.6	4.5	7 kA	0.997 kA
$InGaAs-4$	3	5	56 kA	7 kA
$InGaAs-5$	4.3	8	210 kA	41 kA
$InGaAs-6$	7	9.6	975 kA	125 kA

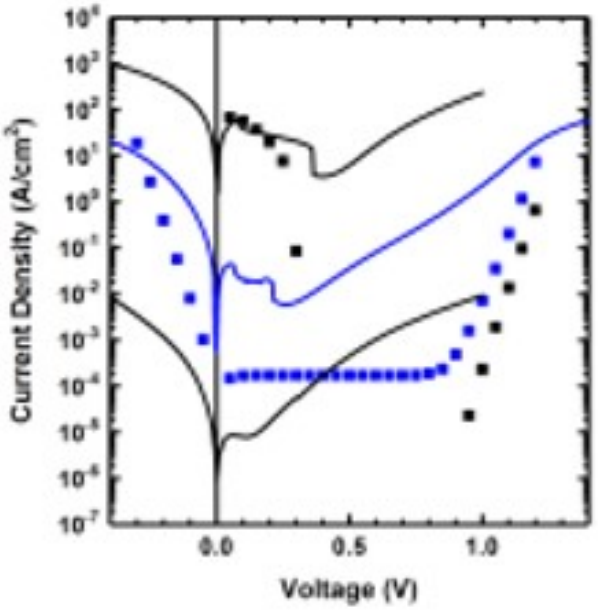

(a) Simulated vs. experimental transfer characteristics. Simulated data is the bulleted lines.

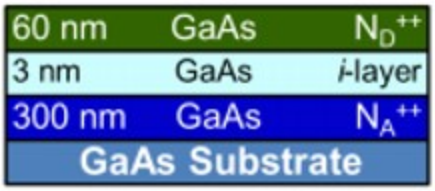

(b) Device structure.

Figure 4.8: NEMO5 simulations for the GaAs structure. [14]

As in the previous simulations, Table 4.2 shows how poorly the GaAs devices simulations fared when compared to the experimental data. NDR is again not even seen in the first two devices.

Table 4.2: Device doping and output current density peak summary for GaAs structure. [14]

Device	N_D x1E19 cm^{-3}	N_A x1E19 cm^{-3}	Exp. J_P $/cm^2$	NEMO J_P $/cm^2$
$GaAs-1$	3	0.5	11 μA	No NDR in NEMO
$GaAs-2$	3	1	45 mA	No NDR in NEMO
$GaAs-3$	3	5	55 A	68 A

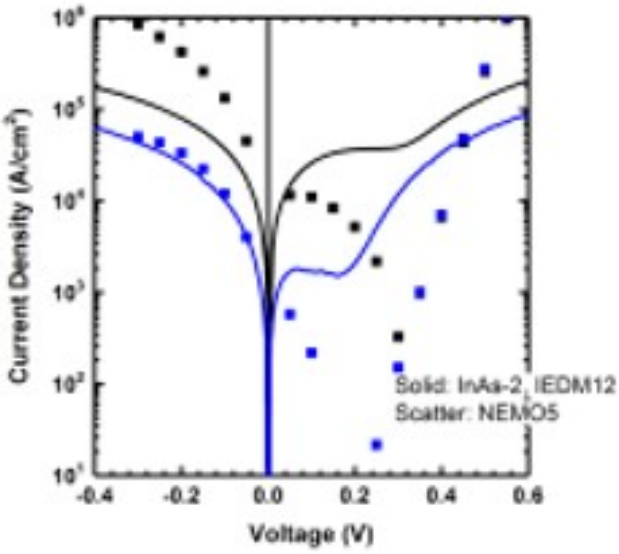

(a) Simulated vs. experimental transfer characteristics. Simulated data is the bulleted lines.

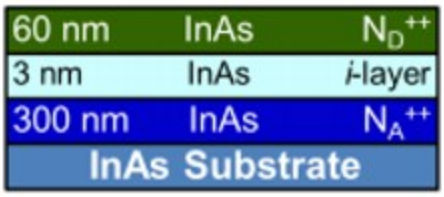

(b) Device structure.

Figure 4.9: NEMO5 simulations for the InAs structure. [14]

Table 4.3 shows that NEMO underestimated the current significantly. The predicted peak current is approximately 25% of the measured experimental peak current.

Table 4.3: Device doping and output current density peak summary for InAs structure. [14]

Device	N_D x1E19 cm^{-3}	N_A x1E19 cm^{-3}	Exp. J_P $/cm^2$	NEMO J_P $/cm^2$
$InAs-1$	0.3	1.8	2 kA	0.575 kA
$InAs-2$	1	1.8	37.6 kA	11.5 kA

The results shown above might seem encouraging at a glance because the I-V characteristics follow generally similar trends to reality, but the severe current density underestimation is a problem. The devices with low levels of degenerate doping showed no NDR, likely due to being too narrow and the simulated contacts not being wide enough to cover them.

To determine the cause of the current density overestimation in the NEMO5 simulations, band diagrams for the materials were simulated to see how they matched published material data. Two of these are shown in Fig. 4.10.

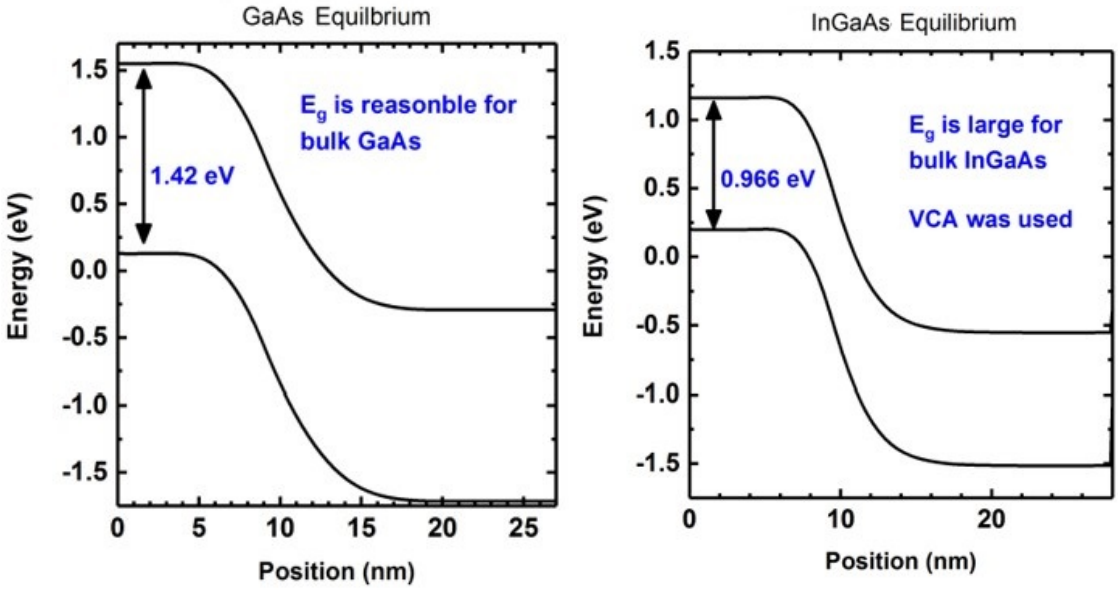

(a) NEMO5 GaAs $E - k$.

(b) NEMO5 InGaAs $E - k$.

Figure 4.10: NEMO5 simulations of E-k for GaAs and InGaAs.

The band gap for GaAs shown in Fig. 4.10a and for InAs (not shown) are reasonable calculations for bulk materials; these were performed using the VCA model in NEMO. The band gap for bulk $In_{0.53}Ga_{0.47}As$ (this concentration is fixed), on the other hand, is shown to be 0.966 eV which is higher than the 0.74 eV expected from literature. [16] It was hypothesized that if the band gap for $In_{0.53}Ga_{0.47}As$ could be brought closer to reality then the simulated current densities would be closer to reality.

A conference call with the NEMO5 team at Purdue University suggested a look at the material file and mentioned that the VCA model assumes an InGaAs concentration of $In_{0.53}Ga_{0.47}As$, might be the culprit.

4.3 Proposed Solution: Change the E_g Calculation

The VCA model in the *all.mat* material file was considered the crux for solving the problem of the incorrect InGaAs E_g value. The *all.mat* file contained the following

equation:

$$E_g{-}Gamma = 1.424{-}1.110{*}IN{+}0.45{*}IN^2{+}\frac{300 - Phys:Tkel}{300 - 77}{*}(0.040{*}IN{+}0.086{*}GA) \tag{4.1}$$

where IN is the indium concentration and GA is the gallium concentration.

According to Bhattacharya, Eq. 4.1 assumes a strained GaAs substrate with a low indium concentration. This is known to not be the case, as seen from Fig. 4.7b which shows that the devices being simulated were grown on InP. Bhattacharya provides a different model to use that assumes a InP unstrained substrate for an $In_{0.53}Ga_{0.47}As$ material. [39] This is Eq. 4.2 which follows:

$$E_g = 0.75 - 1.05 * IN + 0.45 * IN^2 \tag{4.2}$$

Another similar model was found on the Ioffe website and follows as Eq. 4.3 [16]

$$E_g = 0.36 + 0.63 * IN + 0.43 * IN^2 \tag{4.3}$$

The *all.mat* file was edited first with Eq. 4.2 and then Eq. 4.3 with no visible changes in the results seen in the simulated band gaps with either of the changes. On a whim, the $E_g - Gamma$ variable was changed to a ridiculous number that had no basis in reality, to see if this would have any effect and, again, no effect was observed. Thus, this attempt was determined to have been futile and a new approach was considered.

4.4 Proposed Solution: Consider the NEMO5 Tight-binding Parameters

VCA assumes that the parameters vary linearly with the composition. That is, VCA can be considered as a weighted average between the relevant (in this case, InAs and GaAs) molecules. Luisier *et al.* shows the necessity of using a correction factor referred to as a **bowing parameter**. The bowing parameter refers to the empirical offset determined from the linear interpolation used in the VCA. It is called a bowing factor because the parameters seem to *bow* with the composition, as seen in Fig. 4.11, depending on what it is. Fig. 4.11 shows Luisier *et al.*'s fix with the applied bowing parameters.

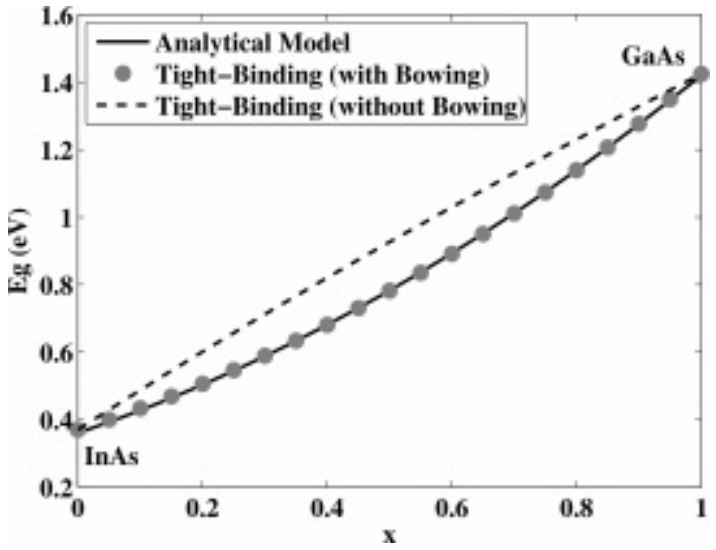

Figure 4.11: Electron band gap of $In_x\ Ga_{1-x}As$ at room temperature as a function of the In concentration x. Note that the paper had it wrong; the bottom axis should be the Ga concentration. This was corrected in this thesis. The solid line corresponds to the Ioffe data, the dotted line is the data with added bowing effects, and the dashed line is the data with no bowing effects. IEEE © 2009.[1][15, 16]

The parameters found in Luisier *et al.* and Boykin *et al.* were applied to the

[1]Reprinted from (M. Luisier and G. Klimeck, Investigation of $in_xga_{1-x}as$ ultra-thin-body tunneling fets using a full-band and atomistic approach, 2009 International Conference on Simulation of Semiconductor Processes and Devices) with the permission of IEEE © 2009.

all.mat file tight-binding parameters using the parameterization equation which follows:

$$P_{InxGa(1-x)As} = x * P_{InAs} + (1-x) * P_{GaAs} + x(1-x) * B_{InAs\_GaAs} \tag{4.4}$$

where $P\_$ is the relevant parameter, x is the indium concentration, and $B\_$ is the bowing parameter used.

A new InGaAs material file was created with the applied bowing parameters. This comprises the next section.

Luisier *et al.* also notes that in their NEMO simulations the band gap and effective masses of InAs and GaAs could not be reproduced without spin-orbit coupling being included in the calculations. If this effect was not included the band gap and effective mass were both predicted larger than reality which caused an underestimation of BTBT. The spin-orbit parameters were kept as they were previously and not edited with an added bowing effect in the simulations which follow. Based on the results which follow, this is assumed to have been a reasonable assumption. [15]

4.5 The Rosetta Stone of NEMO5 Tight-binding Parameters for InGaAs

The results of this examination of the application of the bowing parameter are listed in the tables which follow. The anion is defined as arsenic in both GaAs and InAs. Thus, because there is no change in the anion composition between the two when combined to create InGaAs, the bowing parameter for all of the energies in this first table, Table 4.4, is 0. E_{sa} refers to the energy of the anion's s-orbital, E_{pa} to the energy of the anion's p-orbital, etc. Recall from the discussion of orbitals that the s^*-orbital is an s-like orbital often used to increase simulation accuracy.

Table 4.4: Bowing effects for the anion (As) band energies.

	GaAs all.mat		InAs all.mat			InGaAs all.mat	
Parameters	**Name**	**Value**	**Name**	**Value**	**Bowing**	**Name**	**Value**
E_{sa}	E_s_As	-5.5004	E_s_As	-5.5004	0	E_s_As	-5.5004
E_{pa}	E_Px_As	4.151	E_Px_As	4.1511		E_Px_As	4.1511
	E_Py_As		E_Py_As			E_Py_As	
	E_Pz_As		E_Pz_As			E_Pz_As	
E_{da}	E_Dxy_As	4.151	E_Dxy_As	4.1511		E_Dxy_As	4.1511
	E_Dyz_As		E_Dyz_As			E_Dyz_As	
	E_Dz2_As		E_Dz2_As			E_Dz2_As	
	E_Dxz_As		E_Dxz_As			E_Dxz_As	
	E_Dx2 y2_As		E_Dx2 y2_As			E_Dx2 y2_As	
E_{s*a}	E_Star_As	19.7106	E_Star_As	19.7106		E_Star_As	19.7106

The cation is different for the two materials (either indium or gallium), so all these following tables show the bowing parameter changes to note.

Table 4.5: Bowing effects for the cation (In or Ga) band energies.

	GaAs all.mat		InAs all.mat			InGaAs all.mat	
Parameters	**Name**	**Value**	**Name**	**Value**	**Bowing**	**Name**	**Value**
E_{sc}	E_s_Ga	-0.2412	E_s_In	-0.5819	-0.204	E_s_Galn	-0.4726
E_{pc}	E_Px_Ga	6.7078	E_Px_In	6.9716	0.2621	E_Px_Galn	6.9129
	E_Py_Ga		E_Py_In			E_Py_Galn	
	E_Pz_Ga		E_Pz_In			E_Pz_Galn	
E_{dc}	E_Dxy_Ga	12.7485	E_Dxy_In	13.3071	0.3427	E_Dxy_Galn	13.1299
	E_Dyz_Ga		E_Dyz_In			E_Dyz_Galn	
	E_Dz2_Ga		E_S1dz2_In			E_Dz2_Galn	
	E_Dxz_Ga		E_Dxz_In			E_Dxz_Galn	
	E_Dx2 ~y2_Ga		E_Dx2 ~y2_In			E_Dx2 ~y2_Galn	
E_{s*c}	E_Sstar_Ga	22.6635	E_Sstar_In	19.9414	-1.4772	E_Sstar_Galn	20.8528

Table 4.6 shows parameters applied to the $s - to - s$ orbital interactions. Recall that the s-orbital only forms sigma bonds.

Table 4.6: Bowing effects for the $s-to-s$-orbital interactions.

	GaAs all.mat		InAs all.mat			InGaAs all.mat	
Param	**Name**	**Value**	**Name**	**Value**	**Bowing**	**Name**	**Value**
$ss\sigma$	V_S_S_Sigma_As_Ga	-1.6451	V_S_S_Sigma_As_In	-1.6944	-0.0262	V_S_S_Sigma_As_Galn	-1.6777
	V_S_S_Sigma_Ga_As		V_S_S_Sigma_In_As			V_S_S_Sigma_Galn_As	
$s^*s^*\sigma$	V_S*_S_Sigma_As_Ga	-3.6772	V_S*_S_Sigma_As_In	-4.2105	-0.2850	V_S*_S_Sigma_As_Galn	-40308
	V_S*_S_Sigma_Ga_As		V_S*_S_Sigma_In_As			V_S*_S_Sigma_Galn_As	
$s_as_c^*\sigma$	V_S*_S_Sigma_As_Ga	-2.2078	V_S*_S_Sigma_As_In	-2.2467	-0.0545	V_S*_S_Sigma_As_Galn	-2.3374
	V_S*_S_Sigma_Ga_As		V_S*_S_Sigma_In_As			V_S*_S_Sigma_Galn_As	
$s_as_c^*\sigma$	V_S*_S_Sigma_As_Ga	-1.13149	V_S*_S_Sigma_As_In	-1.1599	-0.1022	V_S*_S_Sigma_As_Galn	-1.2582
	V_S*_S_Sigma_Ga_As		V_S*_S_Sigma_In_As			V_S*_S_Sigma_Galn_As	

Table 4.7 shows parameters applied to the $s-to-p$ and $s-to-d$ orbital interactions. Again, the s-orbital can only form sigma bonds. Also note that $s-to-d$ and $p-to-d$ are the same.

Table 4.7: Bowing effects for the $s-to-p$ and $s-to-d$ orbital interactions.

	GaAs all.mat		InAs all.mat			InGaAs all.mat	
Param	**Name**	**Value**	**Name**	**Value**	**Bowing**	**Name**	**Value**
$s_ap_c\sigma$	V_S_P_Sigma_As_Ga	2.6649	V_S_P_Sigma_As_In	2.5982	-0.0667	V_S_P_Sigma_As_Galn	2.6130
$s_cp_a\sigma$	V_S*_P_Sigma_Ga_AS	2.9603	V_S*_P_Sigma_In_As	2.8094	0.1488	V_S*_P_Sigma_Galn_As	2.8432
$s*_ap_c\sigma$	V_S*_P_Sigma_As_Ga	1.9765	V_S*_P_Sigma_As_In	2.8094	-0.1488	V_S*_P_Sigma_As_Galn	2.0475
$s*_cp_a\sigma$	V_S*_P_Sigma_Ga_As	1.0276	V_S*_P_Sigma_In_As	0.9373	-0.0902	V_S*_P_Sigma_Galn_As	0.9573
$S_ad_c\sigma$	V_S_D_Sigma_As_Ga	-2.5836	V_S_D_Sigma_As_In	-2.2684	0.3152	V_S_D_Sigma_As_Galn	-2.3380
$S_cd_a\sigma$	V_S_D_Sigma_Ga_As	-2.2306	V_S_D_Sigma_In_As	-2.2931	-0.0131	V_S_D_Sigma_Galn_As	-2.3093
$s*_ad_c\sigma$	V_S*_D_Sigma_As_Ga	-0.6282	V_S*_D_Sigma_As_In	-0.8994	0.2711	V_S*_D_Sigma_As_Galn	-0.8395
$s*_cd_a\sigma$	V_S*_D_Sigma_Ga_As	-0.1332	V_S*_D_Sigma_In_As	-0.48899	-0.3556	V_S*_D_Sigma_Galn_As	-0.2332

Table 4.8 shows parameters applied to the $p-to-p$ and $p-to-d$ orbital interactions. The $s-to-p$ orbital interactions were shown in the previous tables. The p-orbital forms both sigma and pi bonds so both of these are listed.

Table 4.8: Bowing effects for the $p - to - p$ and $p - to - d$ orbital interactions.

	GaAs all.mat		InAs all.mat			InGaAs all.mat	
Param	**Name**	**Value**	**Name**	**Value**	**Bowing**	**Name**	**Value**
ppσ	V_P_P_Sigma_As_Ga	4.1508	V_P_P_Sigma_As_In	4.3106	-0.1355	V_P_P_Sigma_As_Galn	4.2018
	V_P_P_Sigma_Ga_As		V_P_P_Sigma_In_As			V_P_P_Sigma_Galn_As	
ppπ	V_P_P_Pi_As_Ga	-1.14274	V_P_P_Pi_As_In	-1.2890	0.1185	V_P_P_Pi_As_Galn	-1.3245
	V_P_D_Pi_Ga_As		V_P_D_Pi_In_As			V_P_D_Pi_Galn_As	
$p_a d_c \sigma$	V_P_D_Sigma_As_Ga	-1.8743	V_P_D_Sigma_As_In	-1.7314	0.1210	V_P_D_Sigma_As_Galn	-1.7684
$p_c d_a \sigma$	V_P_D_Pi_As_Ga	-1.8896	V_P_D_Pi_As_In	-1.9784	0.0876	V_P_D_Sigma_As_Galn	-1.9149
$p_a d_c \pi$	V_P_P_Pi_As_Ga	2.5293	V_P_P_Pi_As_In	2.1889	-0.0979	V_P_P_Pi_As_Galn	2.3245
$p_c d_a \pi$	V_P_P_Pi_As_Ga	2.5491	V_P_P_Pi_As_In	2.4560	-0.0931	V_P_P_Pi_As_Galn	2.4766

The final bowing interactions in Table 4.9 shows parameters applied to the $d - to - d$ orbital interactions. The $s - to - d$ and $p - to - d$ orbital interactions were shown in the previous tables. The d-orbital forms sigma, pi, and delta bonds so all of these are listed.

Table 4.9: Bowing effects for the $d - to - d$ orbital interactions.

	GaAs all.mat		InAs all.mat			InGaAs all.mat	
Param	**Name**	**Value**	**Name**	**Value**	**Bowing**	**Name**	**Value**
ddσ	V_D_D_Sigma_As_Ga	-1.2700	V_D_D_Sigma_As_In	-1.5846	0.0327	V_D_D_Sigma_As_Galn	-1.4286
	V_D_D_Sigma_Ga_As		V_D_D_Sigma_In_As			V_D_D_Sigma_Galn_As	
ddπ	V_D_D_Pi_As_Ga	2.5054	V_D_D_Pi_As_In	2.71799	0.2117	V_D_D_Sigma_As_Galn	2.6708
	V_D_D_Pi_Ga_As		V_D_D_Pi_In_As			V_D_D_Sigma_Galn_As	
ddδ	V_D_D_Sigma_As_Ga	-0.8517	V_D_D_Sigma_As_In	-0.5051	0.3464	V_D_D_Sigma_As_Galn	-0.5817
	V_D_D_Sigma_Ga_As		V_D_D_Sigma_In_As			V_D_D_Sigma_Galn_As	

4.6 Bowing results

New *all.mat* files were generated for varying compositions of In and GaAs, from 5% to 95% in steps of 5% of each and these were used to simulate new $E - k$ plots. A few of these are included in Figs. 4.12 - 4.15. Note from Fig. 4.12 that the band-diagram generated from the *all.mat* file with the added bowing parameter effects

shows a notably smaller band gap. Recall that this was the goal, as the InGaAs band gap from the first simulations was too large to be real.

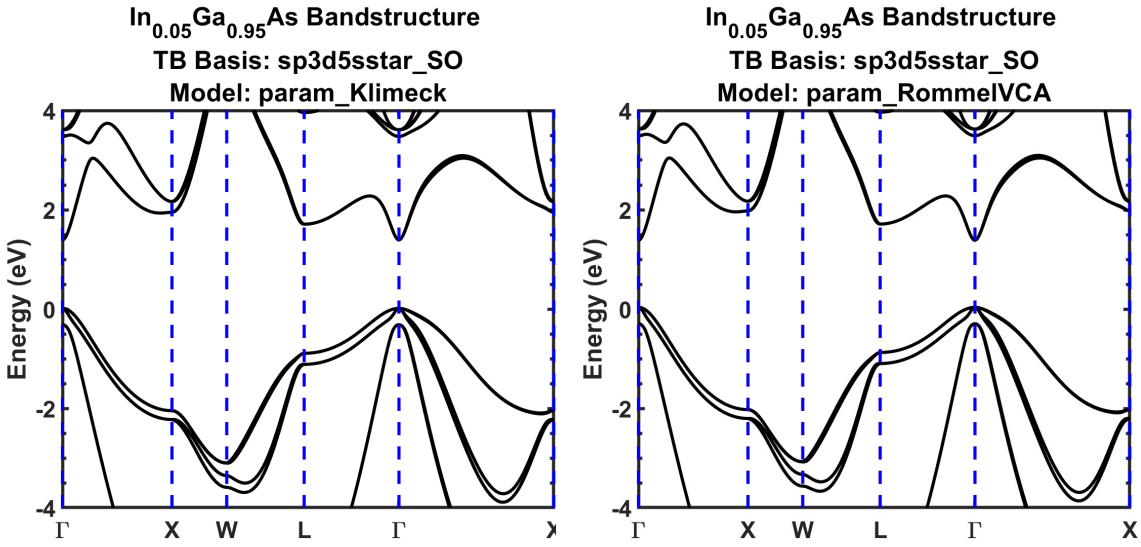

(a) Simulation using only the VCA model. E_g= 1.3764 eV.

(b) Simulation with bowing effects included. E_g= 1.3491 eV.

Figure 4.12: NEMO5 bandstructure results for In=0.05 GaAs=0.95 composition with and without bowing effects included.

Fig. 4.13 has compositions similar to the standard indium 53% concentration and shows a band gap a lot closer to the 0.74 eV expected when the bowing effects are included in the simulation.

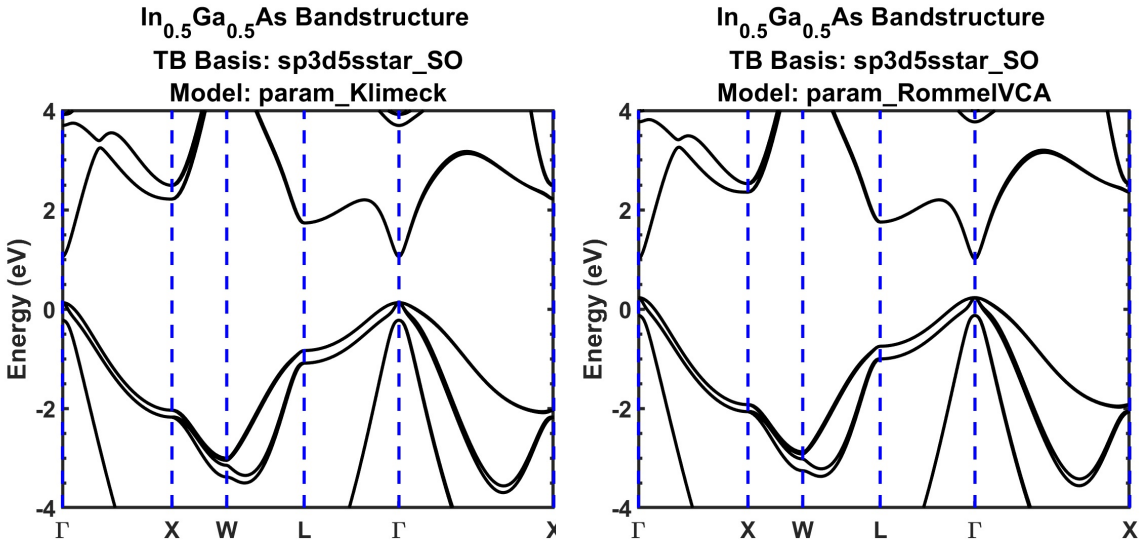

(a) Simulation using only the VCA model. E_g= 0.9260 eV.

(b) Simulation with bowing effects included. E_g= 0.7816 eV.

Figure 4.13: NEMO5 bandstructure results for In=0.50 GaAs=0.50 composition with and without bowing effects included.

Fig. 4.14 corresponds to the indium 53%, gallium 47% concentration and shows a band gap even closer to the 0.74 eV expected with the bowing effects included in the simulation as the band gap is measured to be E_g= 0.7662 eV in this case.

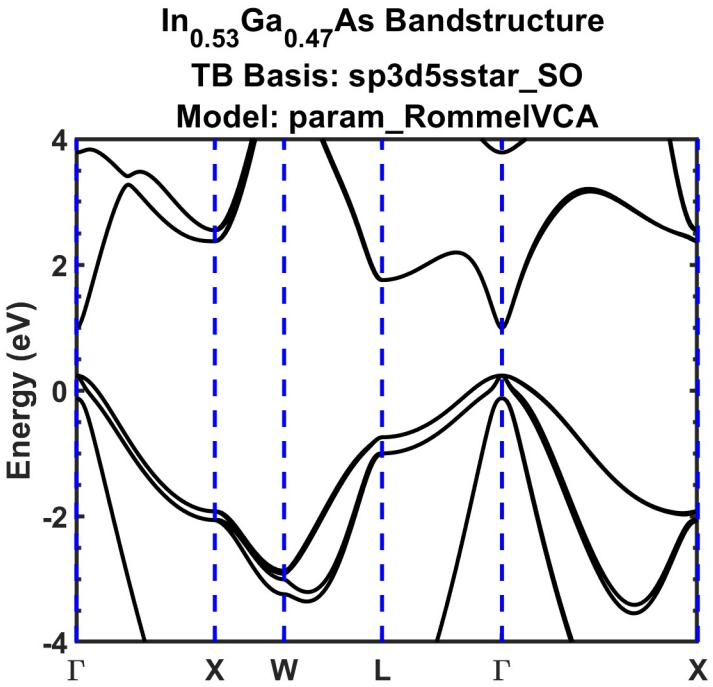

Figure 4.14: NEMO5 bandstructure results for In=0.53 GaAs=0.47 composition with bowing effects included. E_g= 0.7662 eV.

Fig. 4.15 shows the same trends as the previous two figures.

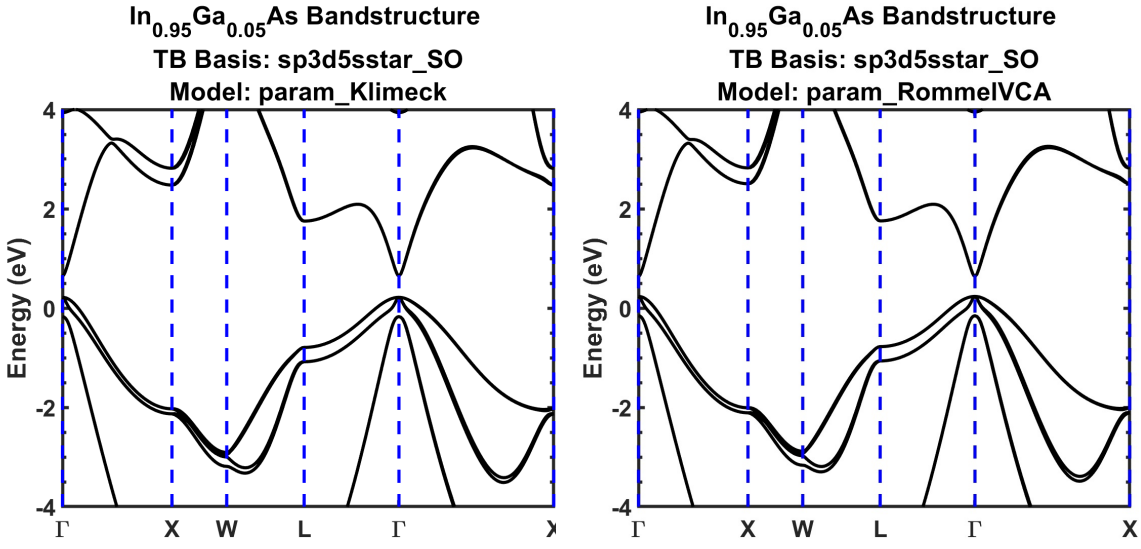

(a) Simulation using only the VCA model. E_g= 0.4290 eV.

(b) Simulation with bowing effects included. E_g= 0.4002 eV.

Figure 4.15: NEMO5 bandstructure results for In=0.95 GaAs=0.05 composition with and without bowing effects included.

Next, the composition was plotted against the band gap for a plot similar to the one made by Luisier *et al.* (Fig. 4.11). Note that Luisier *et al.* actually plotted the x-axis incorrectly.

As seen from Fig. 4.16, band gap increases with decreased indium concentration. There is a slight bow to this data as a result of the bowing parameter application, and it matches up almost perfectly with data from both Luisier *et al.* and Ioffe. [15, 16]

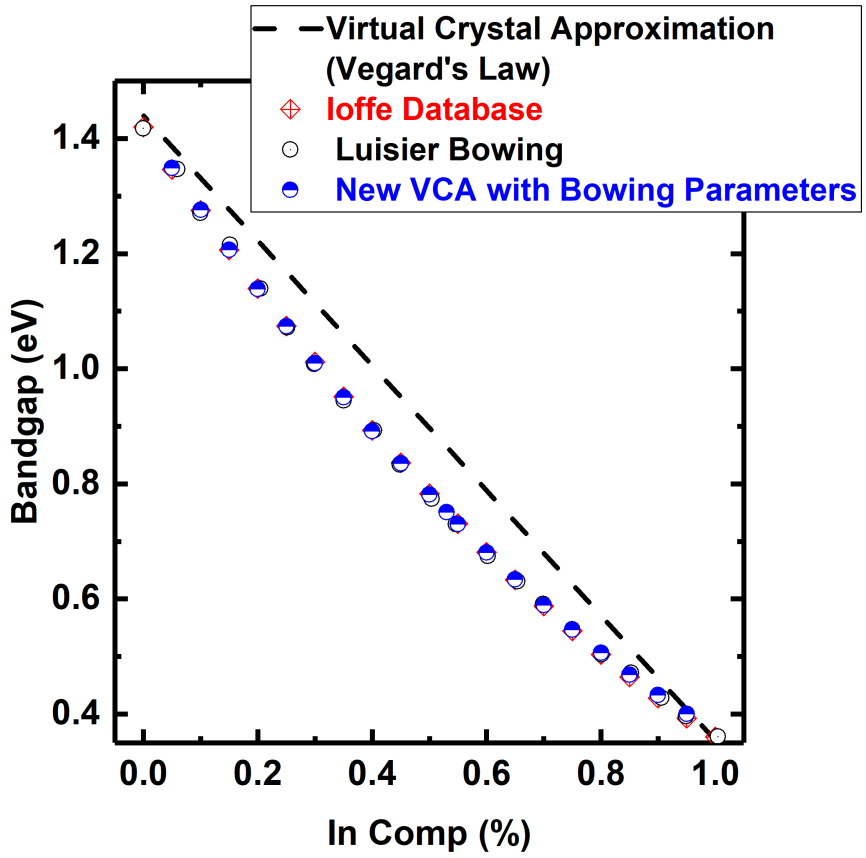

Figure 4.16: Electron band gap of $In_x\ Ga_{1-x}As$ at room temperature as a function of the In concentration x as plotted after applying the bowing effects and comparing to the Ioffe and Luisier data. [15, 16]

4.7 Second NEMO5 Attempts at Benchmarking Homojunctions

The next step after creating this new *all.mat* file with the edited tight-binding parameters was to run the simulations again. The InGaAs results are included in Fig. 4.18. The new simulated data is seen to be an extremely close fit to the experimental data which makes this exercise a success. Note that the device labeled "low-doped, too thin" had contact regions of 16 unit cells which was determined to be not wide enough for the simulation to produce NDR. The contact regions were extended to 20 unit cells; subsequently NDR with a peak current density comparable with the experiment was observed.

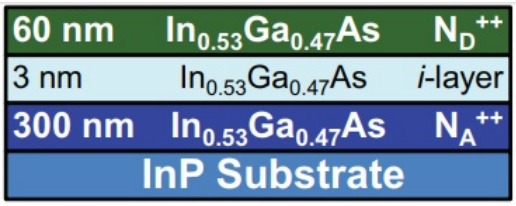

Figure 4.17: InGaAs device structure with doping. [14]

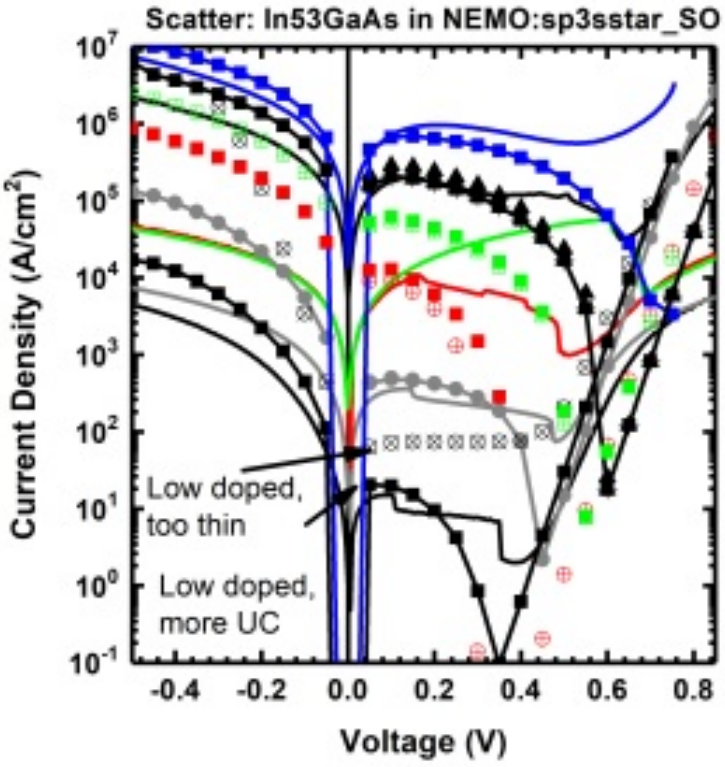

Figure 4.18: InGaAs devices simulated with the new all.mat file and plotted against real data from Pawlik *et al.*. [14]

Table 4.10 shows the new simulated data for the InGaAs structures. As stated above and now seen in this table, an extremely tight fit to the tunneling current is seen for the simulations, especially for the highly-doped devices. This validates the revised NEMO models wholly.

Table 4.10: Device doping and output current density peak summary for InGaAs structure as simulated with the new all.mat file. [14]

Device	N_D x1E19 cm^{-3}	N_A x1E19 cm^{-3}	Exp. J_P $/cm^2$	NEMO J_P $/cm^2$
$InGaAs-1$	1.6	0.57	14 A	20.4 kA
$InGaAs-2$	3	1	360 A	483
$InGaAs-3$	1.6	4.5	7 kA	8.8 kA
$InGaAs-4$	3	5	56 kA	61.3 kA
$InGaAs-5$	4.3	8	210 kA	207 kA
$InGaAs-6$	7	9.6	975 kA	686 kA

Following this data match, a second experiment was run to simulate an exper-

imental device that had initially been meant to be an InGaAs TFET (N_D x1E19 cm^{-3}, N_A x1E19 cm^{-3}) with a 100 nm intrinsic region. Due to miscommunication with the grower, the intrinsic region was instead grown to 10 nm, so when the device was tested it showed NDR. A NEMO5 simulation was performed varying the intrinsic region thicknesses. The simulated results are plotted along with the experimental results in Fig.4.20. Not surprisingly the 10 nm intrinsic region is the tightest match.

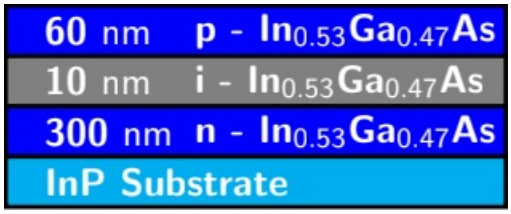

Figure 4.19: InGaAs device structure with doping. [14]

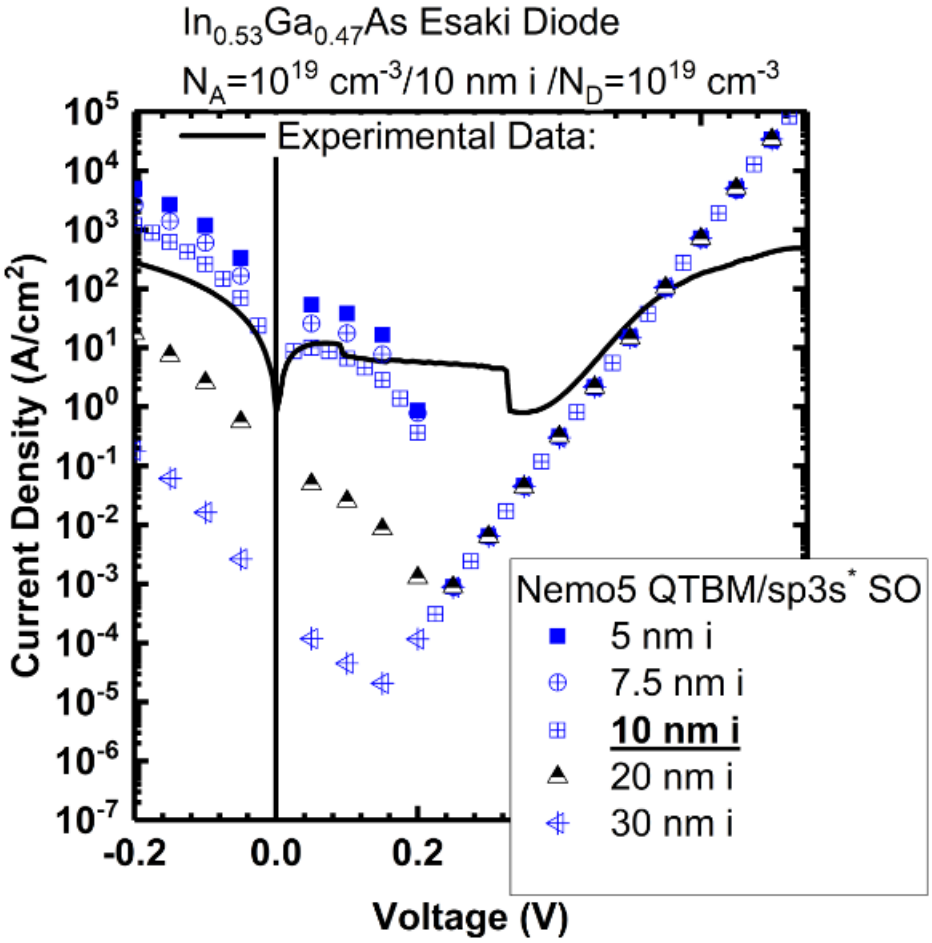

Figure 4.20: InGaAs devices with varying intrinsic (referred to as "i") region thicknesses plotted against experimental data from Pawlik *et al.*. [14]

Chapter 5

VASP Benchmarking Results

A number of VASP tests were run with the primary goal of determining the software's limitations. Note that Appendix B shows the methodology for performing a simple VASP run using MedeA.

5.1 Lattice Constant Variations

One of the first experiments run in VASP 5.4 was to vary the lattice constant input for GaAs and InAs and observe the results in terms of the band diagrams. Note that all VASP simulations were performed in the Materials Design MedeA environment.

A screening DFT simulation was performed. The k-point spacing was 0.5/Å in a Γ-centered Monkhorst-Pack mesh. This resulted in a 4x4x4 grid. The planewave cutoff was 280 eV and a GGA-PBE exchange correlation was used. Fig. 5.1 shows the results for the GaAs simulations. The primary take-away is that the band gap grows larger as the lattice constant is increased. Fig. 5.1(a) is no longer a semiconductor and Fig. 5.1(c) shows an indirect band gap not consonant with GaAs as it is generally known.

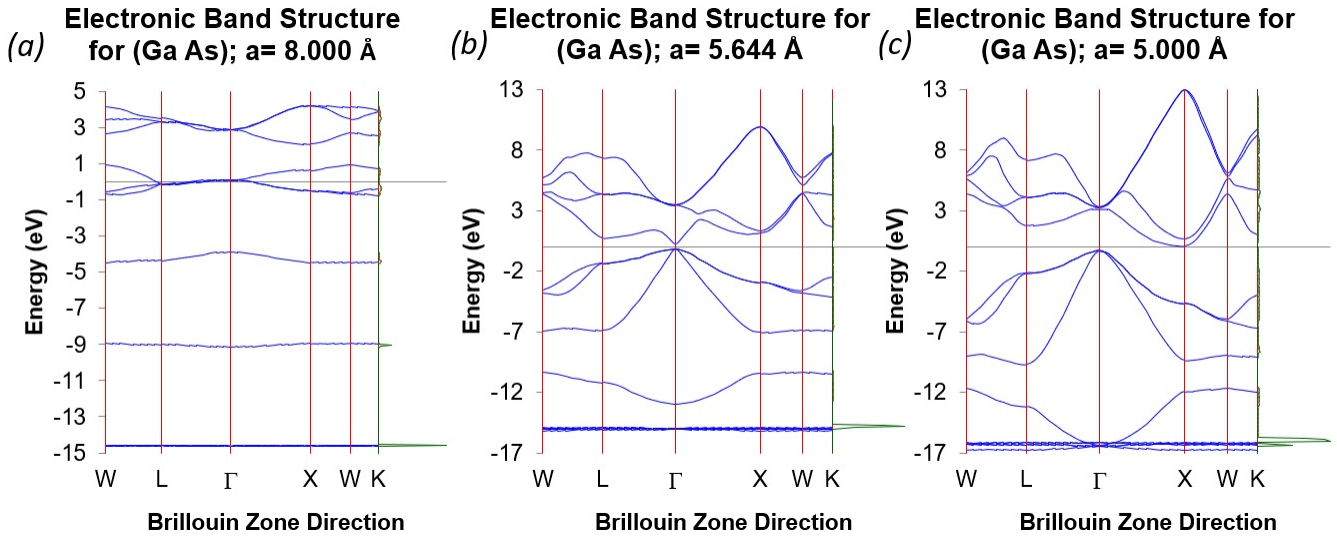

Figure 5.1: VASP simulations of GaAs lattice constant variation screen.

This same experiment was conducted using InAs as the material and parallel observations can be made about the effects of increasing the lattice constant on the band gap from Fig. 5.2.

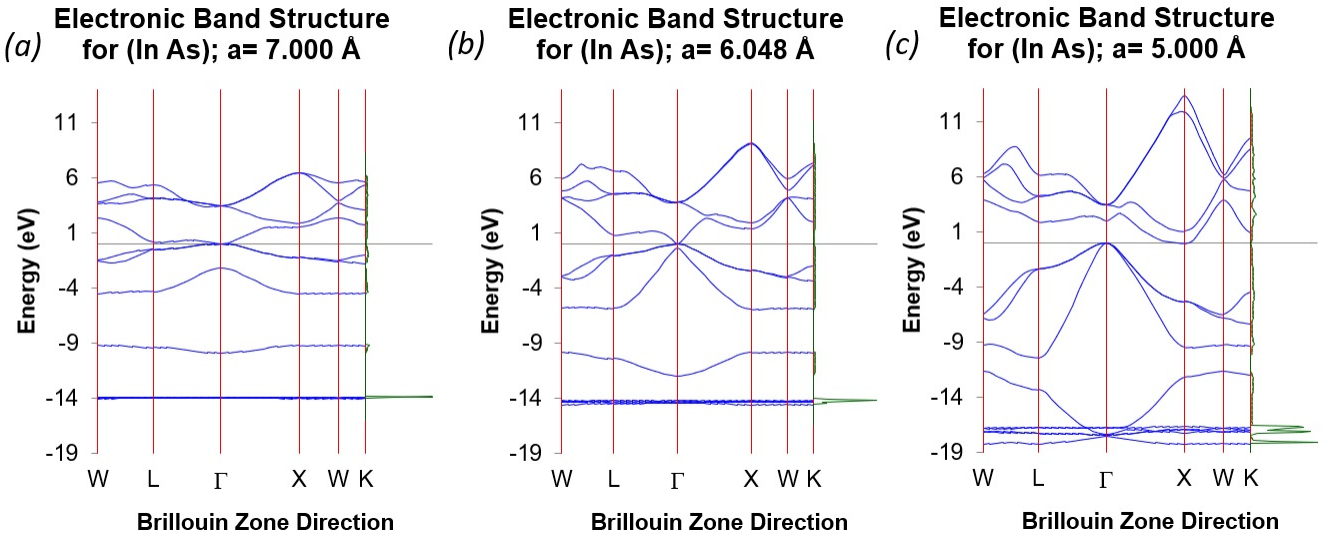

Figure 5.2: VASP simulations of InAs lattice constant variation screen.

5.2 The Effects of Varying the Functional: Part 1

The simulation functionals refers to the simulation calculation methods used. Simulations were performed for GaAs and InAs using different functionals to determine

which corresponded the closest to reality. The functionals of interest were: DFT with GGA-PBE, HSE06 with GGA-PBE, and Hartree-Fock.

Recall that Luisier *et al.* mentioned that in their NEMO simulations the band gap and effective masses of InAs and GaAs could not be reproduced without spin-orbit coupling being included in the calculations. If this effect was not included the band gap and effective mass were both predicted larger than reality. For this reason, spin-orbit was turned on for the following simulations to increase accuracy, though the trade-off is an increase in computation time. The settings described in Section 5.1 for k-point spacing and planewave cutoff were used again. The change was the functional, which is accordingly noted.

5.2.1 GaAs VASP Simulation Results

Note that the expected band gap, E_g, for GaAs is approximately 1.424 eV at 300 K. Fig. 5.3 - 5.5 are all DFT simulations. Fig. 5.3 is the simple DFT with GGA-PBE and added spin orbit and predicts a band gap of 0.3804 eV. Fig. 5.4 is the DFT calculated during the HSE06 simulation and predicts a band gap of 0.5467 eV. Fig. 5.5 is the DFT calculated during the Hartree-Fock simulation and predicts a band gap of 0.1531 eV. They all significantly underestimate the band gap. These simulations were extremely quick to compute, taking approximately one minute each, but are not accurate enough to be useful.

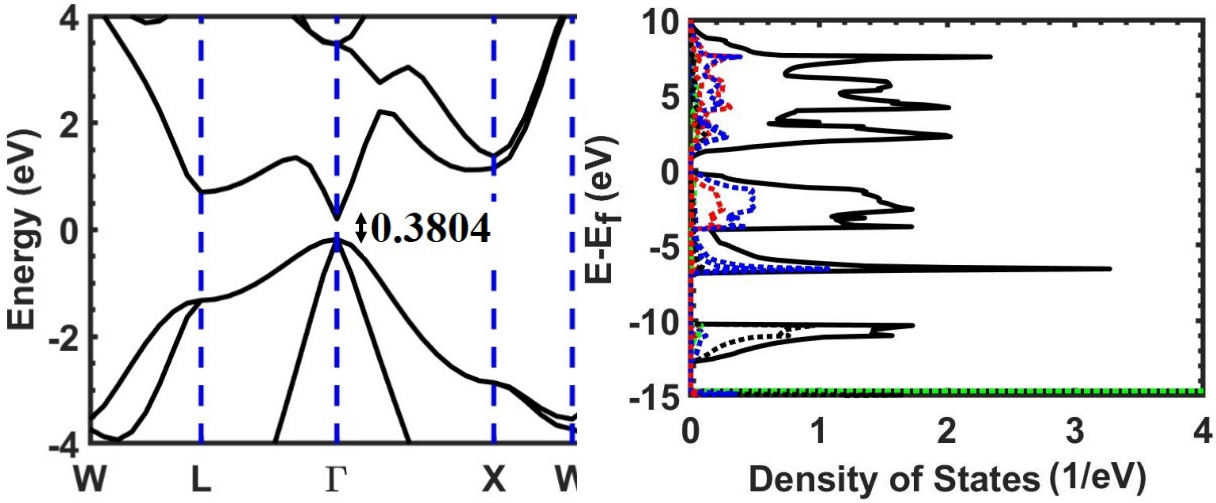

(a) Energy band diagram. **(b)** Density of States.

Figure 5.3: VASP simulation of GaAs using DFT with GGA-PBE with spin-orbit.

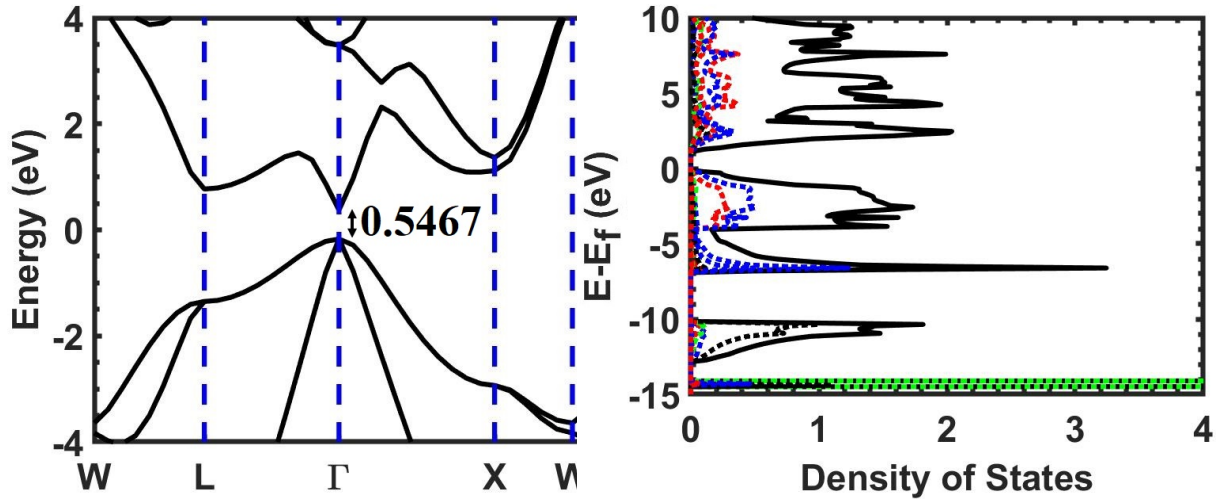

(a) Energy band diagram. **(b)** Density of States.

Figure 5.4: VASP simulation of GaAs DFT as an artifact of the HSE06 simulation. Again with spin-orbit included.

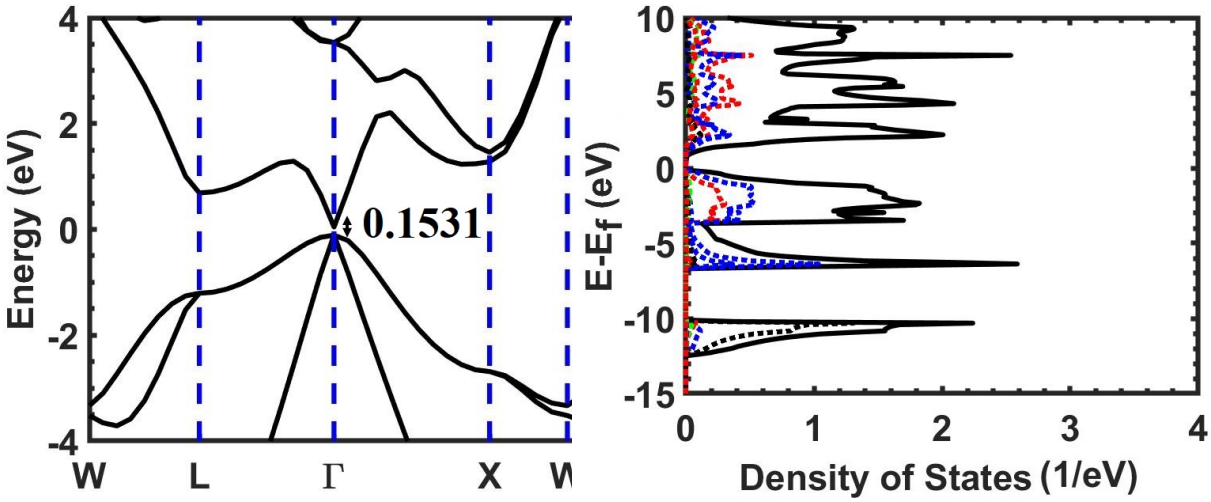

(a) Energy band diagram. **(b)** Density of States.

Figure 5.5: VASP simulation of GaAs DFT as an artifact of the Hartree-Fock simulation. Again with spin-orbit included.

Next, Fig. 5.6 represents the GaAs $E - k$ as simulated using the HSE06 meta-GGA method with spin orbit coupling turned on. The band gap predicted with this method is 1.5029 eV which is very close to the 1.424 eV expected. This simulation took approximately two days to complete on a two-core four-thread machine, so it is significantly more cumbersome computationally.

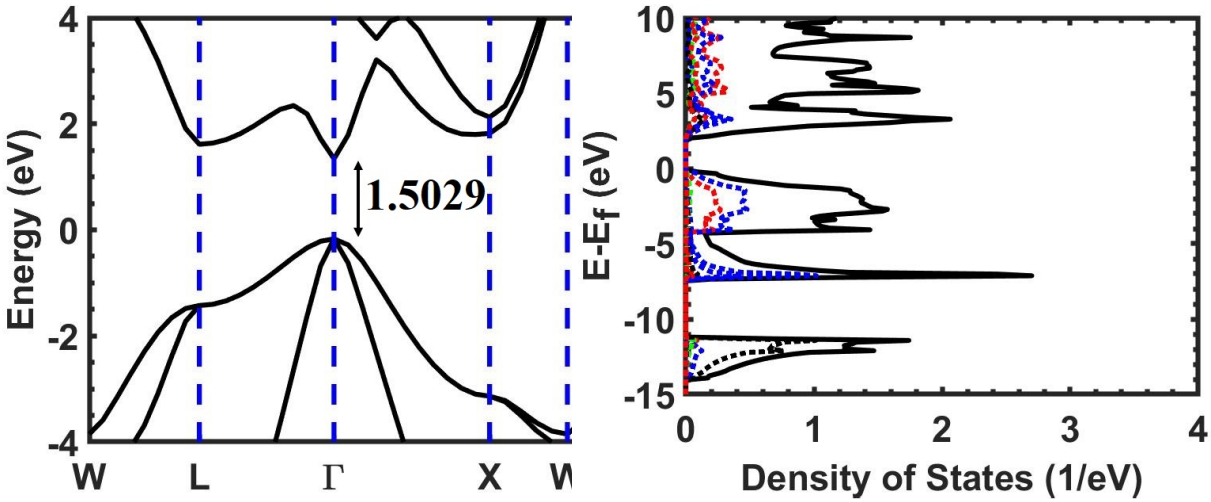

(a) Energy band diagram. **(b)** Density of States.

Figure 5.6: VASP simulation of GaAs using HSE06 with spin-orbit.

Finally, Fig. 5.7 contains the GaAs band diagram as simulated using the Hartree-Fock method. This also took approximately two days to complete, but with a predicted band gap of 4.582 eV that is substantially larger than the 1.44 eV predicted theoretically. The fact that the peak is extremely sharp is a simulation artifact.

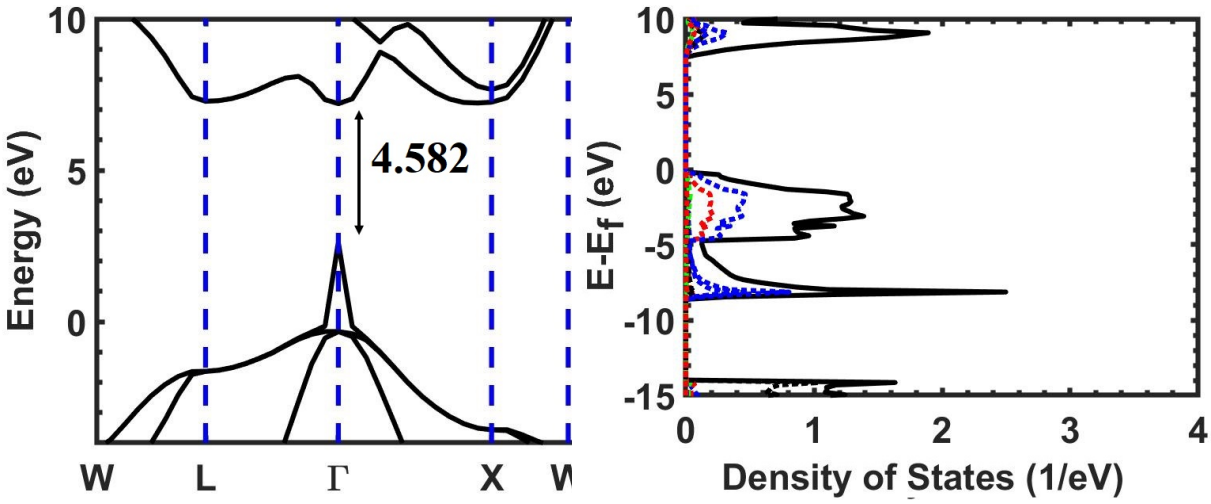

(a) Energy band diagram. **(b)** Density of States.

Figure 5.7: VASP simulation of GaAs using Hartree-Fock with spin-orbit.

5.2.2 InAs VASP Simulation Results

The same simulations as done for GaAs in section 5.1.1 were repeated for an InAs unit cell. Note that the expected band gap in this case is approximately 0.354 eV. [16]

Fig. 5.8 shows a band diagram generated using DFT with GGA-PBE and spin orbit. There is no discernible band gap in this $E - k$ plot. Clearly this is not real as InAs is a known semiconductor.

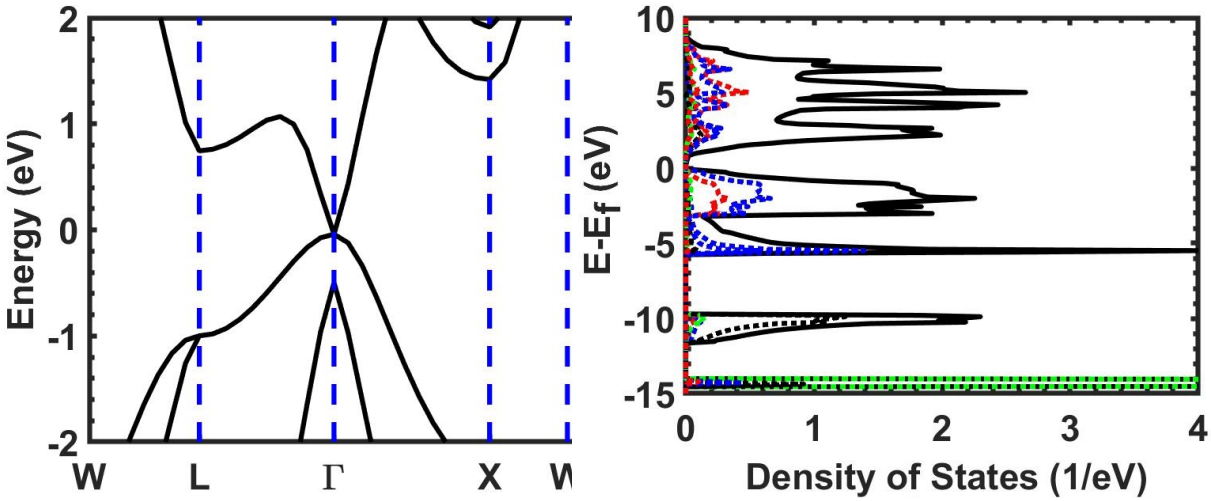

(a) Energy band diagram. **(b)** Density of States.

Figure 5.8: VASP simulation of InAs using DFT with spin-orbit coupling included.

Fig. 5.9 includes the band diagram from the HSE06 with spin orbit simulation. The band gap extracted from the $E - k$ plot is 0.4816 eV which is not far off from the expected band gap 0.354 eV.

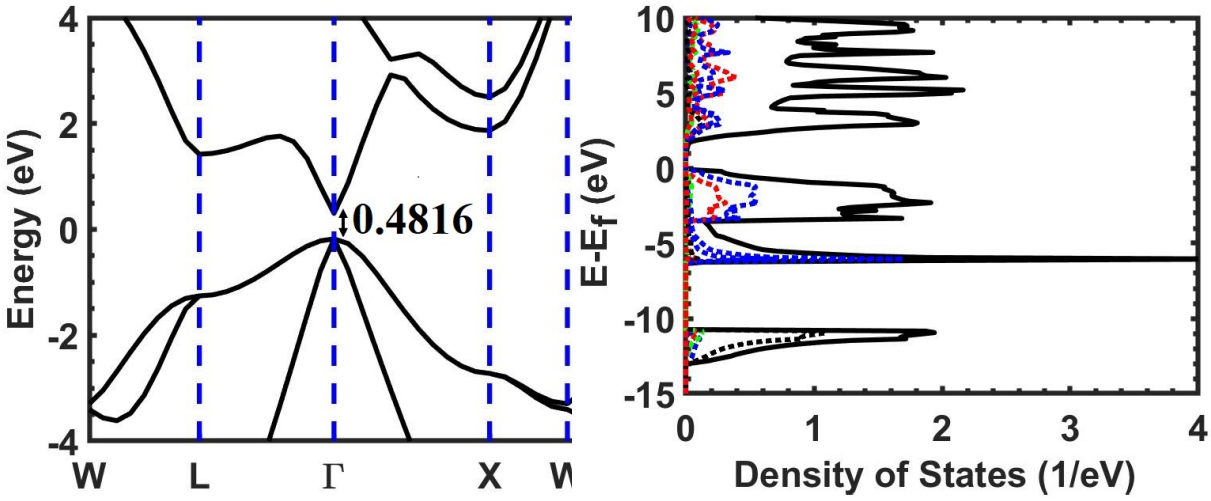

(a) Energy band diagram. **(b)** Density of States.

Figure 5.9: VASP simulation of InAs using HSE06 with spin-orbit.

Fig. 5.10 shows a band diagram generated using the Hartree-Fock method with spin orbit. Not only is this band gap extremely large (>5 eV), but it also simulated

InAs as an indirect band gap material, which is not true.

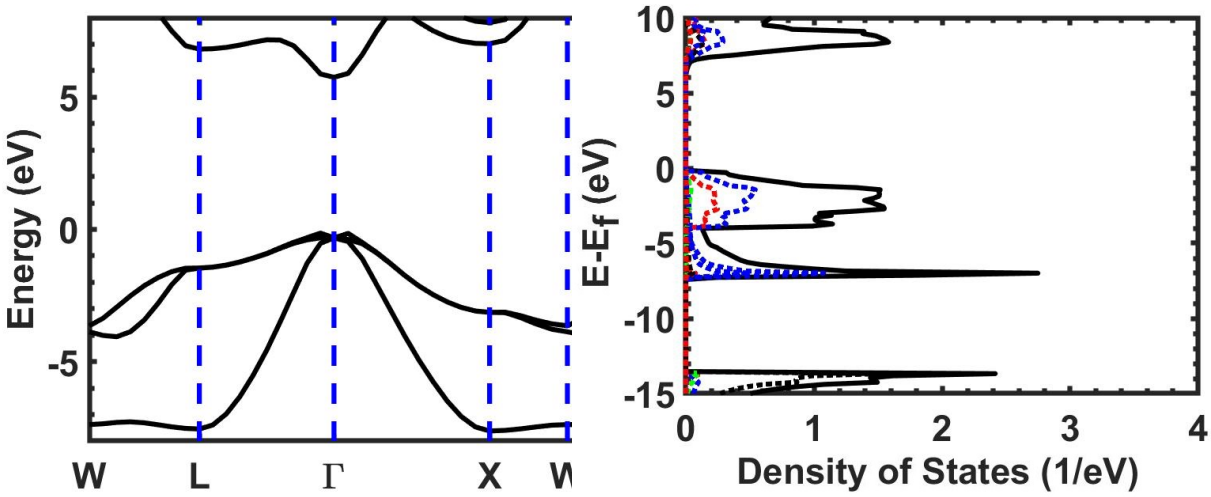

(a) Energy band diagram. **(b)** Density of States.

Figure 5.10: VASP simulation of InAs using Hartree-Fock with spin-orbit.

5.2.3 Reflections on Varying the Functional

From the data seen in Sections 5.2.1 and 5.2.2 it is clear that the HSE06 with GGA simulation method (a type of meta-GGA) was the most promising, while the Hartree-Fock the least useful (as well as time-consuming). In conclusion, the Hartree-Fock method is not a viable method of predicting material characteristics such as energy band gap, possibly because it requires more computational power or the simulation was not set up correctly.

5.3 The Effects of Varying the Functional: Part 2

More materials were simulated using both HSE06 with GGA and DFT with GGA with spin orbit turned on for all simulations. These results are included in Table 5.1.

Table 5.1: Materials simulated in VASP using HSE06 with GGA and DFT with GGA with spin orbit turned on. Note that the PWC is the plane-wave cutoff which refers to the distance the energy is simulated away from atom. The farther or larger this is, the more likely the simulation will converge to reality due to an increase in resolution, but also the longer the computation time. Note that the k-point spacing was 0.5/Å in a Γ-centered Monkhorst-Pack mesh, resulting in a 4x4x4 grid.

Material	Lattice (Å)	Calc E_g (ev)	Real E_g (ev)	Gap Type	PWC (eV)	Functional
GaAs	5.6339	0.4104	**1.424**	direct	0.0327	DFT GGA_BE
		1.3601		direct		**HSE06 GGA_BE**
InAs	6.048	0	**0.354**	direct	239.21	DFT GGA_PBE
		0.3523		direct		**HSE06 GGA_PBE**
GaSb	6.118	0	**0.726**	direct	282.69	DFT GGA_PBE
		0.6077		direct		**HSE06 GGA_PBE**
InP	5.8687	0.5411	**1.344**	direct	255.04	DFT GGA_PBE
		1.3723		direct		**HSE06 GGA_PBE**
AIAs	5.62	1.147	2.153	indirect	240.3	DFT GGA_PBE
		1.8871		indirect		HSE06 GGA_PBE
Ge	5.65	0.0001	0.661	direct	310.29	DFT GGA_PBE
		1.7291		indirect		HSE06 GGA_PBE
AISb	6.1347	0.8767	**1.615**	indirect	240.3	DFT GGA_PBE
		1.5577		indirect		**HSE06 GGA_PBE**
GaP	5.4505	1.4581	**2.26**	indirect	286.69	DDFT GGA_PBE
		2.1886		indirect		**HSE06 GGA_PBE**
AIP	5.451	1.3775	2.45	indirect	255.04	DFT GGA_PBE
		2.1624		indirect		HSE06 GGA_PBE
Si	5.431	0.41418	**1.12**	indirect	255.04	DFT GGA_PBE
		1.0845		indirect		**HSE06 GGA_PBE**

From Table 5.1, as well as the results of the previous section, HSE06 is decidedly worth the extra simulation time as its results are significantly more likely to simulate reality. The **boldface** entries in Table 5.1 highlight the best fits, which in the case of these simulations were always found using the HSE06 GGA_PBE method.

5.4 Some Effects of Changing the Lattice Constant

The ultimate goal of this research is to lay the foundations for simulating TMD material interfaces. A few designed experiments using these materials were run to begin setting up VASP functionality in this regard. DFT with GGA with spin-orbit

turned on was the primary simulation method, chosen for its computation speed.

Fig. 5.11 shows 16 $E - k$ curves for MoS_2 where the lattice constant was varied in steps of 1% up to 15%. This type of variation would happen in reality through the addition of strain to the material system. The top (solid black) line in this plot corresponds to the generic lattice constant of MoS_2, 3.16 Å. The shift in minimum energy to different Brillouin zones is noteworthy for further analysis beyond the scope of this report.

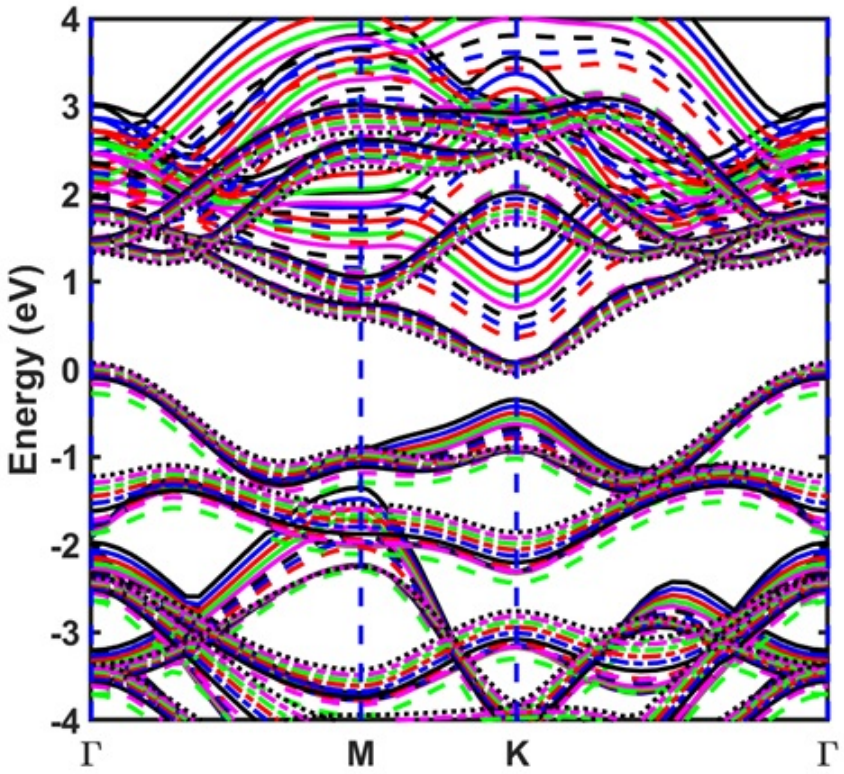

Figure 5.11: VASP DFT with GGA simulation of MoS_2 band diagrams varying with lattice constant. The top (solid black) line corresponds to the original lattice constant.

Fig. 5.12 plots the data from Fig. 5.11, as well as from the same designed experiment run for WTe_2.

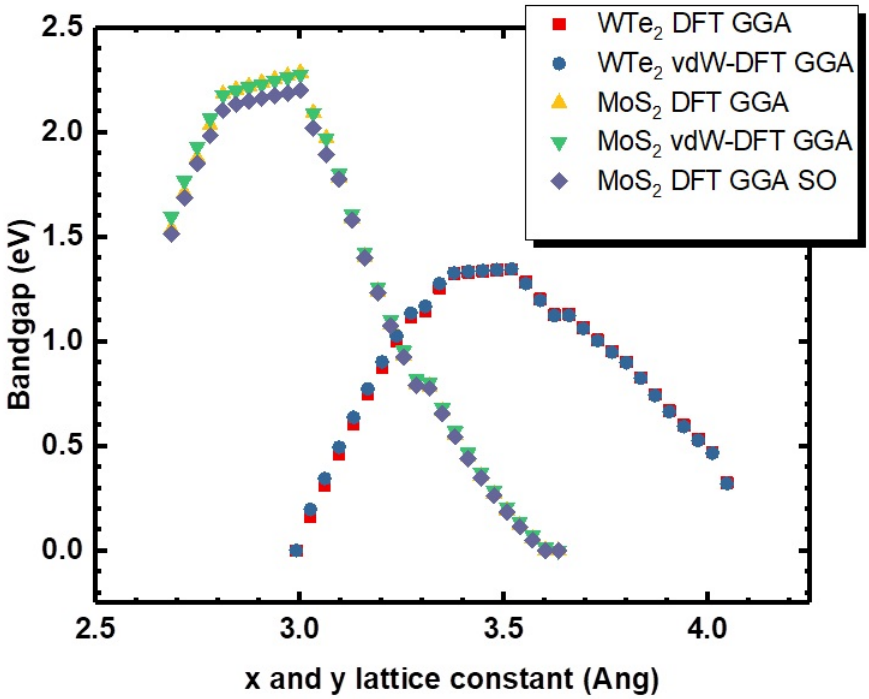

Figure 5.12: VASP DFT GGA simulation data of the MoS_2 and WTe_2 lattice constant variation designed experiment explained above. vdW corresponds to a setting in the simulation where van der Waals forces are applied.

The final plot, seen in Fig. 5.13 shows the MoS_2 bandstructures as simulated in NEMO5 and VASP 5.4 plotted together. The reason for the discrepancies in the data lines is that the tight-binding parameters used for generating the data set in NEMO5 do not correspond exactly to the VASP 5.4 simulation results. The relevance of these results is that the difference between the two data sets can be calculated to generate a new set of bowing parameters.

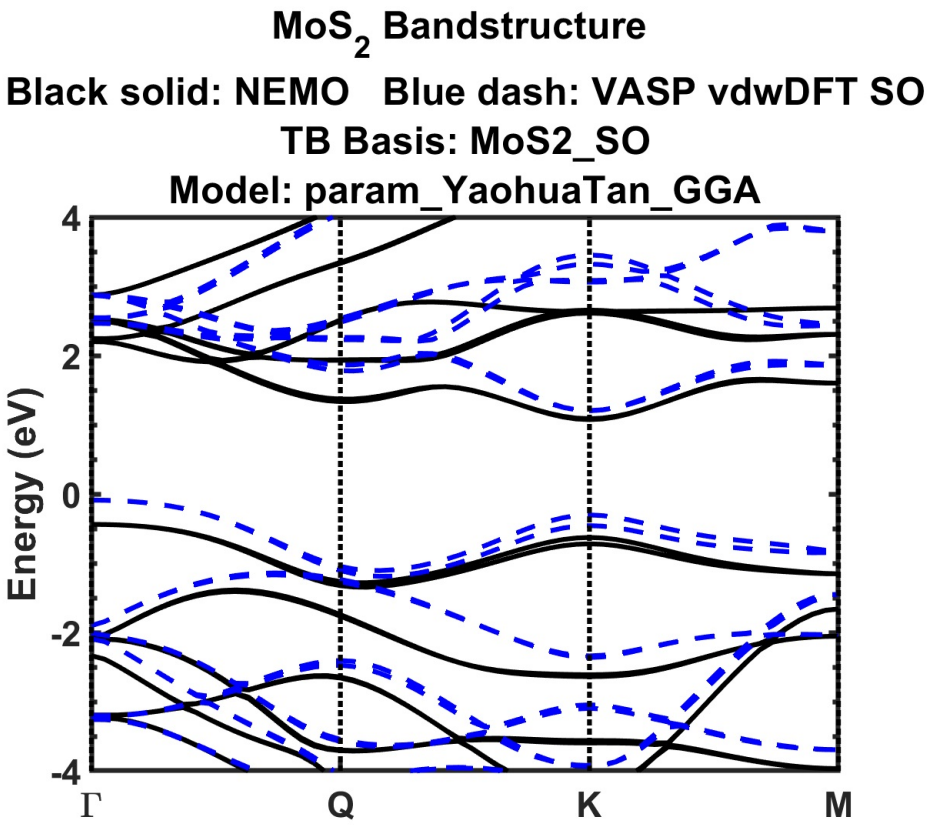

Figure 5.13: VASP 5.4 van der Waals DFT GGA simulation data of MoS_2 plotted against NEMO5 MoS_2 simulations. Spin-orbit is applied during both simulations.

Chapter 6

Conclusions

6.1 Summary of Work

This thesis has set the groundwork necessary for successful fabrication of TFETs with TMD channels at RIT. For such work to become a reality, simulations have to first be performed so as to reduce fabrication cost and increase the likeliness of generating functioning devices. Quantum simulations were identified as a necessity over TCAD simulations through a thorough study of simulation results performed by other groups. The study discussed in this paper is by Jiang *et al.* [10].

The goal of quantum simulations are $E - k$ plots and $I - V$ characteristics that correspond to "real" or experimental data. This means that the simulated data must converge onto reality; the Jacobian iterative method was considered as an example algorithm used by the NEMO5 simulation package to achieve convergence. NEMO5 and VASP 5.4 were both considered and used for the first time at RIT in device design capacity in this thesis. The understanding developed of both is crucial for further work in designing TFET devices.

Previous Esaki diode data was simulated in NEMO5 and the match to reality was poor. To determine why this was so, the band gaps for the material systems were simulated: for GaAs and InAs as simulated by NEMO5, reasonable results were seen, but the band gap for InGaAs was significantly higher than the reality. This

was fixed by developing an understanding of the virtual crystal approximation model used as the tight-binding parameters in NEMO5, and then editing these parameters to contain the effects of bowing parameters as described in Luisier *et al.* [15]. The Esaki diode data was simulated using the newly generated model containing the bowing effects and the results were seen to match reality closely. Thus, the understanding of the bowing effects and how they can be applied to create a calibrated simulation model in NEMO5 is considered a huge find in this study.

Preliminary VASP 5.4 band gap calculations were performed for various III-Vs and other common semiconductors. An experiment was run to determine the most accurate simulation method and the HSE06 with GGA simulation method (a type of meta-GGA) was determined to be the most promising, while the Hartree-Fock the least useful (as well as time-consuming). The Hartree-Fock method is not a viable method of predicting material characteristics such as energy band gap, possibly because it requires more computational power.

Lattice constant variation effects in VASP 5.4 were considered for both standard III-V and MoS_2 and WTe_2 systems. More work should be done in this regard if there is any interest in the effects of strain on 2D materials. Finally, VASP 5.4 and NEMO5 results for MoS_2 bandstructure simulations were plotted together, which is the first step to calculating a set of bowing parameters for this material system.

6.2 Future Work

As this thesis has been merely a first look at using NEMO5 and VASP 5.4 for quantum simulations at the Rochester Institute of Technology, there is substantially more work to do in terms of benchmarking both software packages before actual TMD TFETs can be simulated meaningfully. The ultimate goal is, of course, fabrication of such devices.

Some suggestions for more immediate work include a study of bowing parameters

for other material systems, specifically TMDs. Sharma *et al.*, Mourada and Czycholl, Zhao *et al.*, and Kang *et al.* are all suggested as good starting materials in this regard [40, 41, 42, 43]. Another item is to edit the newly created *all.mat* InGaAs file to remove the *d*-orbital effects and analyze the results to determine the necessity of the *d*-orbital for a true simulation. This is especially useful as the matrix corresponding to the new file would be smaller and thus take less time to simulate, but the accuracy difference between the two simulations must be considered.

Further necessary VASP benchmarking includes developing an understanding of the basic TMD Brillouin zones and the way VASP goes about traversing these, as well as running more standard simulations for TMD energy band diagrams. Also necessary is the further development of a super-cell structure in VASP as this is necessary to simulate compounds such as InGaAs.

References

[1] P. Hohenberg and W. Kohn, "Inhomogeneous electron gas," *Physical Review A*, vol. 136B, p. 864, 1964.

[2] S. Datta, H. Lie, and V. Narayanan, "Tunnel fet technology: A reliability perspective," *Microelectronics Reliability*, vol. 54, no. 5, pp. 861–874, 2014.

[3] D. J. Pawlik, "Comprehensive mapping and benchmarking of esaki diode performance," Ph.D. dissertation, Rochester Institute of Technology.

[4] C. Wei, D. Sarkar, Y. Khatami, K. Jiahao, , and K. Banerjee, "Subthreshold-swing physics of tunnel field-effect transistors," *AIP Advances*, vol. 4, no. 6, June 2014.

[5] C. Wei, K. Jiahao, D. Sarkar, L. Wei, and K. Banerjee, "2d semiconductor fets-projections and design for sub-10 nm vlsi," *IEEE Transactions on Electron Devices*, vol. 62, no. 11, pp. 3459–69, November 2015.

[6] H. Ilatikhameneh, T. Yaohua, B. Novakovic, G. Klimeck, R. Rahman, and J. Appenzeller, "Tunnel field-effect transistors in 2-d transition metal dichalcogenide materials," *IEEE Journal on Exploratory Solid-State Computational Devices and Circuits*, vol. 1, pp. 12–18, 2015.

[7] A. Seabaugh, S. Fathipour, W. Li, H. Lu, J. H. Park, A. C. Kummel, D. Jena, S. K. Fullerton-Shirey, and P. Fay, "Steep subthreshold swing tunnel fets: Gan/inn/gan and transition metal dichalcogenide channels," in *61st IEEE International Electron Devices Meeting*, December 2015, pp. 35.6.1–35.6.4.

[8] L. Fei, W. Jian, and G. Hong, "Atomistic simulations of device physics in monolayer transition metal dichalcogenide tunneling transistors," *IEEE Transactions on Electron Devices*, vol. 63, no. 1, pp. 311–17, January 2016.

[9] C. Gong, H. Zhang, W. Wang, L. Colombo, R. M. Wallace, , and K. Cho, "Band alignment of two-dimensional transition metal dichalcogenides: Application in tunnel field effect transistors," *Applied Physics Letters*, vol. 103, no. 5, 2013.

[10] Z. Jiang, Y. Lu, Y. Tan, Y. He, M. Povolotskyi, T. Kubis, A. C. Seabaugh, P. Fay, and G. Klimeck, "Quantum transport in algasb/inas tfets with gate field in-line with tunneling direction," *IEEE Transactions on Electron Devices*, vol. 62, no. 8, pp. 2445–49, August 2015.

[11] L. A. Bennett. What is electron configuration? [Online]. Available: http://edtech2.boisestate.edu/lindabennett1/502/periodic-table-e20config/electron20configuration.html

[12] s,p,d,f orbitals. [Online]. Available: https://socratic.org/chemistry/the-electron-configuration-of-atoms/arrangement-of-electrons-in-orbitals-spd-and-f

[13] J. P. Perdew and K. Schmidt, "Jacob's ladder of density functional approximations for the exchange-correlation energy," in *AIP Conference Proceedings 577*, no. 1, 2001.

[14] D. Pawlik, B. Romanczyk, P. Thomas, S. Rommel, M. Edirisooriya, R. Contreras-Guerrero, R. Droopad, W.-Y. Loh, M. H. Wong, K. Majumdar, W.-E. Wang, P. D. Kirsch, and R. Jammy, "Benchmarking and improving iii-v esaki diode performance with a record 2.2 ma/cm2 peak current density to enhance tfet drive current," in *International Electron Devices Meeting*, 2012, pp. 27.1.1–27.1.3.

[15] M. Luisier and G. Klimeck, "Investigation of $in_xga_{1-x}as$ ultra-thin-body tunneling fets using a full-band and atomistic approach," in *International Conference on Simulation of Semiconductor Processes and Devices*, September 2009.

[16] Band structure and carrier concentration of gainas. [Online]. Available: http://www.ioffe.ru/SVA/NSM/Semicond/GaInAs/bandstr.html

[17] D. Neamen, *An Introduction to Semiconductor Devices*, 3rd ed. McGraw Hill, 2006.

[18] S. M. Sze, *The Physics of Semiconductor Devices*, 3rd ed. John Wiley and Sons, Inc., 2007.

[19] Z. Jiang, Y. Lu, Y. Tan, Y. He, M. Povolotskyi, T. Kubis, A. C. Seabaugh, P. Fay, and G. Klimeck, "Discovery of the tunnel diode," *IEEE Transactions on Electron Devices*, vol. ED-23, no. 7, pp. 644–647, July 1976.

[20] A. Seabaugh and R. Lake, *Encyclopedia of Applied Physics*, 1998, vol. 22.

[21] E. O. Kane, "Theory of tunneling," *Journal of Applied Physics*, vol. 32, no. 1, pp. 83–91, January 1961.

[22] R. Venugopal, M. Paulsson, S. Goasguen, S. Datta, and M. S. Lundstrom, "A simple quantum mechanical treatment of scattering in nanoscale transistors," *Journal of Applied Physics*, vol. 93, no. 9, p. 5613–25, April 2003.

[23] M. P. Anantram, M. S. Lundstrom, and D. E. Nikonov, "Modeling of nanoscale devices," *Proceedings of the IEEE*, vol. 96, no. 9, pp. 1511–50, September 2008.

[24] M. Buttiker, "Four-terminal phase-coherent conductance," *Physical Review Letters*, vol. 57, no. 14, pp. 1761–64, October 1986.

[25] G. Zhou, R. Li, T. Vasen, M. Qi, S. Chae, Y. Lu, Q. Zhang, H. Zhu, J.-M. Kuo, T. Kosel, M. Wistey, P. Fay, A. Seabaugh, and H. Xing, "Novel gate-recessed vertical inas/gasb tfets with record high ion of 180 μa/ μm at vds= 0.5 v," in *2012 International Electron Devices Meeting*, 2012, pp. 32.6.1–32.6.4.

[26] Y. Tan, "Tight binding parameterization from ab-initio calculations and its applications," Ph.D. dissertation, Purdue University.

[27] M. M. Cohen, *Introduction to the Quantum Theory of Semiconductors.* Gordon and Breach, 1972.

[28] J. Callaway, *Energy Band Theory.* Academic Press, 1964.

[29] H. Jones, *The Theory of Brillouin Zones and Electronic States in Crystals.* North-Holland Pub. Co, 1960.

[30] R. Hummel, *Electronic Properties of Materials*, 4th ed., 2011.

[31] T. B. Boykin, G. Klimeck, R. C. Brown, and F. Oyafuso, "Diagonal parameter shifts due to nearest-neighbor displacements in empirical tight-binding theory," *Physical Review B*, pp. 125 207–1–125 207–6, 2002.

[32] P. Vogl, H. P. Hjalmarson, and J. D. Dow, "A semi-empirical tight-binding theory of the electronic structure of semiconductors," *Journal of Physical Chemistry Solids*, p. 365, 1983.

[33] J.-M. Jancu, R. Scholz, F. Veltram, and F. Bassani, "Empirical spds tight-binding calculation for cubic semiconductors: General method and material parameters," *Physical Review B*, p. 6493, 1998.

[34] J. R. Lewis, *College Chemistry: An Up-to-date Survey with General Review Questions and Answers*, 8th ed. Barnes and Nobel, Inc., 1965.

[35] E. Engel and R. M. Dreizler, *Foundations of density functional theory: Existence theorems.* Heidelberg: Springer Berlin Heidelberg, 2011.

[36] J. E. Drut, R. J. Furnstahl, and L. Platter, "Toward ab initio density functional theory for nuclei," *Progress in Particle and Nuclear Physics*, vol. 64, no. 1, pp. 120–168, 2010.

[37] S. Clark. (2012) The kohn-sham formulation. [Online]. Available: http://cmt.dur.ac.uk/sjc/thesis-dbj/node14.html

[38] C. G. Cullen, *An Introduction to Numerical Linear Algebra.* PWS Publishing Company, 1994.

[39] P. Bhattacharya, *Energy gaps and band structure of lattice-matched and strained InGaAs*, 1993.

[40] T. K. Sharma, R. Jangir, S. Porwal, R. Kumar, T. Ganguli, M. Zorn, U. Zeimer, F. Bugge, M. Weyers, and S. M. Oak, "Compositional dependence of the bowing parameter for highly strained ingaas/gaas quantum wells," *Physical Review B*, pp. 165 403–1–165 403–2, 2009.

[41] D. Mourada and G. Czycholl, "Theory of band gap bowing of disordered substitutional ii-vi and iii-v semiconductor alloys," *The European Physical Journal B*, no. 153, pp. 1–13, 2012.

[42] Y. Zhao, Z. Zhang, and G. Ouyang, "Band shift of 2d transition-metal dichalcogenide alloys: size and composition effects," *Applied Physics A*, 2018.

[43] J. Kang, S. Tongay, J. Li, and J. Wu, "Monolayer semiconducting transition metal dichalcogenide alloys: Stability and band bowing," *Journal of Applied Physics*, pp. 143 703–1–143 703–7, 2013.

Appendix A: Hohenburg-Kohn Theorem Proof [1]

Proof: if $\Psi \neq \Psi$'then $\rho \neq \rho$'.

Assume $\Psi \neq \Psi$'and $\rho = \rho$', and prove that this is untrue.

Ψ is the ground state of $\hat{\mathrm{H}}$ with ground energy E_{gs},

and Ψ'is the ground state of $\hat{\mathrm{H}}$' with ground energy E'_{gs}.

Assuming the same number of electrons:

$$\hat{H} = T + W + V \tag{A.1}$$

and

$$\hat{H}' = T + W + V' \tag{A.2}$$

so

$$\hat{H} = \hat{H}' - V' + V. \tag{A.3}$$

Applying the variational principle:

$$E_{gs} = \langle \Psi | \hat{H} | \Psi \rangle < \langle \Psi' | \hat{H} | \Psi' \rangle = \langle \Psi' | \hat{H}' - V' + V | \Psi' \rangle = E'_{gs} + \int \rho'(\bar{r})[v(\bar{r}) - v'(\bar{r})]d\bar{r}. \tag{A.4}$$

Now repeat the argument, starting with Ψ':

$$E'_{gs} < E_{gs} + \int \rho(\bar{r})[v'(\bar{r}) - v(\bar{r})]d\bar{r}. \tag{A.5}$$

Assuming $\rho = \rho'$, add the previous statements:

$$E'_{gs} + E_{gs} < E'_{gs} + E_{gs} \tag{A.6}$$

This is clearly a contradiction. Therefore, $\rho \neq \rho$'has been proven.

Appendix B: Brief Guide to Using MedeA 2.22.2 for VASP 5.4 Simulations

B.1 Part 1: MedeA Set-Up

Begin by opening *runJobServer* and *runTaskServer* from the *Materials Design* folder. Once these are loaded, open *MedeA 2.22.2*. These options can be seen in Fig. B.1.

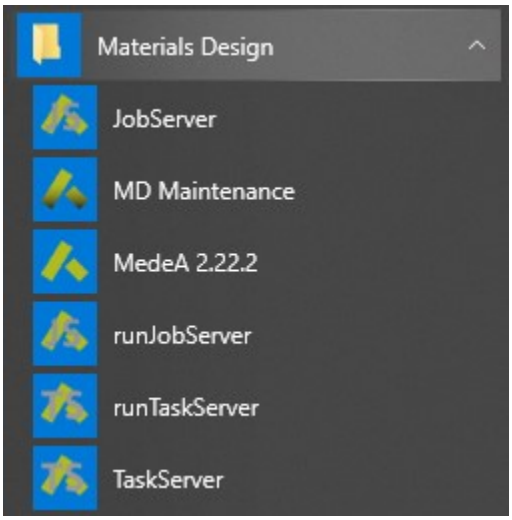

Figure B.1: Materials Design folder as seen running Windows 10 Pro.

Next, click on *Tools* and load *InfoMaticA* and *VASP 5.4* from the drop-down menu. These two tools will appear up top as extra drop-down menus.

Now click *Job Control* and *Select Server* to select the relevant server. The default in this example scenario is the *local* server which refers to the laptop MedeA is installed on, but other servers can be called as well, and these will appear here. Note that it is also possible to point to a remote machine for execution, but this is beyond the scope of this example.

B.2 Part 2: Cell Set-Up

Select *InfoMaticA* and load the *Search* function. The InfoMaticA Search menu will appear. Click *Add New Criterion* from the bottom half of this menu and select *Formula* from the drop-down menu. Type the molecule of interest into the box which appears. In this example case this is indium arsenide (InAs). The relevant existing structures in the library will appear in the top half of the search menu, as seen in Fig. B.2. If there are multiple results, as is the case in this example, click *Edit* and *Find Median Structures* to narrow it down to one selection.

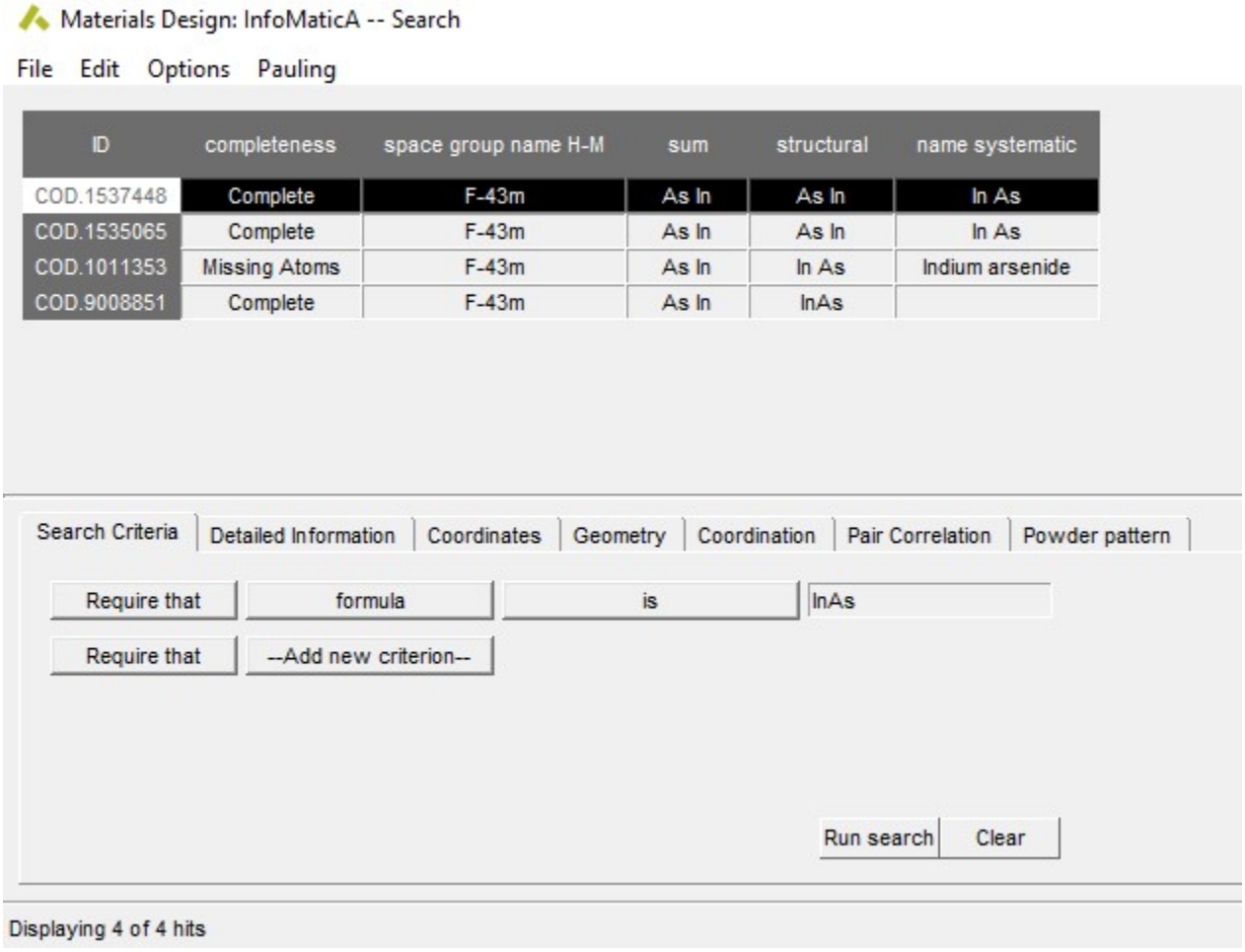

Figure B.2: InfoMaticA Search menu as seen after selecting InAs for this example.

Next, right click on the molecule that is left and select *View*. A figure will appear

in MedeA which can be rotated by clicking the molecule and dragging the cursor; this is the molecule in question. The molecule in its initial state, as seen in Fig. B.3(a), is bond-less; to add bonds right-click on it and select *Edit bonds*. Click *OK* if the bond parameters correspond to what is known about the molecule; this will result in Fig. B.3(b).

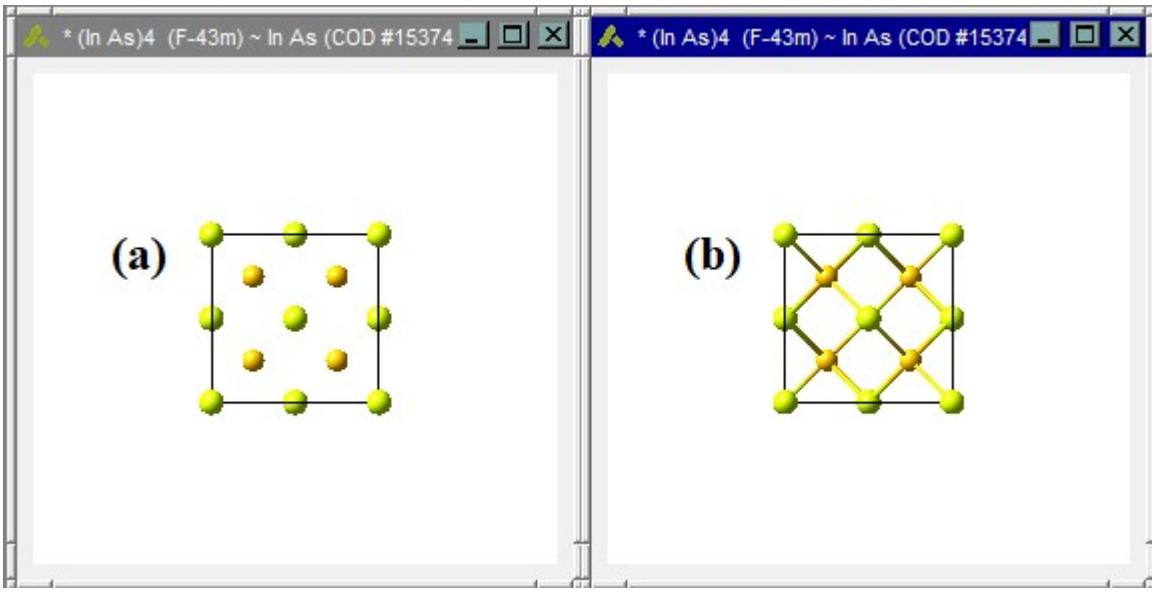

Figure B.3: (a) The InAs molecule chosen as seen without bonds applied. (b) The InAs molecule chosen as seen with bonds applied.

To edit things such as the lattice constant (A= 6.048 Å for InAs remains unchanged in this example case) or to add, move, or remove atoms, right click the cell in question again and click *Edit Cell*. After this, the cell has been set up and VASP is ready to be run.

B.3 Part 3: Structural Optimization using VASP 5.4

The cell must now be minimized, and this is done with VASP 5.4. Click *VASP 5.4* from the menu bar and select *Run*. The menu which will appear is seen in Fig. B.4. All the settings in Fig. B.4 correspond to the standard for *Standard Optimization*. Specifically, these include turning on *Relax atom positions*, *Allow cell*

volumes to change, and *Allow cell shape to change*; the functional can be changed to any functional of interest, though the *Density functional* with the $GGA - PBEsol$ exchange correlation selected is one of the fastest to run; $Spin - orbit\ magnetic$ can be turned on or off from the *Magnetism* option (note that turning it on will increase simulation time substantially); *Standard 500* is the simplest *Precision* to run. The $Spacing\ of\ k - points$ can be edited under the *SCF* menu (0.5 1/Å is standard for InAs). Do not forget to edit the *Title* to something meaningful before running the simulation by clicking *Run*.

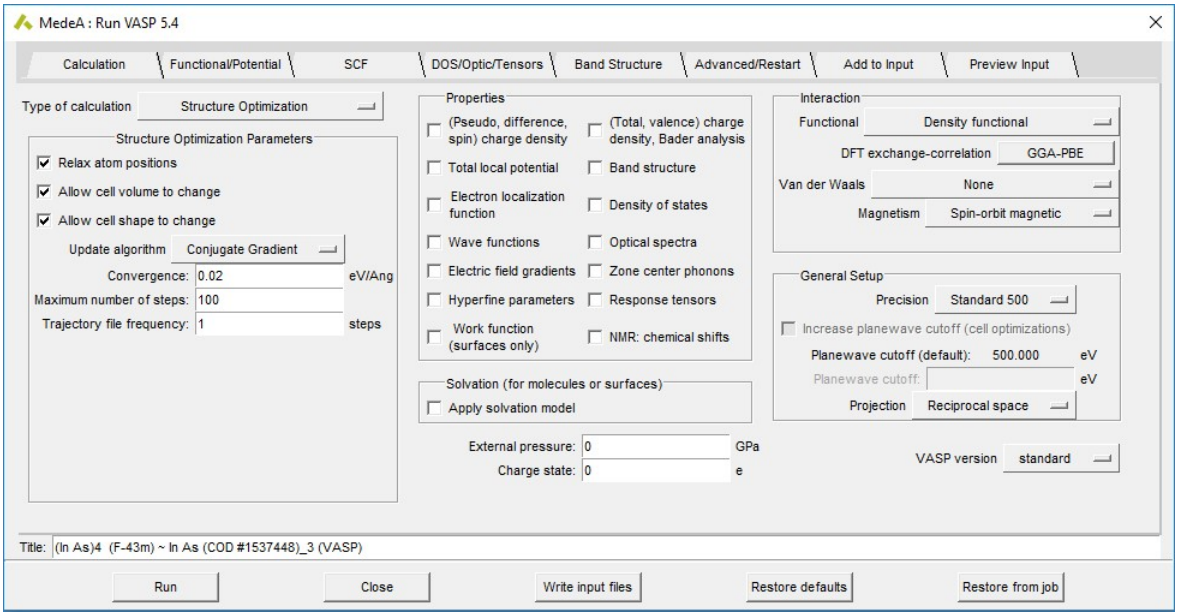

Figure B.4: General setup for Structural Optimization of the chosen InAs molecule.

A *Submit VASP Job* menu will appear where the server *Queue* may be chosen, as well as the *Number of processors* and *Priority* of the job at hand. This can be seen in Fig. B.5. The *Number of processors* is dependent on the machine the chosen server is running on (in the case of this example "minint-3famcrr" has an Intel Core i5-5200U Processor, which corresponds to two cores and four threads, so two is the maximum number of *Processors* available). The greatest *Priority* is 1 and the lowest is 10. Do not forget to add a relevant comment describing the job about to be run.

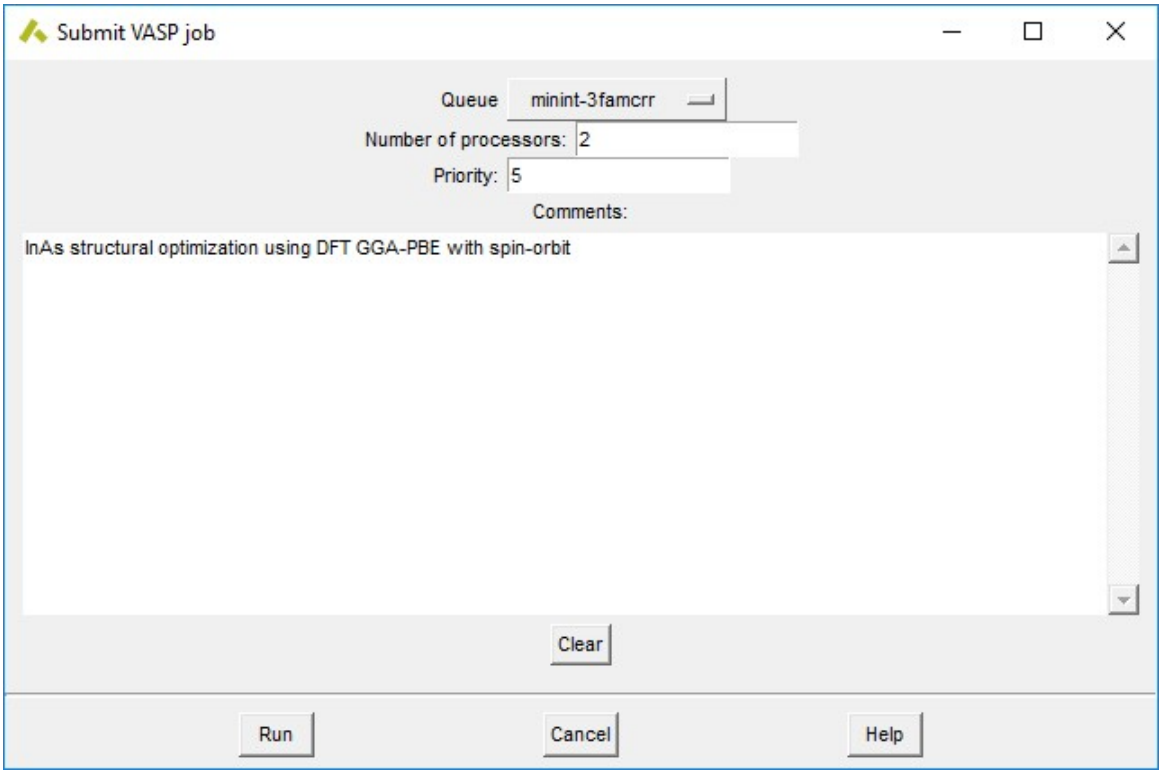

Figure B.5: The pre-run menu.

B.4 Part 4: Viewing and Controlling the Job requested

To view the job, open an Internet browser and type 127.0.0.1:32000/index.html into the search bar. The resulting page is seen in Fig. B.6.

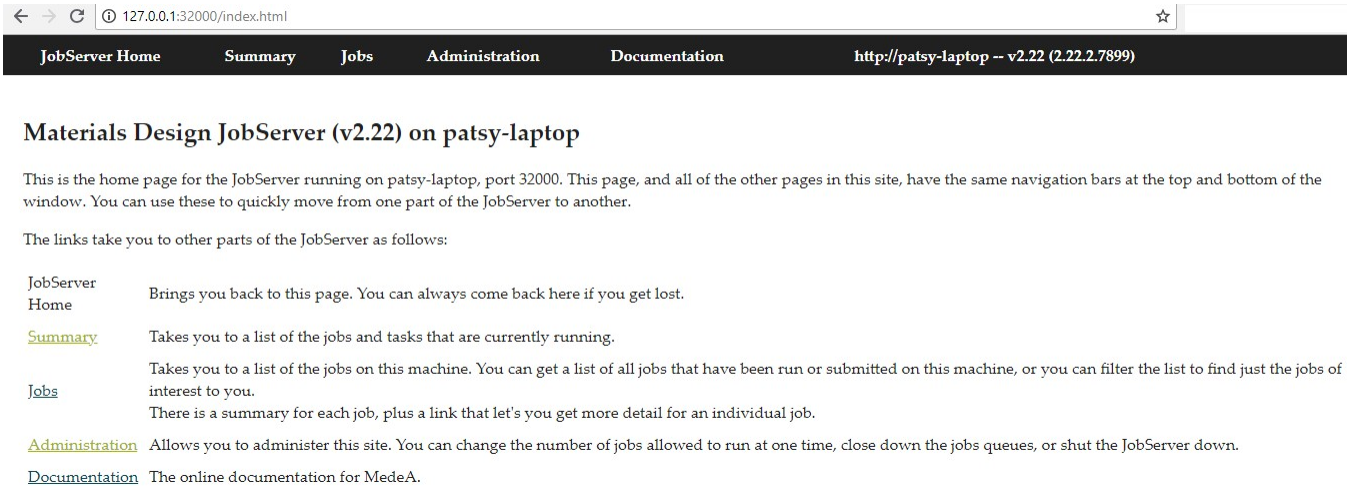

Figure B.6: The Materials Design JobServer menu.

To see the status of the current job, click *Jobs*. After the job in question is shown as *Finished*, load it into MedeA by clicking *File* and selecting *Open structure from job*.

B.5 Part 5: Band Structure and Density of States using VASP 5.4

To acquire meaningful data such as Band structure or Density of states information using VASP, start by clicking on *VASP 5.4* from the menu again. Next, select *Single − point*, followed by whichever *Properties* are of interest. In this case, *Band structure* and *Density of states* are both selected. As before, select the *Functional* of interest as well as the *Precision*. Fig. B.7 shows a sample set-up.

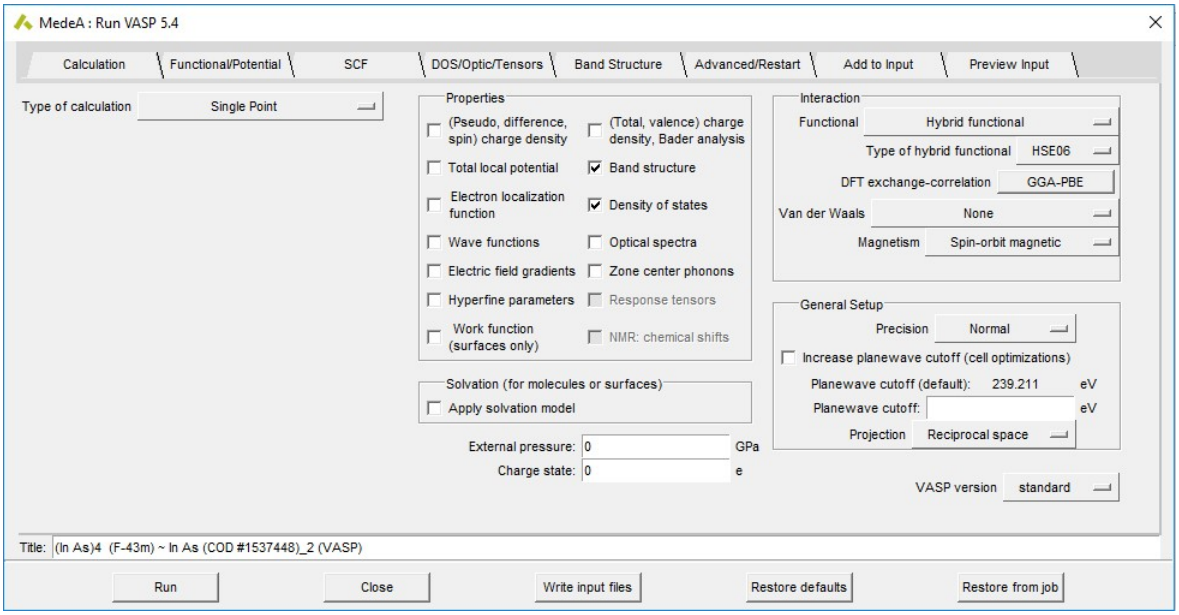

Figure B.7: Sample set-up of band structure and density of states run for the InAs model chosen.

Proceed to *Run*, view and control the job as before.

B.6 Part 6: Analysis

Click *Analysis* from the top menu, followed by the property of interest (in this case *Band structure* or *Density of States*), and choose the relevant job. These files can be exported for further analysis by clicking *Analysis*, *Export*, and finally *File Select* and selecting the relevant file.

Appendix C: NEMO5 Sample Device Simulation Files

The following files correspond to InGaAs-6 which was simulated in this study.

C.1 Typical Material and Structure definition

```
    Material { crystal_structure = zincblende
doping_density = 7E19
doping_type = N
name = GaInAs
x=0.47
regions = (3)
tag = InGaAs_highDoping }
Material { crystal_structure = zincblende
doping_density = 7E19
doping_type = N
name = GaInAs
x=0.47
regions = (2)
tag = InGaAs_lowDoping }
Material { crystal_structure = zincblende
doping_density = 9.6E19
doping_type = P
name = GaInAs
x=0.47
regions = (1)
tag = GaSb_high_doping }
```

C.2 Domain definition

```
   Domain { base_material = InGaAs_lowDoping
crystal_direction1 = (1,0,0)
crystal_direction2 = (0,1,0)
crystal_direction3 = (0,0,1)
dimension = (48,1,1)
leads = (source_contact,drain_contact)
name = device
output = (xyz,coupling)
periodic = (false,true,true)
regions = (1,2,3)
space_orientation_dir1 = (1,0,0)
space_orientation_dir2 = (0,1,0)
starting_cell_coordinate = (0,0,0)
type = pseudomorphic }
```

C.3 Contact definitions

```
   source contact,source source contact,source source source contact
source mode contact,source source mode contact
drain contact,drain drain contact,drain drain drain contact
drain mode contact
```

C.4 Mesh Domain definition

```
   Domain{
mesh_from_domain = device
```

```
name = fem_device
number_of_refinement_steps = 1
refinement_regions = (1,2,3)
type = finite_elements
periodic = (false,true,true)}
Domain{
mesh_from_domain = drain_contact
name = fem_drain_contact
number_of_refinement_steps = 1
periodic = (false,false,false)
refinement_regions = (2,3)
type = finite_elements}
Domain{
mesh_from_domain = drain_drain_contact
name = fem_drain_drain_contact
number_of_refinement_steps = 1
periodic = (false,false,false)
refinement_regions = (2,3)
type = finite_elements}
```

C.5 Region definition

```
   Geometry{Region{
max = (9.38992,2,2)//represents 16 UC of InGaAs per div, a=0.58687 nm
min = (-20,0,0) //Hopefully I don't need to change this #.
priority = 1
region_number = 1
shape = cuboid}
```

```
Region{
max = (18.77984,2,2) //represents 16 UC of InGaAs per div, a=0.58687 nm
min = (9.38992,0,0)
priority = 1
region_number = 2
shape = cuboid}
Region{
max = (40,2,2)
min = (18.77984,0,0)//represents 16 UC of InGaAs per div, a=0.58687 nm
priority = 2
region_number = 3
shape = cuboid}}}
```

C.6 QTBM Solver definition

```
   solver{
type = MetaPoissonQTBM5
name = QTBM
active_regions = (1,2,3)
clean_all_in_reinit = true
contact_domains = (source_contact,drain_contact)
contact_aux = (source_source_mode_contact)
output = (JE,NE,current,ldosn1d,ldosp1d)
tb_basis = sp3d5sstar
energy_grid_constructor = QTBM:adaptive_grid_generator
number_of_MPI_ranks_in_real_space = 1
density_solver = QTBM:Transformation1
derivative_of_density_solver = QTBM:Transformation1
```

```
solve_on_single_replica = true
solver_type = compression
with_poisson = true
no_file_output = true
debug_output_job_list = false
regions_adjacent_to_source_electrode = 1
regions_adjacent_to_drain_electrode = 3
source_voltage = 0.0
drain_voltage = 0.0
ramper_voltage  (-0.65,-0.6,-0.55,-0.5,-0.45,-0.4,-0.35,-0.3,-0.25,-0.2,-0.15,-0.1
ramper_contact = source
no_integration_for_transmission = true
system_type = quasi_1D
kxmax = 0.5
kxmin = 0
kymax = 0.5
kymin = 0
number_of_k_points = 14
degeneracy_factor = 4
non_rectangular_energy = true
laplacian = (x)
bands_number_of_nodes = (100)
number_of_eigenvalues = 80
number_of_eigenvalues_to_use = 16
output_line_corners = [(0, 0.2, 0.2), (40, 0.2, 0.2)]
number_1D_output_points = 100
homogeneous_initial_potential = 0.3
```

```
selfconsistent_algorithm = fast

electron_hole_model = true

electron_hole_heuristics = omen_smooth

particle_source = hole

particle_drain = electron

iteration_output = false

poisson_max_iterations = 24

bandstructure_smart_parallelization = true

parallelize_adaptive_grid_construction = true

residual_criterion = 1.e-5}
```